SLAC-396
UC-414
(E)

A Measurement of the Z^0 Hadronic Branching Fraction to Bottom Quarks and the Charged Multiplicity of Bottom Quark Events Using Precision Vertex Detectors at E_{CM} = 91 GeV*

Dale Steven Koetke

Stanford Linear Accelerator Center
Stanford University
Stanford, California 94309

June 1992

Prepared for the Department of Energy
under contract number DE-AC03-76SF00515

* Ph.D. Thesis

Abstract

Using the precision vertex detectors of the Mark II at the SLC, an impact parameter tag was developed to select a sample of hadronic Z^0 decays enriched in its fraction of bottom quark events. The nominal tagging method requires that there be at least three tracks whose impact parameters are inconsistent with the track having originated at the electron-position interaction point. A tagging efficiency for $b\bar{b}$ events of 50% with a enriched sample purity of 85% was achieved.

This impact parameter tag was used to measure the fraction hadronic Z^0 decays which produce $b\bar{b}$ events, F_b. It is found that

$$\mathrm{F}_b = 0.232^{+0.053}_{-0.045}\,(\mathrm{stat})\,^{+0.025}_{-0.021}\,(\mathrm{syst}).$$

This result is consistent with those found using other tagging methods as well as the Standard Model prediction of 0.217.

The $b\bar{b}$-enriched event sample was also used to measure the difference between the average charged multiplicity of $b\bar{b}$ events and that of all hadronic Z^0 decays,

$$\delta\bar{n}_b = 2.11 \pm 1.82\,(\mathrm{stat}) \pm 0.57\,(\mathrm{syst}).$$

Using previous measurements of the total hadronic charged multiplicity, the corresponding total multiplicity for $b\bar{b}$ events is

$$\bar{n}_b = 23.05 \pm 1.82\ (\mathrm{stat}) \pm 0.60\ (\mathrm{syst}).$$

Subtracting the contribution to the multiplicity from B hadron decays yields the multiplicity of the $b\bar{b}$ non-leading system,

$$\bar{n}_{nl} = 12.04 \pm 1.82\ (\mathrm{stat}) \pm 0.63(\mathrm{syst}).$$

Comparing this non-leading multiplicity to the total hadronic multiplicity data at lower energy supports the hypothesis that the non-leading particle production is independent of the flavor of the inital quarks. This also yields a determination of the average energy fraction of bottom hadrons in Z^0 decays of

$$\langle x_E \rangle_b = 0.619^{+.096}_{-.107}\,(\mathrm{stat})^{+.043}_{-.045}(\mathrm{syst}).$$

Acknowledgments

Many people have contributed to the quality of my experiences during the years I have spent at SLAC and at Stanford. First and foremost, I want to express my sincere gratitude to my advisor, John Jaros. Working under his tutelage for the past six years I have learned a great deal about how to do experimental physics. Participating in the assembly and use of the DCVD has been a great opportunity and valuable learning experience. I am also grateful for John's patience and his guidance. His insight into different solutions and new approaches to solving the problems has been invaluable.

I also owe a debt of gratitude to the members of the *B* Physics Working Group, especially Chris Adolphsen, Don Fujino, Bob Jacobsen, Bruce Schumm, and Steve Wagner who all worked heroically to extract information from a tiny event sample. I have learned much from having had the opportunity to work with each of these people and enjoyed the interaction with them. In particular I want to express my thanks to Bruce, with whom I collaborated on the multiplicity analysis.

Building the DCVD was a large part of my experience here and I want to thank all of those who took part in that project. Specifically, working with Jim Smith on various aspects of this project was both enjoyable and a good chance to learn the physics of wire chambers from a hands-on perspective. Ken Hayes and Jim Alexander also helped me get started on the DCVD by providing guidance on projects which I could squeeze into a busy schedule of classes during my first two years at Stanford.

Of course even the DCVD was part of a much larger detector, and I want to thank all of the Mark II Collaborators for having supported the detector even through the 1990 run.

Throughout my time at SLAC, I have been a member of Martin Perl's group, and am most grateful for his support. Other Group E members, especially Lee Anne Kowalski, Mike Hildreth and Charles Munger and Dave Coward, have been good friends. Thanks for all of the help and the enlightening discussions. Deserving special thanks, however, is Lydia Beers, for everything she has done to make my life at SLAC easier.

Nina Adelman-Stolar has been another good friend and someone who was always willing to help out when the going got tough. Also, thanks to Sylvia and Terry in publications for helping with some of the complicated figures in this thesis.

My six years at Stanford has also allowed me to make many new and dear friends. Keith Martinez, Brian Sterling and Jon Labs made the first-year of graduate school bearable and have been very good friends since then. Living in Escondido Village also provided the opportunity to get to know many new friends, particularly Bruce and Tracy Onsager, and Reinaldo Michelena and Mainlin Suarez. I must also thank a much older friend, Dave Klemz, for providing some of the most fun I have had during my time at Stanford: the yearly ski weeks! Finally, I appreciate the opportunities I had to get away from it all by visiting the Roach family. I'll cherish the time spent at the cabin and the visits to Tres Hombres.

I must also express my deepest thanks for the friendship I have with my family, particularly my mother and father, my brother and my sister. They were always supportive of my endeavors and have provided many of my life's most memorable moments.

Finally, I want to dedicate this thesis to two people: my father and my wife. To my father, I am grateful for having fed my curiosity and guided my learning of the physical world, from my earliest memories through my years in college as both an advisor and a friend. He has set an fine example of what one can achieve as both outstanding educator and researcher.

To my wife, however, I owe the deepest thanks. She has been very supportive of me throughout this endeavour, having to put up with my working strange hours and everything else which is part of being a graduate student. We have known each other for almost a decade now, and her love and companionship through this period have been my life's greatest joy.

Table of Contents

List of Tables

List of Figures

Chapter 1

Introduction

This thesis presents the measurements of several quantities related to the production of bottom quark pairs at the Z^0. The $b\bar{b}$ event enrichment method employed for these measurements used the vertex detector system of the Mark II detector at the SLAC Linear Collider. This system provides very accurate track measurements. In particular, the average impact parameter resolution, including the uncertainty in the e^+e^- interaction point (IP) location, is about 30 μm for high momentum tracks and about 75 μm for tracks with 1 GeV/c of momentum transverse to the beam axis. The property used to identify potential $b\bar{b}$ events is that tracks from B hadron decay will tend to have impact parameters (b) inconsistent with the track having originated at the IP.

The specific technique for selecting a $b\bar{b}$ enriched sample requires that there be at least n_{min} tracks which have an impact parameter significance, b/σ_b, greater than some minimum value S_{min}. Typical values for tags used in this analysis have n_{min} = 3 and S_{min} = 3.0. With a detector of the above resolution, this tag selects $b\bar{b}$ events with an efficiency of 50%. The resulting tagged sample has a $b\bar{b}$ event purity of 85%.

This tagging method was employed to make several measurements. These measurements include,

- the hadronic branching fraction of the Z^0 to bottom quark pairs,
- the non-leading multiplicity in $b\bar{b}$ events, and

- the average energy fraction of bottom hadrons.

The hadronic branching fraction to $b\bar{b}$ events, F_b, is of interest because, with the statistics available to the analysis, it provides a check of the Standard Model couplings to a particular flavor of quark. With larger data samples, a measurement of F_b is sensitive to the top quark mass through electroweak corrections and also to potential sources of new physics. Using the impact parameter tag to measure F_b is also of interest because it will have different sources of systematic error from the other tags used in previous measurements.

With a $b\bar{b}$ enriched sample, the non-leading multiplicity in $b\bar{b}$ events can be determined. The non-leading multiplicity is defined as the average number of the tracks not from the decay of heavy hadrons, namely those tracks which are produced during the fragmentation process. The quantity directly measured in this determination of the non-leading multiplicity, is the difference between the multiplicity of the tagged sample and the multiplicity of the total hadronic sample. The difference between the $b\bar{b}$ event multiplicity and the Z^0 decay multiplicity was then calculated, after accounting for the effects of detector acceptance and bias introduced by the tagging method. The $b\bar{b}$ event multiplicity was determined by adding the multiplicity difference to the average total hadronic Z^0 decay multiplicity as measured by other experiments. The multiplicity of the non-leading system was then extracted by subtracting the B hadron decay multiplicity. The measurement of the multiplicity difference, rather than the $b\bar{b}$ event multiplicity, significantly reduces the sensitivity of the measurement to the systematic errors which affect all types of hadronic events similarly (*e.g.* tracking efficiency, pair production, *etc.*).

The principle purpose of this measurement is as a qualitative check of QCD phenomenology. As explained by QCD, the fragmentation process is governed by a quark and gluon shower and is thus expected to be independent of the flavor of the initial quark. To test this, the non-leading multiplicity measurement can be compared to the total hadronic multiplicity measured at a center of mass energy, which is equal to the energy of the non-leading system. Alternatively, if this flavor independence is assumed, one can extract the energy of the non-leading system by a similar comparison to the multiplicity measurements at lower center of mass energies. The average energy fraction of bottom hadrons, $\langle x_E \rangle_b$, is then determined from this non-leading energy measurement. Although the available event sample precludes a measurement of $\langle x_E \rangle_b$ with errors comparable to the present measurements, this approach has much different systematic errors than the

conventional method of using the momentum spectra of the leptons from semileptonic B decay to determine $\langle x_E \rangle_b$.

This chapter begins with a brief review of the Standard Model and, in particular, the electroweak couplings which govern the decay of the Z^0. The production of $b\bar{b}$ events is discussed along with the various corrections to R_b. The experimental methods used to select enriched $b\bar{b}$ event samples are surveyed, and the impact parameter tagging method used in this analysis is introduced. A summary of the present status of the determination of R_b by other experiments is given and the limiting source of systematic error in these measurements is discussed. Finally, the motivation for the measurement of the non-leading multiplicity is reviewed in more detail and the similar measurements made at PEP and PETRA are summarized.

1.1 The Standard Model

The goal of particle physics is to understand the nature and interactions of the most basic components of matter. The previous 25 years have been ones of great progress toward the achievement of this goal. In particular, the rise and longevity of the *Standard Model*, as a description of the most elementary particles and the forces which govern their behavior, is a testament to this progress.

The Standard Model* incorporates a small number of point-like, spin one-half particles, called *fermions*, to explain the composition of matter. These fermions are divided into two categories, *quarks* and *leptons*, which are each presently believed to contain at least six members (see Table 1–1). The quarks and leptons are divided into three similar generations, with the analogous particle in the next generation having a larger mass than that of the previous generation.

The forces at their most basic level are governed by integral spin particles, called *bosons*. Of the four forces that are known to exist, three have been included in the Standard Model. The *electromagnetic force* is governed by the massless photon (γ). The *weak nuclear force* has three very massive mediating particles, the Z^0, W^- and W^+. One of the ultimate goals of particle physics is the unification of all of the forces into one theory. To this end, the electromagnetic and weak forces were predicted to be different aspects of a single underlying force in the *electroweak theory* of Glashow, Salam and Weinberg.[2] The discovery in 1983 of the Z^0, W^-

* A complete discussion of the Standard Model is beyond the scope of this thesis and only a brief overview of the relevant material is presented herein. There are many very good sources of further information available — see Reference [1].

	Quarks	Leptons
1st generation	up (u) $q = +2/3$	electron neutrino (ν_e) $q = 0$
	down (d) $q = -1/3$	electron (e^-) $q = -1$
2nd generation	charm (c) $q = +2/3$	muon neutrino (ν_μ) $q = 0$
	strange (s) $q = -1/3$	muon (μ) $q = -1$
3rd generation	top (t) $q = +2/3$	tau neutrino (ν_τ) $q = 0$
	bottom (b) $q = -1/3$	tau (τ) $q = -1$

Table 1–1 The known quarks and leptons are listed with their electric charge (q), in units of e. Note that the top quark and the tau neutrino have not been directly observed.

and W^+ at the masses predicted by this theory was the conclusive evidence of its validity.[3]

The theory which explains the strong nuclear force is *quantum chromodynamics* (QCD). In this theory, the strong interactions are governed by the exchange of massless gluons (g) between particles which carry color charge. This color charge has three types, which are called red, green and blue. Of the fermions, only quarks carry color charge. The gluons also carry color charge, however, and thus gluons can interact with themselves, leading to two important consequences. The first is that at small distances, an anti-screening effect occurs which reduces the amount of color charge seen around a quark. This results in the property of *asymptotic freedom*, and implies that at very small distances the quark-quark and quark-gluon forces will be quite weak and the quarks will behave rather like free particles. The second effect is that the color flux lines between the quarks are pulled into a tube due to the gluon-gluon interactions. The inter-quark potential thus rises linearly with the distance between the quarks resulting in *quark-confinement*. Because of quark confinement, quarks are only observed in various bound systems such as *mesons* (a quark-antiquark pair) and *baryons* (three quarks). These mesons and baryons are known collectively as *hadrons*. As the separation between quarks gets quite large the energy stored in the strong field between the quarks becomes large enough to create a quark-antiquark pair from the vacuum. As a result of the

renormalization process, the coupling strength of the strong force varies as a function of energy such that at high energies (the asymptotically free regime), the coupling strength, α_s, is small and thus perturbation theory can be used to calculate the various effects. At lower energy, though, α_s becomes larger and the perturbation theory is no longer of much value. These energies are, however, of critical importance in understanding the production of hadrons from quarks, a process known as fragmentation. Consequently, this process must be described by physically-motivated models, such as those described in Chapter 3.

Finally, gravity is not included in the Standard Model, largely because of theoretical problems in building a suitable theory. This does not pose any difficulty for measurements such as that presented herein, because the strength of the gravitational attraction at the distances considered by the interaction of these elementary particles is far less than that of the other three forces.

1.2 Electroweak Couplings

The electroweak theory is based on an $SU(2)_L \times U(1)$ gauge group and the principle of local gauge invariance. The $SU(2)_L$ is a weak isospin group with a V – A structure such that it only couples to the left-handed fermions (hence the subscript 'L'). The U(1) is the electromagnetic symmetry group, which couples to right and left-handed fermions. Upon mixing the B_μ and W^3_μ fields of the U(1) and $SU(2)_L$ groups, one can generate four massless fields:

$$W^{\pm} = \sqrt{\frac{1}{2}}(W^1 \pm W^2)$$

$$Z_\mu = B_\mu \cos\theta_W + W^3_\mu \sin\theta_W \qquad (1\text{-}1)$$

$$A_\mu = -B_\mu \cos\theta_W + W^3_\mu \sin\theta_W .$$

These fields correspond to the $W^{\pm}$, Z^0 and γ gauge bosons, respectively. The process by which the mass of the $W^{\pm}$ and Z^0 is generated is the Higgs mechanism. This involves introducing a complex Higgs doublet from which three of its four degrees of freedom are used to provide the extra degrees of freedom necessary to form massive bosons. The remaining degree of freedom generates a scalar particle, the Higgs boson, which has not yet been discovered.

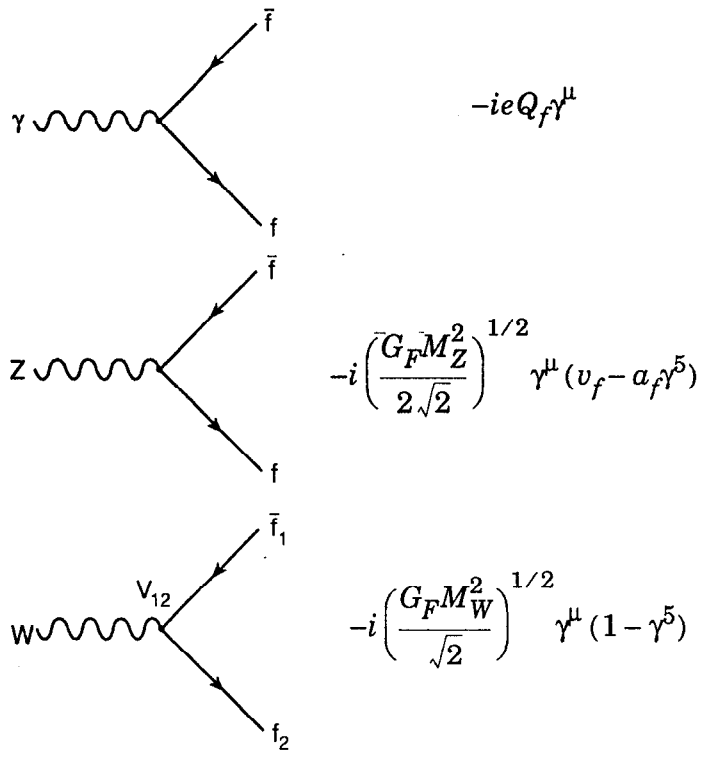

Figure 1–1 Feynman diagram vertex factors for the neutral and charged electroweak interactions.

The electroweak couplings between the fermions and the gauge bosons are given by the Feynman diagram vertex factors in Figure 1–1. These factors are written in terms of the vector and axial vector couplings, defined for a fermion of type f as

$$v_f = 2(T_f^{3L} - 2Q_f \sin^2\theta_W) \tag{1-2}$$

$$a_f = 2T_f^{3L} \tag{1-3}$$

where Q_f is the electric charge in units of the positron charge, and T_f^3 is the projection of the weak isospin onto the z-axis. The values of these constants are given in Table 1–2. It is also interesting to note that the $Z^0 f\bar{f}$ vertex factor can be re-written in a form which clearly exhibits the right and left-handed contributions:

$$-i\left(\frac{G_F M_Z^2}{2\sqrt{2}}\right)^{1/2}\gamma^\mu(v_f - a_f\gamma^5) = -i\left(\frac{G_F M_Z^2}{2\sqrt{2}}\right)^{1/2}\gamma^\mu[R_f(1+\gamma^5) + L_f(1-\gamma^5)], \tag{1-4}$$

Fermion type	Q_f	T_f^{3L}	a_f	v_f
u, c, t	+2/3	1/2	1	$1-\frac{8}{3}\sin^2\theta_w \approx 0.38$
d, c, b	–1/3	–1/2	–1	$-1+\frac{4}{3}\sin^2\theta_w \approx -0.68$
ν_e, ν_μ, ν_τ	0	1/2	1	1
e, μ, τ	–1	–1/2	–1	$-1+4\sin^2\theta_w \approx -0.06$

Table 1–2 The electric charge, the z-component of the weak isospin, and the axial-vector and vector couplings for the quarks and leptons in the electroweak theory. For right-handed fermions, $T_f = 0$. The numerical values for the vector coupling strengths are calculated for $\sin^2\theta_w = 0.231$.[4]

where,

$$R_f = \frac{1}{2}(v_f - a_f) = -2Q_f \sin^2\theta_W$$

$$L_f = \frac{1}{2}(v_f + a_f) = 2T_f^3 - 2Q_f \sin^2\theta_W.$$

There is one more small complication: the weak eigenstates of the quarks are different from their mass eigenstates. The left-handed eigenstates, namely those which participate in the charged-current interactions, are related by a 3×3 unitary, complex matrix known as the Kobayashi-Maskawa matrix.[5] By convention, the charge –1/3 quarks are chosen to be related by this matrix such that the weak eigenstates (primed) are given in terms of the mass eigenstates (un-primed) by

$$\begin{pmatrix} d'_L \\ s'_L \\ b'_L \end{pmatrix} = \begin{pmatrix} V_{ud} & V_{us} & V_{ub} \\ V_{cd} & V_{cs} & V_{cb} \\ V_{td} & V_{ts} & V_{tb} \end{pmatrix} \begin{pmatrix} d_L \\ s_L \\ b_L \end{pmatrix}. \tag{1-5}$$

This matrix has four free parameters: three angles and one complex phase.

1.3 Bottom Quark Production at the Z^0 Resonance

The production of quarks through electron-positron annihilation proceeds via two primary channels as illustrated in Figure 1–2. The cross section to produce hadronic events generally falls off as $1/s$ (where $s = E_{cm}^2$) in the energy region where the photon-exchange diagram dominates. At the center of mass energy around the mass of the Z^0, there is very large resonance. One can characterize the

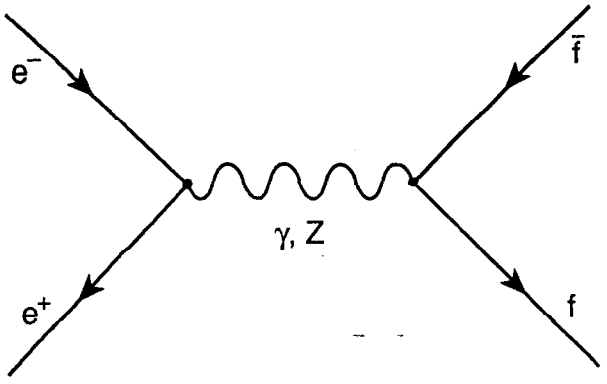

Figure 1–2 Electron-positron annihilation to an electroweak boson and the subsequent decay into a fermion-antifermion pair.

size of a resonance by comparing it to the point cross section for muon production, $\sigma_{pt} = 4\pi\alpha^2/3s$. The ratio of the cross section for producing hadronic events to σ_{pt} is referred to as R. At $E_{cm} = m_Z$, R is approximately 2900 (after correcting for the ~30% effect of initial state radiation).[6] This analysis is based on data from electron-positron annihilations at a center of mass energy of about 91 GeV.

1.3.1 Branching Fraction of the Z^0 to Fermions

The partial width of the Z^0 decay into a fermion-antifermion pair can be calculated in the Born approximation, given the vertex factors from Figure 1–1. The amplitude for this decay is

$$\boldsymbol{M}_{Z\to f\bar{f}} = -i\left(\frac{G_F M_Z^2}{2\sqrt{2}}\right)^{-1/2} \varepsilon_\mu^\lambda \, \bar{f}\gamma^\mu (a_f - v_f\gamma^5) f, \tag{1-6}$$

where ε_μ^λ is the polarization vector of the Z^0, and f and $\bar{f}$ are the fermion and antifermion spinors. The partial width for a two-body decay is given by:

$$\Gamma(Z^0 \to f\bar{f}) = \frac{1}{64\pi^2}\frac{s\beta}{M_Z^3}\int \left|\boldsymbol{M}_{Z\to f\bar{f}}\right|^2 d\Omega_{cm}, \tag{1-7}$$

where β is the speed of the fermion, equal to $\sqrt{1-4m_f^2/s}$. Thus, the resulting partial width for massless quarks is:

$$\Gamma(Z^0 \to f\bar{f}) = n_c\frac{G_F M_Z^3}{24\sqrt{2}\pi}(a_f^2 + v_f^2) = \frac{1}{2}n_c(a_f^2 + v_f^2)\,\Gamma_Z^0, \tag{1-8}$$

where n_c is a color factor which is 3 for quarks and 1 for leptons. In the last part of the expression $\Gamma_Z^0 = \Gamma(Z^0 \to \nu\bar{\nu}) \approx 0.17$ GeV.

The hadronic branching fraction of the Z^0 into a $b\bar{b}$ pair is defined as

$$F_b = \frac{\Gamma(Z^0 \to b\bar{b})}{\Gamma(Z^0 \to \text{hadrons})}. \tag{1-9}$$

In the absence of the production of additional flavors beyond bottom, the denominator is just the sum of the partial widths of the Z^0 to decay into the five flavors of quarks:

$$\Gamma(Z^0 \to \text{hadrons}) = \Gamma_u + \Gamma_d + \Gamma_s + \Gamma_c + \Gamma_b. \tag{1-10}$$

The tree level partial widths and hadronic branching fractions are given in Table 1–3.The total width of the Z^0 is about 2.5 GeV; the total hadronic width is about 1.7 GeV.

Fermion type (per channel)	$\Gamma(Z^0 \to f\bar{f})$	$\frac{\Gamma(Z^0 \to f\bar{f})}{\Gamma(Z^0 \to \text{had})}$
u, c	0.29 GeV	17%
d, s, b	0.37 GeV	22%
ν_e, ν_μ, ν_τ	0.10 GeV	—
e^-, μ^-, τ^-	0.17 GeV	—

Table 1–3 Estimates of the tree level, massless fermions partial widths and branching fractions, calculated for M_Z = 91.1 GeV and $\sin\theta_w$ = 0.231.[4] The coupling strengths used are given in Table 1–2.

The measurement of the branching fraction involves selecting the $b\bar{b}$ events from the *udsc* events with some known efficiencies, because in a given sample of Z^0 decays, F_b is calculated from the ratio of the number of $b\bar{b}$ events to the total number of events. Methods for selecting a sample of $b\bar{b}$ events are introduced in Section 1.4. The details of relating F_b to the fraction of events tagged as $b\bar{b}$ are found in Chapter 6.

1.3.2 Corrections to the Tree Level Branching Fraction

There are a number of corrections to this massless-quark, Born approximation calculation of the partial width. The first of these is the mass of the quark which is produced. With a non-zero mass, Equation (1-8) becomes

$$\Gamma(Z^0 \to f\bar{f}) = n_c \frac{G_F M_Z^3}{24\sqrt{2}\pi} \beta \left[\beta^2 a_f^2 + \left(\frac{3-\beta^2}{2} \right) v_f^2 \right]. \tag{1-11}$$

For bottom quarks at the Z^0, this correction is about –1.2%.

QCD Corrections

The radiation of soft gluons from the final state quarks is the source of the largest corrections due to QCD. To first order, the effect of these corrections is equivalent to the substitution into Equation (1-11) of [7]

$$a_f^2 \to a_f^2 \left\{ 1 + \frac{4}{3}\alpha_s \left[\frac{\pi}{2\beta} - \left(\frac{19}{10} - \frac{22}{5}\beta + \frac{7}{2}\beta^2 \right) \left(\frac{\pi}{2} - \frac{3}{4\pi} \right) \right] \right\} \tag{1-12}$$

$$v_f^2 \to v_f^2 \left\{ 1 + \frac{4}{3}\alpha_s \left[\frac{\pi}{2\beta} - \left(\frac{3+\beta}{4} \right) \left(\frac{\pi}{2} - \frac{3}{4\pi} \right) \right] \right\}. \tag{1-13}$$

In these expressions, the strong coupling constant α_s is given by [8]

$$\alpha_s(\mu) = \frac{12\pi}{(33-2n_f)\ln(\mu^2/\Lambda^2)} \left[1 - \frac{6(153-19n_f)\ln[\ln(\mu^2/\Lambda^2)]}{(33-2n_f)^2 \ln(\mu^2/\Lambda^2)} \right], \tag{1-14}$$

where μ is the energy scale, n_f is the number of quarks with mass less than μ and Λ is the QCD scale parameter. As $\beta \to 1$, these correction factors approach the same value of $(1+\alpha_s/\pi)$, which for a value of $\alpha_s = 0.123$ produces a correction of about 4%. Second and third order corrections have been calculated in the massless quark limit and are believed to be less than 1%.[9] Because this correction affects all quark flavors similarly, measuring the branching ratio instead of the partial width significantly reduces the contribution from this correction and the associated uncertainty in the value of α_s.

QED Corrections

In an analogous fashion to the QCD corrections discussed above, corrections due to pure QED process such as photon radiation and exchange between the final fermions can also be calculated. The result is a multiplicative correction factor of $(1+3\alpha Q_f^2/4\pi)$ for the partial width.[10] For bottom quarks this correction is

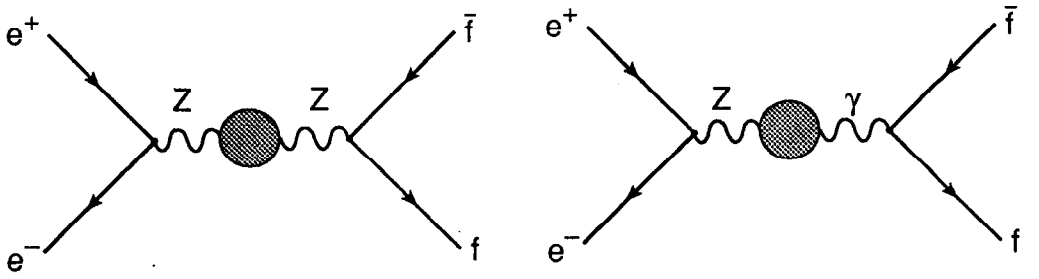

Figure 1–3 Examples of oblique corrections, including the γ-Z mixing diagram.

0.019%. The largest correction, that for the charged leptons, is 0.17%. Photon radiation from the initial state electron and positron reduces the peak cross section by ~30% as noted previously. Its affect on the partial widths, however, is only ~3%. Both of these QED corrections cancel in the branching ratio.

Electroweak Corrections

The genuine electroweak corrections can be divided into two categories: the corrections to the propagators via vacuum polarization diagrams (oblique corrections — see Figure 1–3) and the corrections to the final state vertex. The oblique corrections can be calculated using formalism such as that of Kennedy and Lynn[11] which allows the calculation of these corrections to all orders. These corrections are essentially the same for all flavors of quarks. The vertex and fermion self-energy corrections have been calculated by a number of authors.[12][13][14] They are of particular interest because $Z^0 \to b\bar{b}$ events have vertex and self-energy contributions from the yet unseen top quark. This is the case because the Kobayashi-Maskawa matrix element V_{tb} is expected to be approximately unity. The diagrams which contribute to the top quark coupling are shown in Figure 1–4. These additional contributions actually reduce the dependence of $\Gamma(Z^0 \to b\bar{b})$ on the top mass relative to that of $\Gamma(Z^0 \to d\bar{d})$ because of cancellations between the oblique and vertex corrections.[13][15][16] Specifically, the m_t^2-dependence of the branching fraction that results from the oblique corrections almost entirely cancels with that from the vertex diagrams. This leaves a term proportional to $\ln(m_t^2/M_Z^2)$ which, depending on the top mass, can be twice as large as original oblique correction. This logarithmic term also has the opposite sign than that of the oblique correction (see Figure 1–5). A very thorough compilation of the expected effects on the partial widths can be found in Reference [13]. Because of these additional top quark contributions to the vertex diagrams, the study of the $Z^0 \to b\bar{b}$ channel provides a tool with which one can

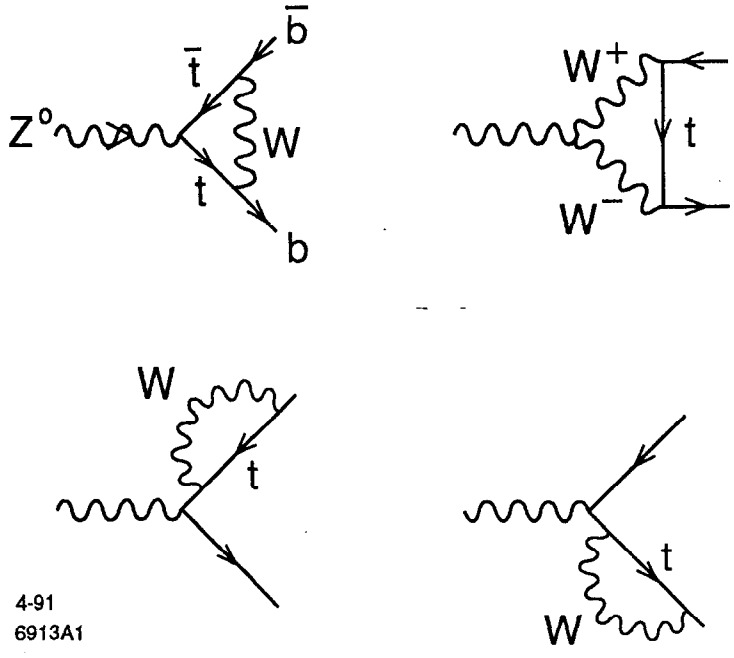

Figure 1–4 Contributions to the Z^0-$b\bar{b}$ vertex from the top quark.

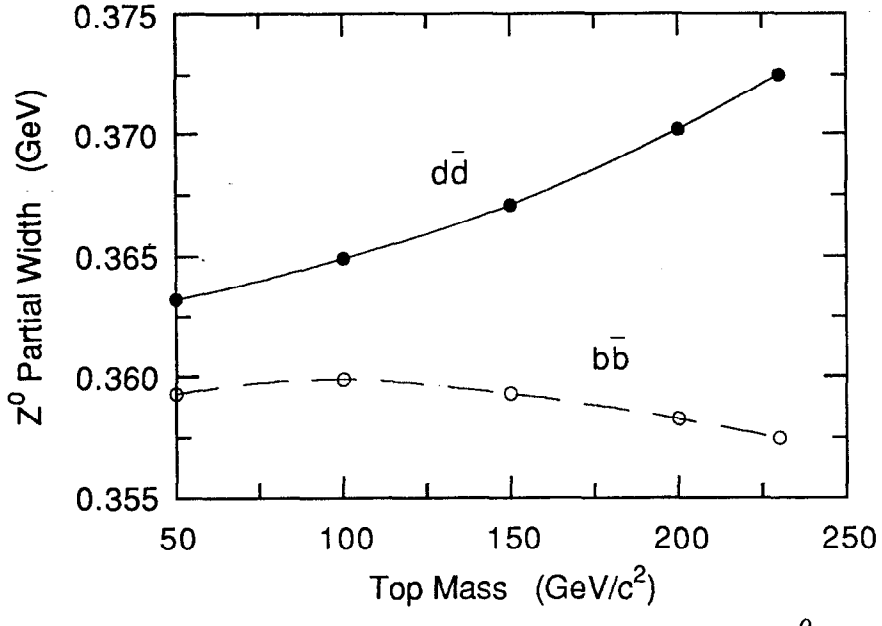

Figure 1–5 The dependence of the partial widths of the Z^0 to decay to down and bottom quark pairs. The points were calculated by W. Hollik for M_Z = 91 GeV/c^2 and a Higgs mass of 100 GeV/c^2. The lines are an interpolation between these points.[13]

attempt to separate the effects due to the top quark from those due to other new physics (see Section 1.3.3).

Finally, it should be noted that the variation of mass of a neutral Higgs boson, which is predicted to be present in the minimal Standard Model, has a very small effect on the partial width (less than 10 MeV).

1.3.3 Contributions from Exotic Phenomena

There are a number of mechanisms beyond the minimal Standard Model, which can affect the branching fraction to $b\bar{b}$. These extensions to the Standard Model include the possibility of additional Z bosons, the supersymmetry theory and the addition of a second Higgs doublet without all of the supersymmetric contributions. Djouadi *et al.* have presented a consistent strategy for disentangling these extensions from the $Zb\bar{b}$ vertex itself which involves measuring several quantities at accuracies requiring a very large event sample.[15]

Extra Z Boson: the Z'

In higher dimensional symmetry groups favored by Grand Unified Theories, it is possible to generate additional weak vector bosons.[17] Direct searches for the Z' with couplings similar to that of the Z at hadron colliders have set lower limits on the mass at 173 GeV/c^2 (UA1, 90% C.L.), 180 GeV/c^2 (UA2, 90% C.L.) and 412 GeV/c^2 (CDF, 95% C.L.).[18] Also, given a particular choice of symmetry group, indirect limits can be set on Z' mass given the Z, W and top quark masses.[19] The effects of the presence of a Z' on the partial width to $b\bar{b}$ is considered in Reference [15] and can vary significantly depending on the assumptions as to the source of the new boson.

Second Higgs Doublet

Although one Higgs doublet is required to generate the mass of quarks and bosons, more doublets are possible. This produces a pair of charged Higgs scalars which would lead to a number of new vertex diagrams shown in Figure 1–6(a). The effect of these additional diagrams on F_b has been calculated and is shown in Figure 1–7.[16] Again, precision measurements may make it possible to determine the presence of an additional Higgs doublet.

Supersymmetry

Supersymmetry (SUSY) is an attempt to resolve the vast difference in mass scales between the 10^{16} GeV mass scale of Grand Unified Theories and the much lighter mass scales of the Z and W around 100 GeV.[20] In unifying the treatment of the quark, leptons and gauge bosons, SUSY requires that every fundamental

particle have a supersymmetric partner with the same charge and color, but with a spin which differs by 1/2. The resulting partners of the quarks and leptons are the spin 0 squarks and sleptons. Similarly, the photon, *Z*, *W*, gluon and Higgs are paired with the photino, zino, wino, gluiono and higgsino, respectively, all of which have spin 1/2. Additionally, a second Higgs doublet is also required by SUSY. At the present, there has been no experimental observation of any of these partners.[8][21] Some of the diagrams containing these new particles, which will contribute to modifying F_b, are shown in Figure 1–6. The net result of these new diagrams on F_b has been calculated.[15][16] The result of Boulware and Finnell for a particular minimal SUSY model is shown as a function of the top quark mass in Figure 1–7.* The central line in this figure is the prediction of the minimal Standard Model and the upper line is the minimal supersymmetric model. Even for a very large top mass, the difference between these curves is about 1%, which is about the same magnitude as the variation in the minimal Standard Model for the reasonable range of top mass. However, with the combination of other precision measurements (such as the Z and W masses) and a precise determination of F_b it may be possible to find indirect evidence of supersymmetry and untangle it from the effects of the top quark.

1.4 Experimental Methods for Identifying *b* Events

In order to study properties of *B* hadrons, it is necessary to select an event subset which is enriched with $Z^0 \to b\bar{b}$ events. In particular, the goal of the tagging algorithm is both to tag the $Z^0 \to b\bar{b}$ events efficiently and have a high $Z^0 \to b\bar{b}$ purity in the tagged sample of events.

The B hadron has several properties which are relevant to tagging $Z^0 \to b\bar{b}$ events. These include,

1. *B* hadrons have much larger mass than other hadrons;[8]
2. *B* hadrons tend to be produced from fragmentation with a substantial fraction of the beam energy (~0.7);[22][23][24]
3. The mean lifetime of *B* hadrons is about 1.3 psec,[8][25] which with the rather hard fragmentation and the high energy at the Z^0, corresponds to a decay length of ~2 mm. Furthermore, because of the small value of V_{ub},[26] *B* hadrons decay almost exclusively into *D* hadrons which also

* As noted by Boulware and Finnell[16] their result for the supersymmetric contributions to the $Zb\bar{b}$ vertex differs in sign from that of Djouadi *et al.*[15] The latter find that the contribution of the charged Higgs and true supersymmetric contributions have the same sign, whereas the former find these to have the opposite sign.

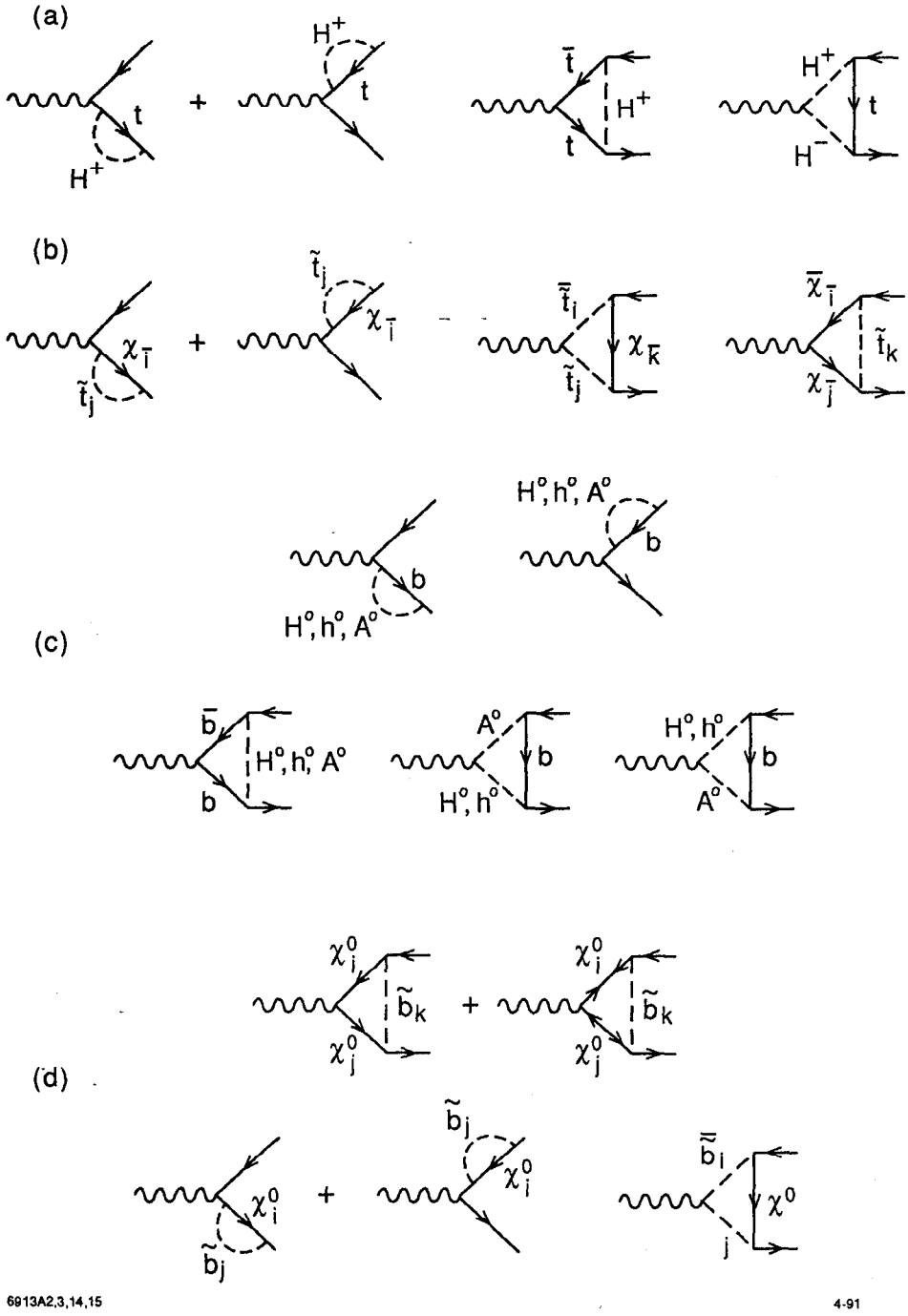

Figure 1–6 Supersymmetric contributions to bottom quark production from Z^0 decay: (a) charged Higgs, (b) charginos (χ), (c) neutral scalars, and (d) neutralinos.[16] The charginos and neutralinos are, respectively, the mixtures of the charged and neutral gauginos and higgsinos.

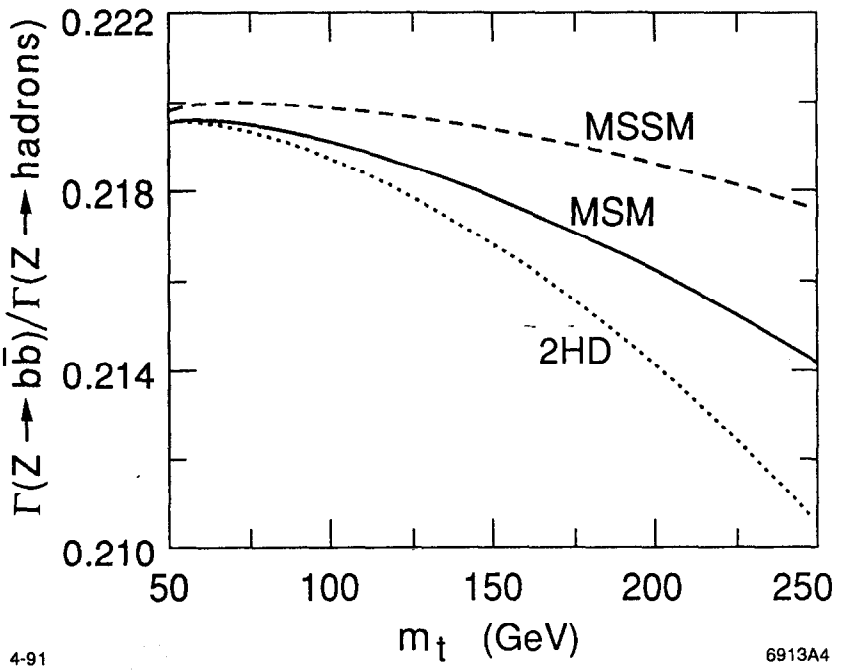

Figure 1–7 The dependence of the branching fraction of the Z^0 to bottom quarks for several models: the minimal Standard Model (MSM), the addition of a second Higgs doublet (2HD), and the minimal supersymmetric model (MSSM), as calculated by Boulware and Finnell.[16] The MSSM calculation assumes tanβ = 1 (relative size of the vacuum expectation values of the two Higgs doublets), M = 50 GeV (W-ino mass matrix parameter), μ = 30 GeV (coupling between the two Higgs fields), and *m(top squark)* = $M(H^+)$ = 100 GeV. This combination of values was chosen to illustrate a maximal effect.

have significant lifetimes, ranging from 0.4 to 1.0 psec, depending on the type of D.[8]

As described below, the high p and p_T lepton tag and the boosted sphericity product tag use these first two properties, which imply that tracks from B decay will tend to have a large total momentum (p) and also a large momentum component in the direction transverse to the event axis (p_T).

The third property of the B hadron decay implies that $Z^0 \rightarrow b\bar{b}$ events will have a rich vertex structure, which distinguishes them from *uds* and to some extent charm events. Figure 1–8 illustrates this vertex structure for a typical light quark and $b\bar{b}$ event. Indications of this vertex structure are potentially resolvable with state-of-the-art tracking detectors. Figure 1–9 shows the same events as Figure 1–8, except that the tracks have been reconstructed after detector

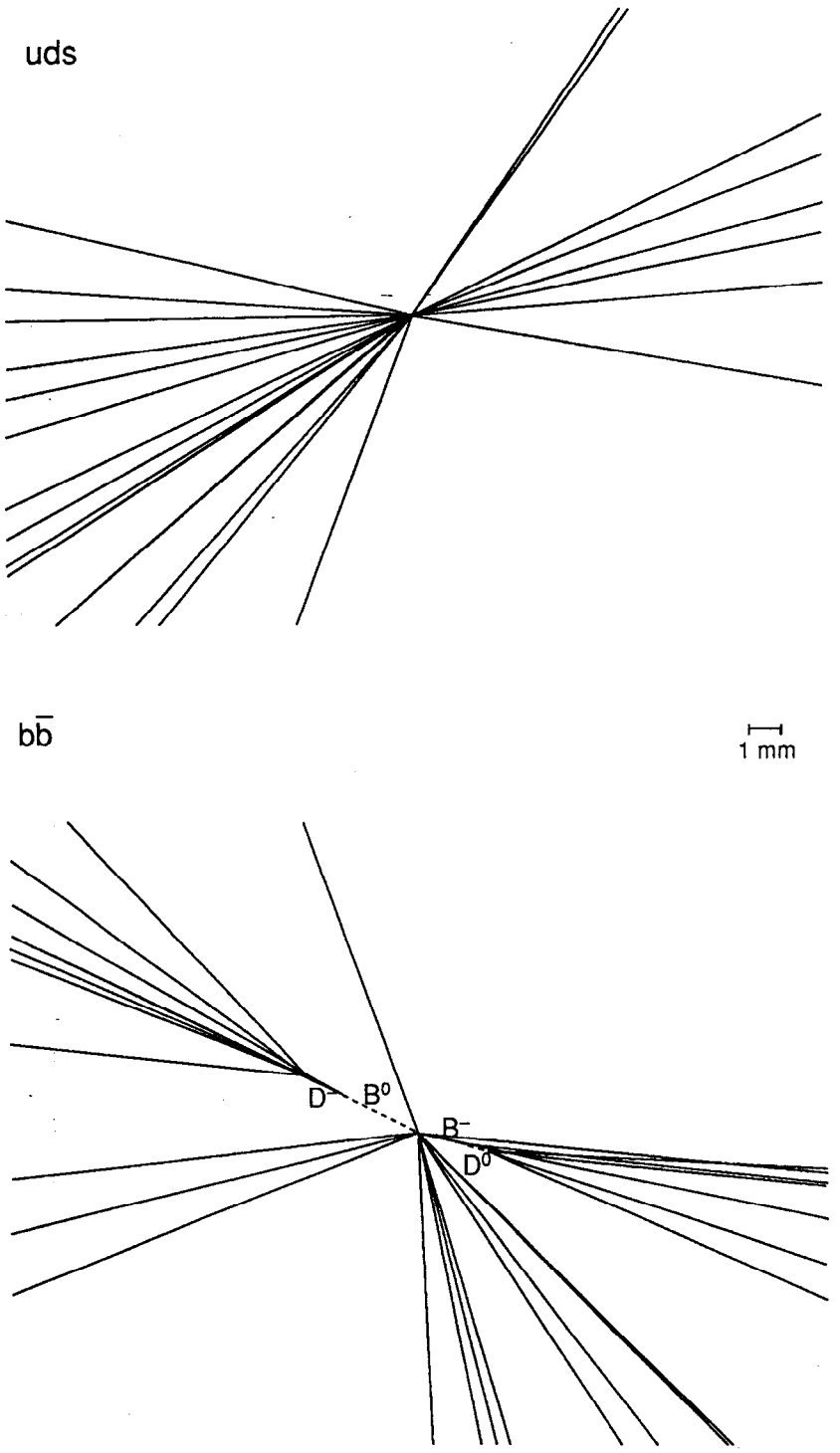

Figure 1–8 Monte Carlo events showing the generated particle trajectories. The upper event is a light quark event and the lower is a bottom quark event, showing the B and D decay vertices.

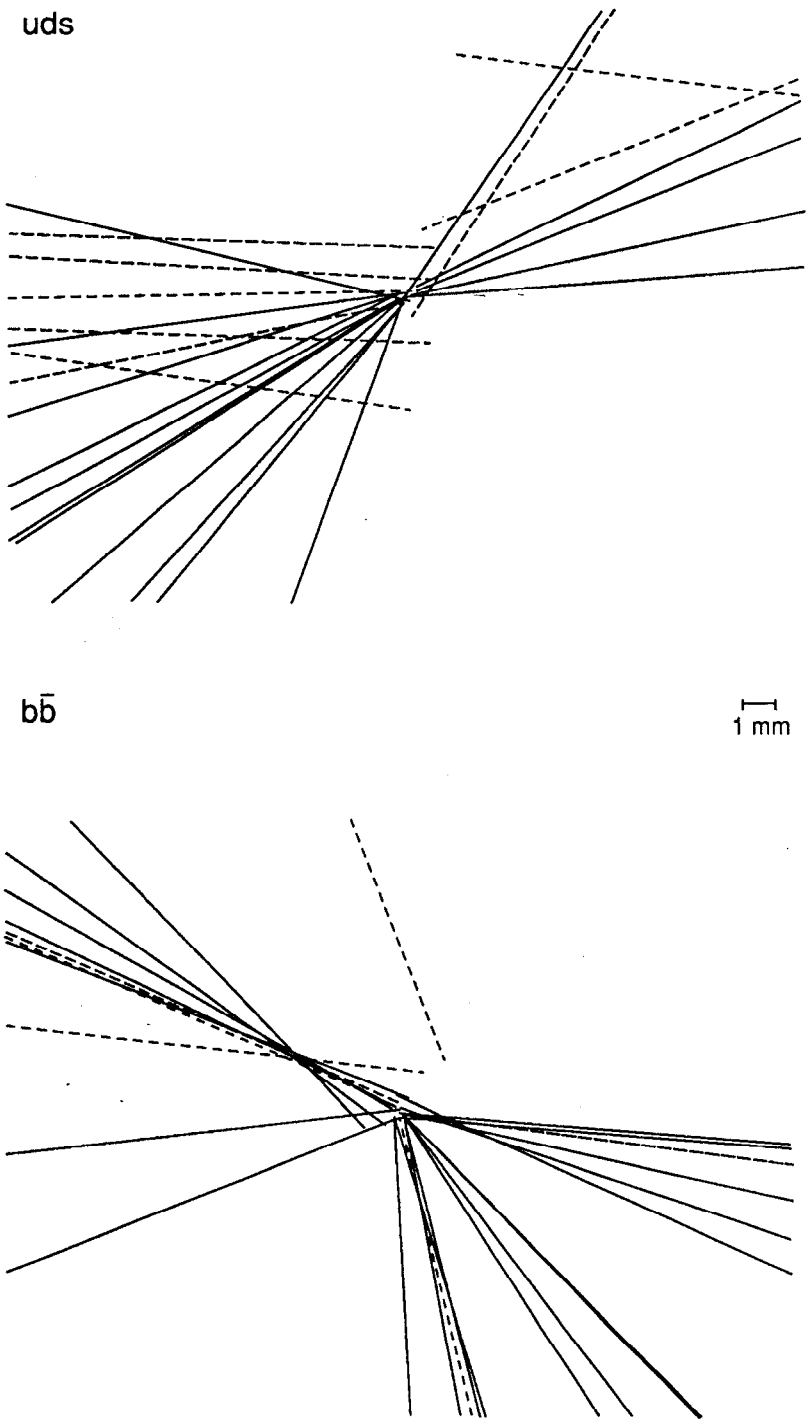

Figure 1–9 Monte Carlo events showing the tracks reconstructed after the Mark II detector simulation. The upper event is a light quark event and the lower is a bottom quark event. These are the same events as shown in Figure 1–8. The tracks represented as dashed lines failed track quality cuts.

simulation. Note that the vertex structure is now significantly more difficult to discern. Because of this, no attempt has been made to tag $Z^0 \to b\bar{b}$ events by fully reconstructing these vertices, primarily because of its low efficiency. Instead, the analyses use properties of the tracks which emanate from the secondary and tertiary vertices. At PEP and PETRA, the introduction of vertex detectors permitted new algorithms to be used to select $b\bar{b}$ events based on the positions of potential secondary vertices. The tag used in this analysis is also based on the use of precision tracking detectors, except that the algorithm only looks for tracks inconsistent with having originated from the location of the e^+e^- annihilation and does not do any fits for secondary vertices.

1.4.1 Lepton Tag

The high p and p_T lepton tag has been used by numerous groups to isolate $b\bar{b}$ events at PEP and PETRA, and more recently at the SLC[27] and LEP.[22][23][24] For the lepton tag, one searches for leptons from the semileptonic decay of the B hadron, $B \to Dl\nu$, requiring these leptons to have a large p and p_T. Typical cuts for selecting only the leptons from B decay, such as those used by OPAL,[24] are $p > 4.5$ GeV and $p_T > 1$ GeV. The branching fraction can then be extracted from the number of events which pass these criteria. Alternatively, the lepton p and p_T spectra can be fit using Monte Carlo predicted p and p_T distributions for all of the sources of leptons.

1.4.2 Boosted Sphericity Product Tag

The boosted sphericity product tag, originally developed by TASSO[28] and used at LEP by DELPHI,[29] uses the shape of the events to select a $b\bar{b}$-enriched event sample. Specifically, $b\bar{b}$ events will, because of the large B mass, tend to be less collimated than *udsc* events. The event-shape variable sphericity, S, is used to quantify this difference in event shape. It is defined as

$$S = \frac{3}{2}\min\left(\frac{\sum_i \left|\vec{p}_i \times \hat{S}\right|^2}{\sum_j \left|\vec{p}_j\right|^2}\right), \tag{1-15}$$

where the sum i is over tracks and the unit vector $\hat{S}$ is that which minimizes the momentum sum.

The algorithm consists of calculating the sphericity separately in each hemisphere defined by the plane perpendicular to the event sphericity axis, after

boosting the tracks in each hemisphere to the rest frame of the average B hadron (TASSO used β=0.74 at E_{cm} = 35GeV and DELPHI used β=0.96 at 91 GeV). The product of the jet sphericities, S_1S_2, is then used to separate the $b\bar{b}$ sample. TASSO used a fixed cut requiring that $S_1S_2 > 0.18$ to select the enriched event sample which it used for B lifetime measurements. DELPHI has fit the S_1S_2 spectrum between 0.1 and 0.5 to a pair of Monte Carlo predicted S_1S_2 distributions for $b\bar{b}$ and *udsc* events weighted by the fraction of $b\bar{b}$ events.

1.4.3 Vertex Detector-Based Tags: PEP and PETRA

Algorithms were developed at PEP and PETRA which used information from their vertex detectors as indicators of $b\bar{b}$ events. P. Weber[30] developed a vertex search algorithm used with the Mark II at PEP. This algorithm initially fit all of the tracks in an event to a common vertex, removing those tracks necessary to achieve a fit probability of some minimum value. Secondary vertices were then sought in the events and $b\bar{b}$ candidate events selected with the requirements that the vertex contain at least four tracks, have a positive decay length, and lie close to the expected flight path as determined by the thrust axis.

The TASSO Collaboration[31] developed an enrichment method that did not attempt to reconstruct a multitrack B decay vertex, but instead fit a vertex using each track pair. Each of these vertices were assigned a weight based upon distance to the beam spot, and the angle between the momentum sum of the tracks in the vertex and the line connecting the two-track vertex to the beam position. These individual vertex weights were then summed, either by event or jet, and a fixed cut was used to select the $b\bar{b}$-enriched event sample.

1.4.4 Impact Parameter Tag

Instead of fitting tracks to vertices, the tag used by this analysis simply looks for tracks which are inconsistent with the electron-positron interaction point (IP).* The IP used in this analysis is one which is determined with a fitting algorithm on an event-by-event basis. The variable used to measure the distance of a track from the IP is the impact parameter, b (see Figure 1–10). However, the resolution with which the impact parameter can be measured for a given track may vary significantly with the track's momentum and angle, and the number of position measurements associated with that track. Thus, it is useful to use the impact parameter

* The details of this algorithm and the use of impact parameters are discussed in subsequent chapters. For more information on impact parameters and the impact parameter measurement resolution of the tracking detectors refer to Chapter 4. For the specifics of the tagging method see Chapter 5.

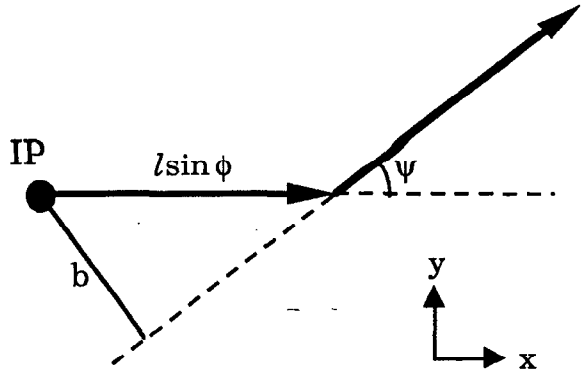

Figure 1–10 Definition of the impact parameter b. For a parent particle which traveled a distance l at an angle ϕ with respect to the beam axis, and then decayed into a daughter at an angle ψ from the parent's direction, the projection of the impact parameter into the plane perpendicular to the beam axis is given by $l\sin\psi\sin\phi$. The projection of the impact parameter is used because the precision vertex detectors only measure the tracks in this plane.

significance, b/σ_b, where σ_b is the expected impact parameter resolution. The tagging algorithm then requires an event (or hemisphere) to have a minimum number of tracks of some minimum impact parameter significance. A typical tag requires at least three tracks with $b/\sigma_b > 3.0$. To further increase the signal-to-noise ratio of the tracks with large significance, the impact parameters are given an algebraic sign which is positive if the vector from the IP to the point where the track crosses the thrust axis makes an acute angle with respect to the track direction. The result of this is that most of the tracks from B decays have positive impact parameters, while tracks from *udsc* events are distributed more symmetrically about $b = 0$. The distribution of impact parameter significance as predicted by the Monte Carlo whose impact parameter resolution was tuned to that in the data is shown in Figure 1–11.

1.4.5 Other Tags

Other types of hybrid tags are also possible which incorporate a number of event properties to achieve statistically powerful tags. A multidimensional algorithm has been explored by ALEPH[32] and DELPHI[33] using Monte Carlo simulation. The use of neural networks also has been investigated by DELPHI[34] and used to measure the branching fractions to different flavors of events. The major drawback of these methods is the evaluation of the systematic error with such a complicated algorithm.

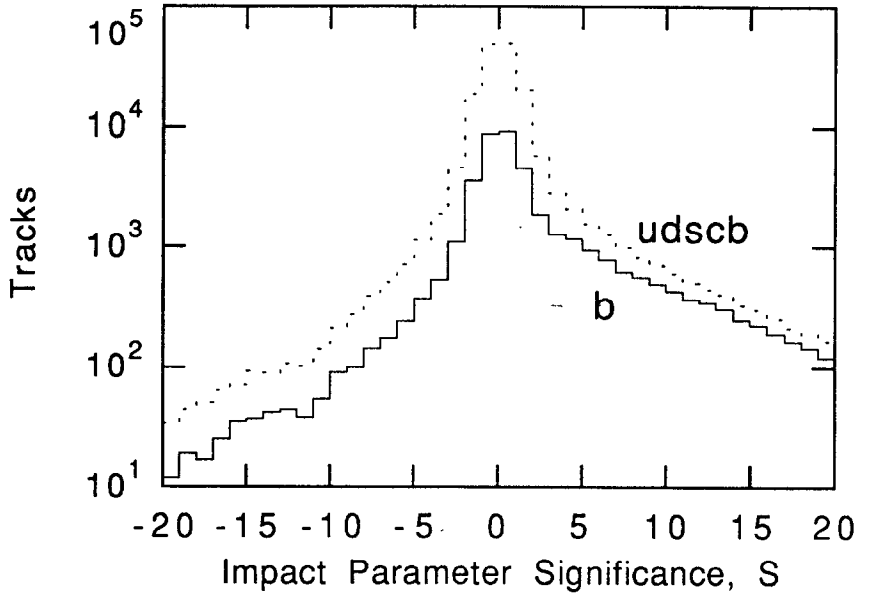

Figure 1–11 The impact parameter significance distributions for all flavors of hadronic events and the bottom flavor events. The asymmetry is the result of applying a sign to the impact parameter with the thrust axis. Note that the tracks from b events are the dominant contribution to the tracks with a positive impact parameter.

1.5 Measurements of the Branching Fraction to b Quarks

The measurement of the hadronic branching fraction of the Z^0 to decay into $b\bar{b}$ is well motivated for a number of reasons. With the statistics presently available, this provides a check of the Standard Model prediction for the Z^0 couplings to b quarks. When larger event samples are available, the increased sensitivity makes this an interesting window on the top quark as well as various possibilities of new physics as discussed in Sections 1.3.2 and 1.3.3 While this measurement has been done by a number of collaborations, the use of an impact parameter tag to measure F_b is potentially interesting because of the different sources of systematic error from the methods employed in the previous measurements.

All of the experiments at SLC and LEP have measured quantities related to F_b. A summary of these measurements and their quoted results is given in Table 1–4. Four experiments, Mark II,[27] ALEPH,[22] L3[23] and OPAL,[24] have used lepton tags and DELPHI[29] used the boosted sphericity product tag.

Experiment	Method	Quantity quoted
Mark II[27]	lepton tag (e & μ)	$F_b = 0.23^{+0.10+0.05}_{-0.09-0.04}$
ALEPH[22]	lepton tag (e & μ)	$F_b = 0.220\pm0.016\pm0.024$
L3[23]	lepton tag (e & μ)	$\Gamma_b = 385\pm7\pm22$ MeV
OPAL[24]	lepton tag (μ)	$F_b \cdot Br(B \to lX) = 0.0226\pm0.0007\pm0.0013$
DELPHI[29]	boosted sphericity product	$F_b = 0.209\pm0.030\pm0.031$

Table 1–4 Measurement of F_b and quantities related to F_b by the experiments at the SLC and LEP. The errors are statistical and systematic, respectively. To get their value for F_b, Mark II, ALEPH and L3 used 0.11 ± 0.01, 0.102 ± 0.010 and 0.117 ± 0.006 respectively as the B decay semileptonic branching ratio.

To compare the results of the lepton tag measurements, it is useful to compare the quantity which is actually measured with this tag, namely the product of F_b and the branching fraction of the B hadron to leptons, $F_b \cdot Br(B \to lX)$. In order to convert the L3 value for Γ_b into F_b, their measured hadronic width of the Z^0, to which they normalized their result for Γ_b, of 1742 ± 19 MeV[35] is used to yield $0.221\pm0.004\pm0.012$ (where the 19 MeV error on the total hadronic width was removed in quadrature). The value of $F_b \cdot Br(B \to lX)$ is then extracted using the same value of $Br(B \to lX)$ that was used by each experiment to calculate F_b. The $F_b \cdot Br(B \to lX)$ measurements are given in Table 1–5.

Experiment	$F_b \cdot Br(B \to lX)$
Mark II (e & μ)	$0.025^{+0.011+0.006}_{-0.088-0.005}$
ALEPH (e & μ)	$0.0224\pm0.0016\pm0.0010$
L3 (e & μ)	$0.0259\pm0.0005\pm0.0007$
OPAL (μ)	$0.0226\pm0.0007\pm0.0013$
Weighted Average	$0.0248\pm0.0004\pm0.0005$

Table 1–5 The SLC and LEP measurements of the product of the hadronic branching fraction to b quarks and the branching ratio of the B hadron to leptons.

To determine an average value for F_b, the common systematics among the lepton tags of the B decay semileptonic branching ratio must be properly handled. As mentioned previously, the lepton tags actually measure the product of F_b and the branching fraction of the B hadron to leptons, $F_b \cdot Br(B \to lX)$, so in order to combine the lepton tag results, the weighted average of the product will be taken and then converted to F_b afterward. The resulting average value is given in Table 1–5.

To determine a value for F_b, a value of $Br(B \to lX)$ must be chosen. There is some question of what value of $Br(B \to lX)$ to use. ALEPH, for instance, has used the value from CLEO and ARGUS measurements at the $\Upsilon(4s)$,[36] where only $B_{u,d}$ mesons are studied, whereas the Mark II and L3 use values measured at higher energies. There appears to be a significant difference between these results, the former being 0.102±0.007 and the latter being 0.117±0.006. The branching ratios measured at PEP, PETRA and LEP are used for calculating the following average value of F_b because the mixture of various B hadron species at these energies more properly represents that at the Z^0. This results in an average of

$$F_b(\text{lepton tags}) = 0.212 \pm 0.003 \pm 0.012$$

where the error includes the uncertainty in $Br(B \to lX)$. Averaging this with the DELPHI result yields,

$$F_b(\text{world average}) = 0.212 \pm 0.003 \pm 0.011.$$

The Standard Model predicts a value of $F_b = 0.217$.[13] Despite the contribution from the DELPHI measurement, the systematic uncertainty in this value is dominated by the uncertainty in $Br(B \to lX)$, which suggests that other measurements not depending on tagged leptons — such as the impact parameter significance tag — would be beneficial.

1.6 Measuring the Non-leading Multiplicity in b Quark Events

The high $b\bar{b}$-purity sample of impact parameter tagged events can also be used to measure other properties of $b\bar{b}$ events. The average charged multiplicity of $Z^0 \to b\bar{b}$ events, $\bar{n}_b$, is pursued in this analysis.

1.6.1 Theoretical Interest

The primary purpose of this measurement is a qualitative check of QCD phenomenology as observed in the fragmentation process. The framework of QCD provides that, at high energy, multiple particle production is governed by gluon fragmentation, which is triggered by the disruption of the vacuum by the color charge of the leading quark. As such, the fragmentation process is expected to be independent of the initial quark flavor. It has been suggested[37][38] how this expectation can be tested by measuring $\bar{n}_b$, subtracting off the well-known average B meson decay multiplicity, $\bar{n}_B$, and determine the *non-leading* multiplicity,

$$\bar{n}_{nl} = \bar{n}_b - \bar{n}_B. \tag{1-16}$$

The non-leading multiplicity can then be compared to the total multiplicity of e^+e^- annihilation at the center of mass energy equal to the average energy available to the non-leading system in $Z^0 \to b\bar{b}$ events. This is shown graphically in Figure 1–12(a). This average non-leading energy can be expressed as

$$\langle E_{nl} \rangle = E_{cm}(1 - \langle x_E \rangle) \tag{1-17}$$

where E_{cm} is the center-of-mass energy and $\langle x_E \rangle$ is the average energy fraction carried off by the heavy hadron,

$$x_E = \frac{2E_{had}}{E_{cm}}. \tag{1-18}$$

Conversely, as shown in Figure 1–12(b), it was also suggested that one can determine $\langle x_E \rangle$ by a measurement of $\bar{n}_{nl}$ by assuming that the multiplicity of the non-leading system is indeed independent of the flavor of the initial quark flavor.

1.6.2 Previous Measurements

The measurement of $\bar{n}_b$ ($\bar{n}_c$), in the case of $e^+e^- \to \gamma^* \to b\bar{b}$ ($c\bar{c}$) decays at PEP and PETRA energies, has been published by the Mark II,[37] DELCO,[39] TPC[40] and TASSO,[41] so a measurement at E_{cm} = 91 GeV is well motivated. Table 1–6 shows the measured values of $\bar{n}_b$. The Mark II and TPC analyses also make the comparison of the non-leading multiplicity to lower energy total multiplicity data, both finding that their $\bar{n}_{nl}$ is consistent with the total multiplicity measurements, within their experimental uncertainty. The Mark II and TASSO analyses also reverse the measurement to determine average fragmentation information. The Mark II measured $\langle x_E \rangle$ in the manner described above, while TASSO used the $\bar{n}_b$ distribution to determine $\langle z_b \rangle$ by a comparison with Monte Carlo predictions. Each

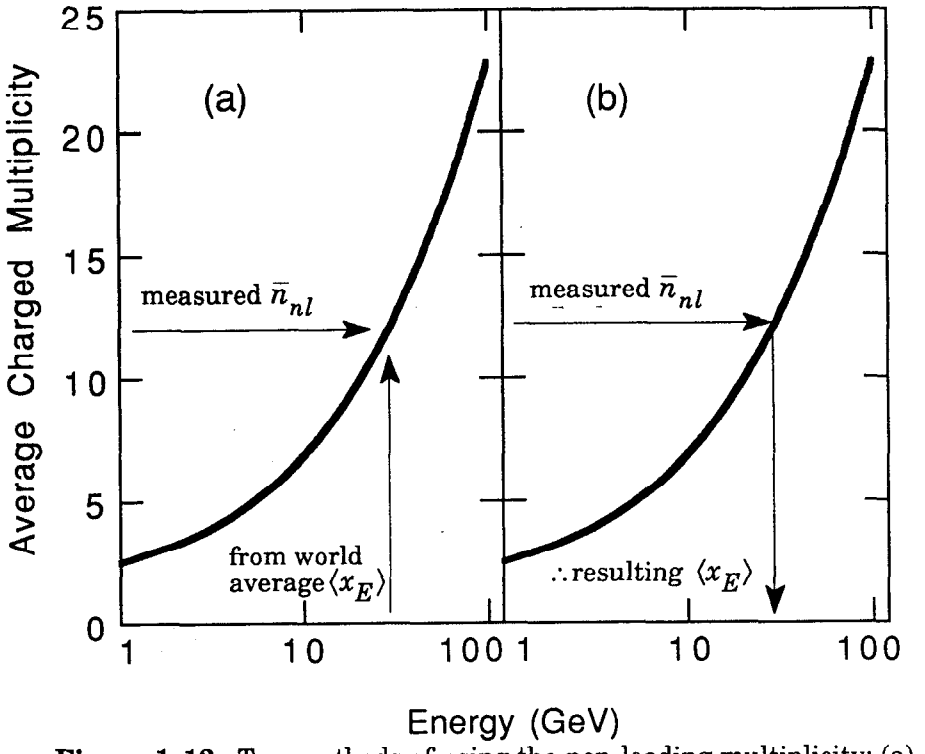

Figure 1-12 Two methods of using the non-leading multiplicity: (a) a test of the independence of the fragmentation process on the flavor of the initial quark by comparing a measured non-leading multiplicity, $\bar{n}_{nl}$, and its average non-leading energy to total multiplicity at lower E_{cm}; (b) the determination of $\langle x_E \rangle$ from the measured non-leading multiplicity by assuming the flavor independence. In both figures, the line represents the world's average measurement of the total charged multiplicity.

of the PEP and PETRA measured values of $\bar{n}_b$ can be used to make the comparison with the lower energy total multiplicity by use of an average decay multiplicity for the bottom or charm heavy hadron.

In making these comparisons a number of corrections were studied to make the comparison as relevant as possible. These corrections include:

- heavy quark correction, which removes the effects of heavy quarks in the lower energy total multiplicity data;
- leading particle correction, which removes the effect of the leading particles in light quark events;
- x_E-distribution correction, which accounts for the distribution of the non-leading energy and the non-linear relationship between multiplicity and energy.

experiment and heavy quark type	tagging method	E_{cm} (GeV)	$\bar{n}_b$ or $\bar{n}_c$
Mark II $(b\bar{b})$[37]	lepton tag	29	16.1±1.1
Mark II $(c\bar{c})$[37]	lepton tag	29	13.2±1.0
DELCO $(b\bar{b})$[39]	lepton tag	29	14.32±0.92
TPC $(b\bar{b})$[40]	lepton tag	29	16.7±1.0
TPC $(c\bar{c})$[40]	lepton tag	29	13.5±0.9
TASSO $(b\bar{b})$[41]	vertex tag	35	15.96±1.43
TASSO $(b\bar{b})$[41]	vertex tag	42.1	17.02±1.98

Table 1–6 The b or c event multiplicities $\bar{n}_b$ or $\bar{n}_c$ measured at PEP and PETRA are given with their total statistical and systematic error. Also given is the method used to select the subset enriched in b or c events. DELCO, TPC and TASSO measured the multiplicity in the thrust hemisphere opposite the tagged hemisphere, whereas Mark II used the entire event multiplicity.

It can be seen in Figure 1–13 that the overall agreement between the non-leading multiplicity measurements and lower energy multiplicity is indeed good and a similar point at E_{cm} = 91 GeV would be advantageous in demonstrating further agreement. These corrections, and the comparison with them appropriately applied, are discussed in all their detail in Section 7.6, "Comparison with Data at Lower C.M. Energy," on page 217.

The measurement which is performed in this analysis has a number of advantages over earlier measurements. Firstly, by measuring the non-leading multiplicity at a significantly higher center-of-mass energy than earlier experiments, the corresponding non-leading energy (~30 GeV) is on the continuum, well away from any resonances, and is in a region where the total multiplicity has been accurately measured by many of the PEP and PETRA experiments. Also, the use of the impact parameter tag avoids systematic difficulties of the high p and p_T lepton tags alluded to by J. Chrin.[42] Finally, the measurement of $\langle x_E \rangle_b$ in this fashion is an important independent check on $\langle x_E \rangle_b$ measured using the lepton momentum spectrum from semileptonic B decay.

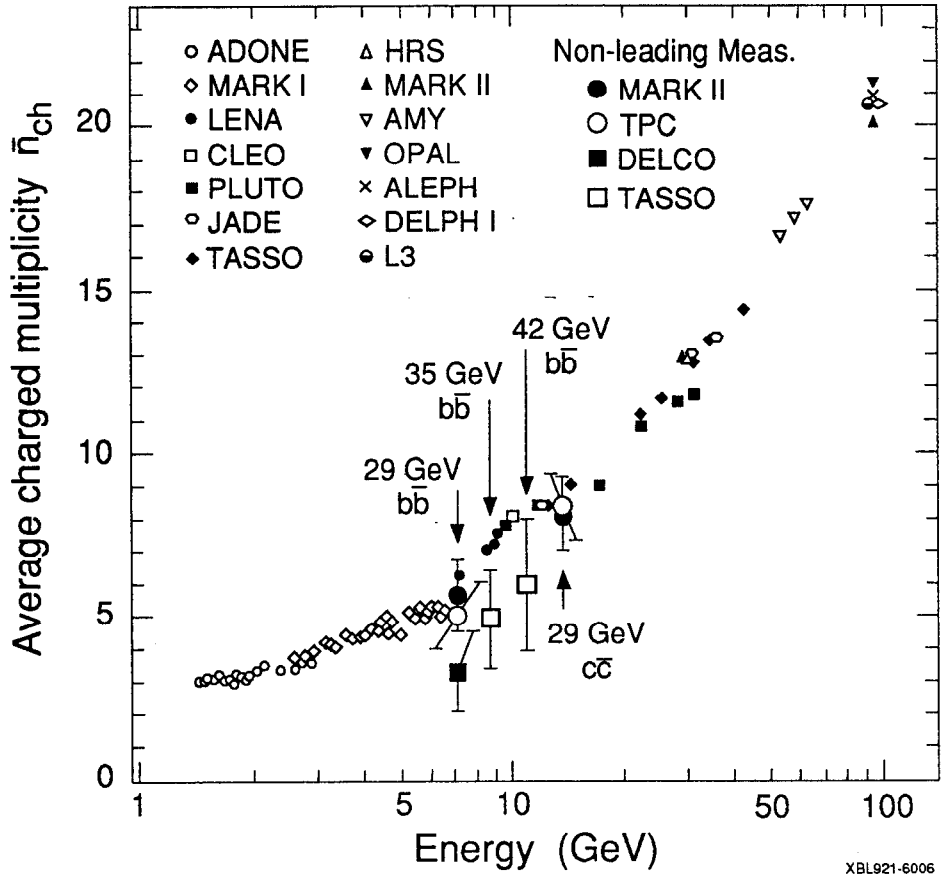

Figure 1–13 The comparison between the non-leading multiplicity at the corresponding non-leading energy, and the total multiplicity at a given center of mass energy. The center of mass energies at which the non-leading multiplicities were measured are indicated. The non-leading energy for a measurement of the *b* event multiplicity at a center-of-mass energy of 91 GeV is about 30 GeV.

Chapter 2

Experimental Apparatus

The heart of the Stanford Linear Accelerator Center (SLAC) is the linear accelerator (LINAC) which accelerates electrons up to very high energies.[44] Constructed between 1962 and 1966, the LINAC originally provided electrons for a very productive fixed target experimental program. This program included the deep inelastic scattering experiments which demonstrated the quark nature of the proton and neutron.[45] In the early 1970's SLAC built its first electron-positron storage ring, SPEAR, where the charm quark[46] and tau lepton[47] were discovered. In the late 1970's the PEP storage ring was built to collide electrons and positrons at still higher energies. Finally in the mid-1980's the SLAC Linear Collider (SLC) was constructed to provide electron-positron collisions at high enough energies to produce the weak boson, the Z^0. To detect the produced particles, we use the Mark II detector, which was originally used at SPEAR and PEP. It was extensively upgraded at PEP in preparation for its move to the SLC and upgraded still further at the SLC.

2.1 The SLAC Linear Collider

The SLC is unique among electron-positron colliders now in use, in that it is a single pass collider, not a storage ring.[48] An important motivation behind the concept of a linear collider is an economic one. The cost associated with electron circular accelerators varies as the square of the energy of the machine, whereas a

linear accelerator's costs varies linearly with the energy.* Thus the linear collider concept is the only one which will be financially reasonable for the next generation of high energy electron-positron colliders and the SLC is a prototype for the study of linear colliders.

The SLC uses the LINAC to accelerate both the e^- and e^+ beams up to an energy of 47 GeV. At the end of the linac the beams are sent into opposite arcs which bend them around in order to collide them together head-on (see Figure 2–1). Three bunches of particles are accelerated simultaneously, two e^- bunches and one e^+ bunch. The purpose of the second e^- bunch is for producing the e^+ bunch for the next accelerator cycle. At two-thirds of the way down the accelerator, this extra e^- bunch is deflected out of the accelerating tube and directed onto a tungsten target. Here the ensuing electromagnetic shower produces the positrons which will be sent to the beginning of the LINAC and accelerated along with two new e^- bunches.

In order to maximize the luminosity of the accelerator, and thus the production of Z^0s, it is essential that the beams be compressed to a very small transverse size when they collide at the interaction point (IP). To achieve this it is essential that the beams be very well tuned coming from the LINAC. Damping rings, near the beginning of the LINAC, reduce the transverse emittance of the beams through synchrotron radiation. Just before the beams reach the IP, the Final Focus system compresses the transverse size of the beams from about 1 mm to only a few microns. After the collision, the beams go out through the opposite final focus where they are diverted toward beam dumps.

The SLC produced it's first recorded Z^0 on 11 April 1989. In the remainder of that year, the Mark II detector recorded 528 events. In the fall of 1989 the SLC was shut down for upgrades both to the accelerator and the Mark II detector, which included the installation of the vertex detectors. The SLC began running in 1990 with a test run during January in which 37 Z^0 events were produced and then ran through the summer to produce 257 more events. As the analysis in this thesis requires the precision tracking provided by the vertex detectors, only the 294 events

* These cost scaling rules can be illustrated with the following argument. In a storage ring design, the majority of the cost scales as the size of the ring. However, the RF power required to compensate for the sychrotron radiation scales differently. The energy loss per orbit due to synchrotron radiation is proportional to E^4/R, where E is the machine energy and R is its radius. Thus the cost will be a sum of two terms: costs which scale linearly with the size of the ring (magnets, excavation, *etc.*) and those due to the RF system. The total cost, C, can be expressed as $C = \alpha R + \beta E^4/R$. Differentiating this with respect to R and setting the derivative to zero to optimize the cost performance yields the result that the cost of a storage ring scales as E^2. In contrast the cost of a linear machine scales linearly with energy. More detailed information can be found in Reference [49]

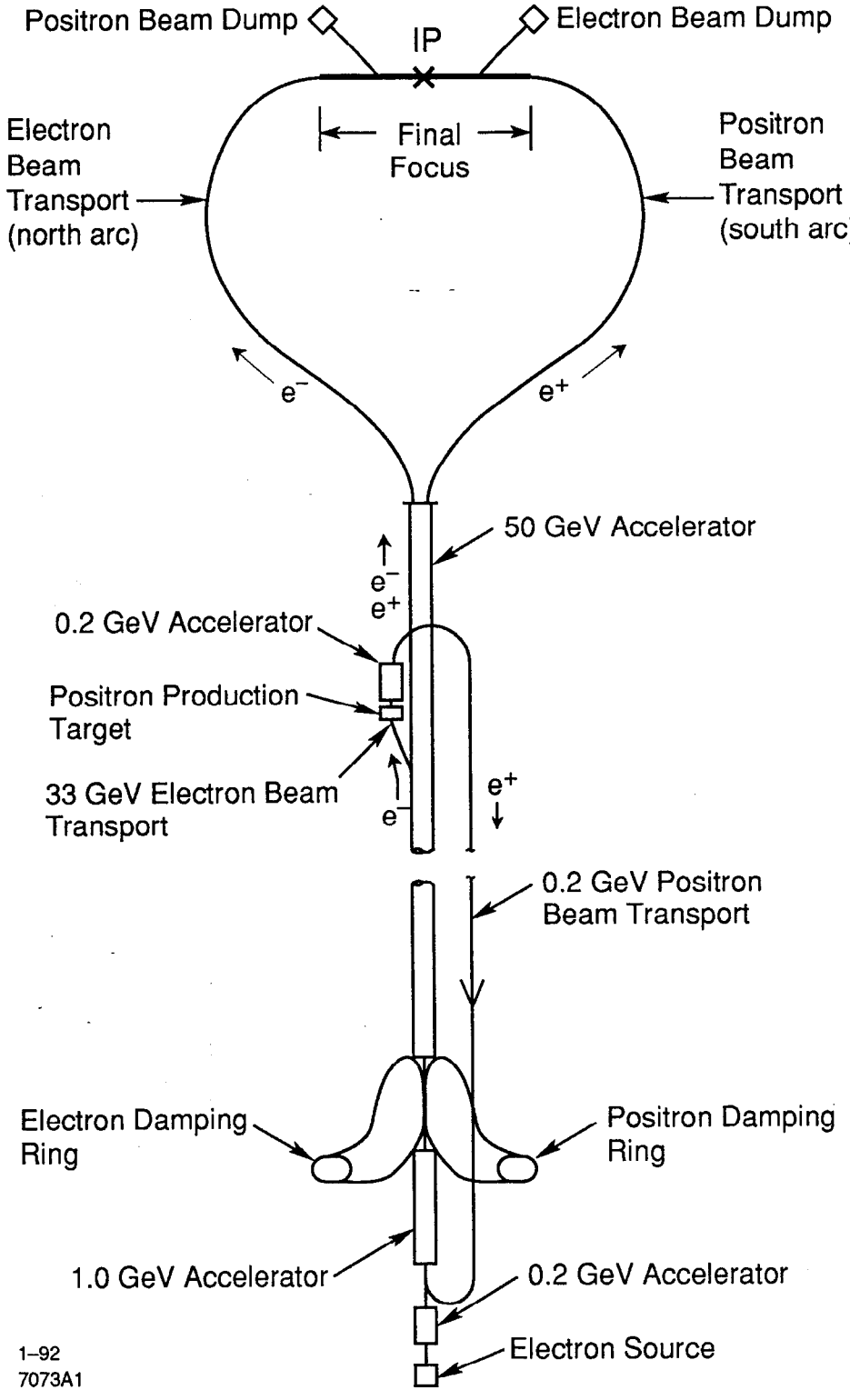

Figure 2–1 A schematic layout of the SLC.

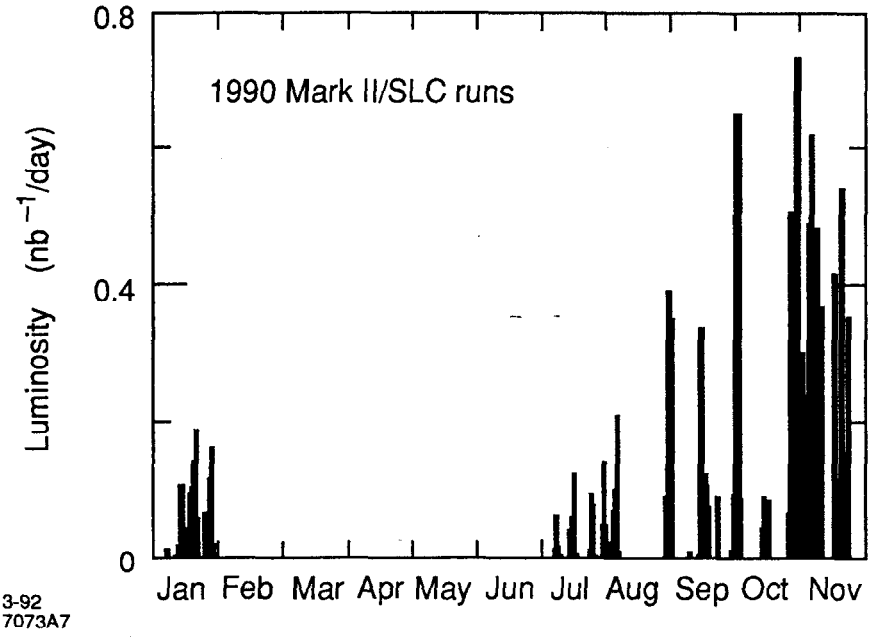

Figure 2–2 The daily luminosity delivered to the Mark II by the SLC during the 1990 runs.

taken during the 1990 runs are used here. The average center of mass energy for the 1990 runs was measured to be 90.93±0.01±0.04 GeV.[50] The luminosity recorded by the Mark II during 1990 is shown in Figure 2–2. From July through October, the focus of the run was on SLC machine physics studies, particularly improvement of performance parameters such as the repetition rate and raising the beam currents. With these improvements, instantaneous luminosity as high as 3 to 4 Z^0 events per hour was achieved.

2.2 The Mark II Detector

The Mark II is a solenoidal spectrometer which was based on the first e^+e^- detector at SLAC, the Mark I. The detector was first used at SPEAR from 1978 to 1979, and later at PEP from 1981 to 1984. In preparation for its move to the SLC, the detector was substantially upgraded with the additional of several new detector components, most notably a new central tracking detector. The upgraded detector was tested at PEP with a run during 1985 and 1986. The Mark II was moved to the SLC collider hall in 1986 and started operations there in 1987. Finally, in the fall of 1989, the vertex detectors were installed for the final Mark II runs during 1990.

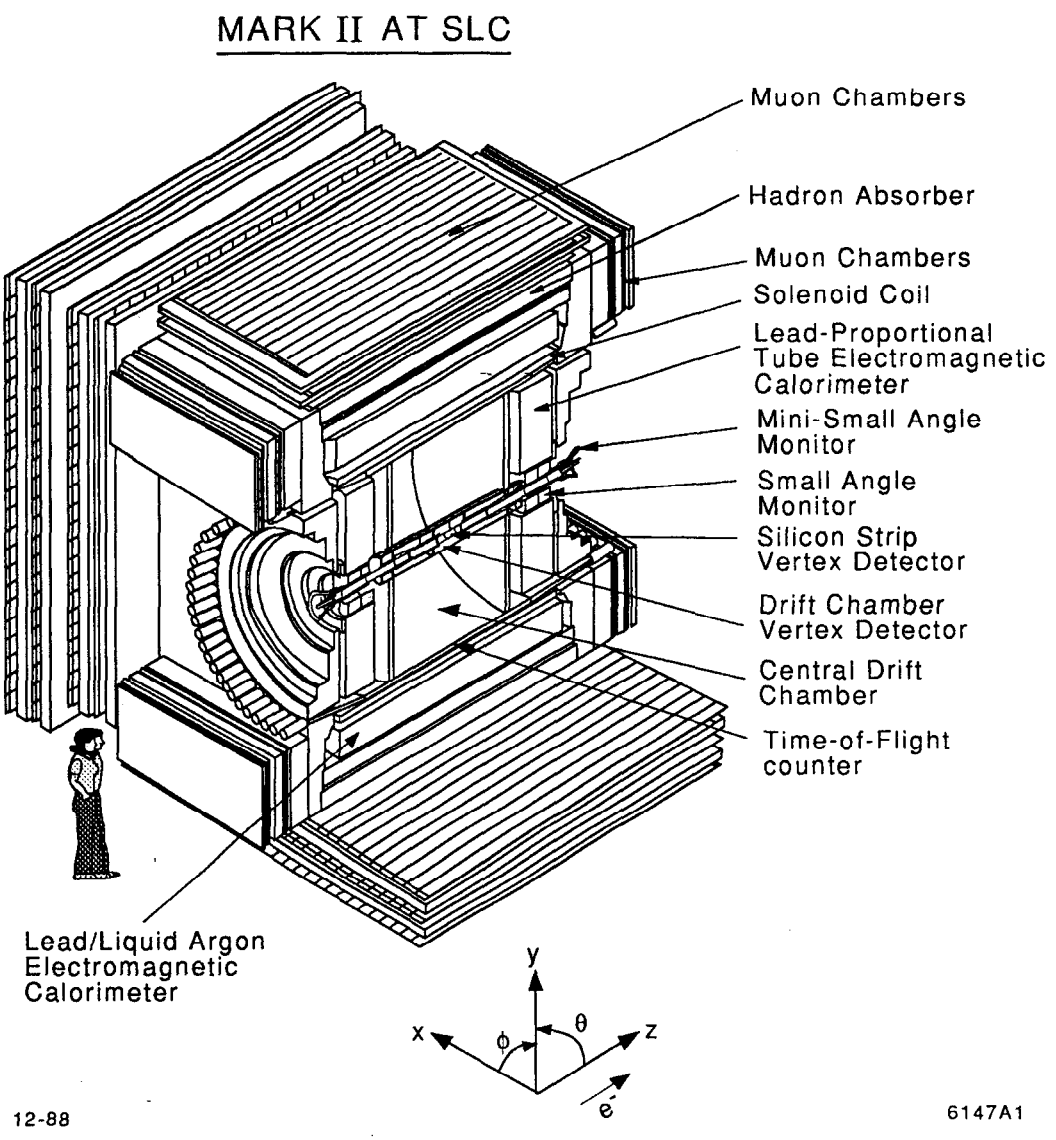

Figure 2–3 A cut-away view of the Mark II detector systems in place for the 1990 runs at the SLC with the definition of the Mark II coordinate system.

2.2.1 Detector Overview

As shown in Figure 2–3, the Mark II has a series of detecting layers which surround a central beam pipe that brings the e^- and e^+ beams into the IP located at the center of the detector. From the IP, particles whose trajectories are not at small angles with respect to the beam pipe will go through the beam pipe, then into the detector systems. These are introduced roughly in the order a particle would pass through them. As the tracking detectors are the primary tool in this analysis, they are discussed in more detail, along with the event trigger, data acquisition and

energy measurement, in the following sections. Reference [51] contains an extensive description of the upgraded Mark II detector.

Beam Pipe

The beam pipe used by the Mark II during 1990 is an aluminum vacuum chamber with a copper coating on the inner surface. In order to get detectors as close as possible to the IP, the radius is only 25 mm.

Silicon Strip Vertex Detector

The Silicon Strip Vertex Detector (SSVD) is a three layer silicon strip detector located just outside of the beam pipe. The radii of the three detector layers are 29, 33 and 37 mm from the beam axis. The primary function of the SSVD is to provide a very accurate track measurement close to the IP in order to accurately measure the track impact parameter.

Drift Chamber Vertex Detector

The Drift Chamber Vertex Detector (DCVD) is a 38 layer drift chamber divided axially into 10 jet cells. The strengths of the DCVD are providing very accurate track position measurements, particularly for locating the correct hits for a given track in the SSVD and for rejecting spurious tracks detected by the outer detector.

Central Drift Chamber

The Central Drift Chamber (CDC) is a large 72 layer drift chamber, extending out to a radius of 1.52 m and having an active length of 2.3m. The initial track finding is done in the CDC, where closely spaced tracks have the greatest separation. Furthermore, its lever arm provides a very accurate angle measurement necessary for good impact parameter determination with high momentum tracks. By measuring the charge deposited on each of the layers in the CDC, it also provides a measurement of the energy loss by a given particle (dE/dx), which when combined with a momentum measurement can aid the identification of electrons.

Time-of-Flight System

The time-of-flight system (TOF) is used primarily for particle identification and detection of cosmic rays. It consists of 48 blocks of 4.5 cm thick plastic scintillator that extend axially for 3.0 m along the outside edge of the CDC. A phototube is placed at each end. The system's measured average time resolution is 220 psec. Combined with the dE/dx information from the CDC, a 2σ separation is possible between π and K up to a momentum of 10 GeV/c and between K and p up to 2 GeV/c.

Solenoidal Magnet Coil

The Mark II solenoid is a conventional coil which provides the nominal magnetic field of 4.75 kG. The thickness is 1.3 radiation lengths and the field uniformity is held to 3% in the tracking volume. The field has been mapped as a function of z and r with an error of <0.1% for use in the tracking fitting programs. The absolute scale of the field during data runs is measured with a pair of Hall probes positioned on the ends of the CDC which provide field-normalization to <0.1%.

Liquid Argon Electromagnetic Calorimeter

The primary calorimeter of the Mark II detector is a lead-liquid argon sampling calorimeter. It is comprised of eight modules arranged in an octagonal barrel outside of the solenoid magnet. Except for small gaps between the modules, it covers the polar angle range from 47 to 133 degrees, which corresponds to 64% of the total solid angle. Each module has a stack of 18 lead strips each of 2 mm thickness which are oriented in different directions to aid in assigning energy to a particular track. The total amount of material in the calorimeter is 14.1 radiation lengths for normal incidence. These strips are separated by 3 mm gap filled with liquid argon in which the ionized argon atoms drift in a 12 kV/cm electric field to the readout strips. The energy resolution has been measured at PEP to be $\sigma_E/E = [(3.3\%)^2 + (13.3\%)^2/E]^{1/2}$, where E is in GeV.

Endcap Calorimeter

The endcap calorimeter increases the solid angle coverage of the Mark II electromagnetic calorimetry by covering the region from 15 to 45 degrees from the beam axis. This system consists of a lead/proportional tube stack of 36 layers, for a total of 18 radiation lengths. In conjunction with the liquid argon calorimeter, 86% of the solid angle is covered with full electromagnetic calorimetry. During the Mark II upgrade run at PEP in 1985, the end-cap energy resolution was measured to be $\sim 22\%/\sqrt{E}$, where E is measured in GeV.

Muon Detector System

The Muon Detector System is comprised of four alternating layers of steel hadron absorbers and planes of proportional tubes. Some of these absorbers also serve as the flux return for the magnet. The solid angle coverage is 45% at the outermost layer. There are about 1.2 nuclear interaction lengths inside of the muon system and about 6 more in the muon system. The efficiency of the muon system is greater than 85% for muons in the fiducial volume of the detector with a momentum greater than ~1.8 GeV/c. The Muon Upgrade Detectors, which are located along the

faces of the detector above and below the beam pipe, add about 15% more solid angle coverage. There are 1.8 nuclear interaction lengths of lead before the first layer of proportional tubes and 1.2 nuclear interaction lengths of steel between that and the second layer of proportional tubes.

Luminosity Monitors

The Small-Angle Monitor (SAM) and Mini-Small-Angle Monitor (Mini-SAM) are designed primarily to precisely measure the integrated luminosity by counting small-angle Bhabha events. The SAM and Mini-SAM cover angular ranges of 50 to 160 mrad and 15 to 25 mrad, respectively. The SAM consists of nine layers of drift tubes for tracking and six layers of a lead/proportional tube sandwich which form a sampling calorimeter. The Mini-SAM is composed of six layers of plastic scintillator interspersed between a total of 15 radiation lengths of tungsten slabs.

2.2.2 The Central Drift Chamber

In upgrading the Mark II detector for operations at the SLC, a new drift chamber was constructed to replace the drift chamber used at SPEAR and at PEP prior to 1986. The new Central Drift Chamber (CDC)[51][52] was designed to provide large solid angle coverage, high momentum resolution in the solenoidal magnetic field, and good pattern recognition and track finding required in the narrow, high multiplicity jets at E_{cm} = 91 GeV.

There are a number of very good papers on the principles of drift chambers. For a general introduction to the concepts of drift chambers see any of those suggested in Reference [53]. A more detailed and especially informative article is the 1977 paper by F. Sauli.[54]

2.2.2.1 Design

The CDC is designed in a modified jet cell configuration in which there are 12 concentric layers of jet cells (superlayers), with each jet cell containing 6 sense wires (see Figure 2–4). Within a cell, the sense wires are spaced at 8.33 mm intervals and are staggered by ±380 μm from the centerline of the cell in order to aid pattern recognition by being able to determine locally through which side of the cell a particular track passed. Potential wires are placed between the sense wires so that the gain and drift field can be independently controlled. There are two guard wires on each end of the row of sense wires to provide a more uniform drift field in the center of the cell. The width of the cell at its center is 3.3 cm which was constrained by the desire to minimize the effect of diffusion and thus achieve the best double-track separation.

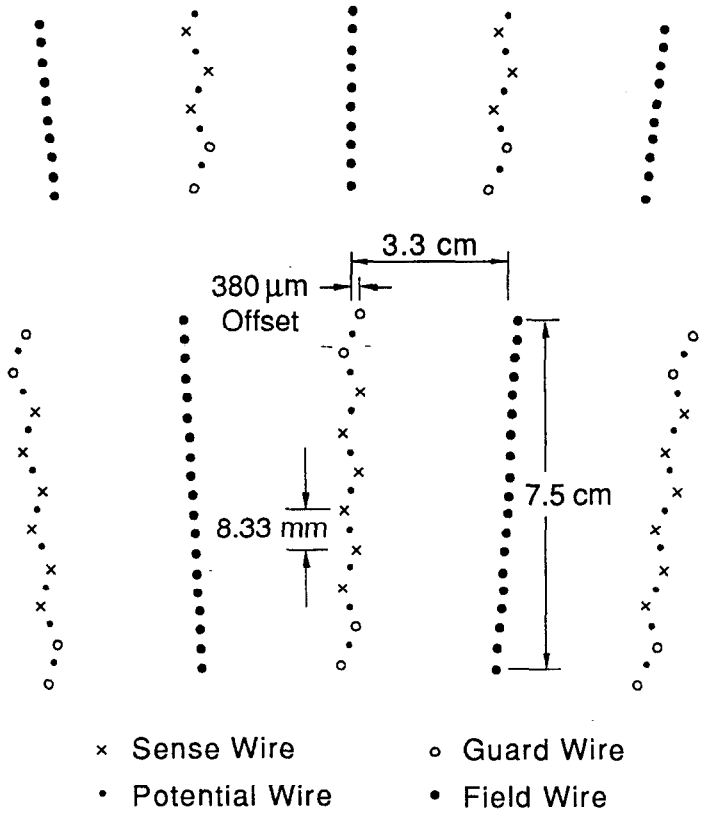

Figure 2–4 Wire pattern for a cell in the Central Drift Chamber.

The 12 superlayers consist of alternating layers of axial and stereo wires. The stereo layers are at ±3.8° angles with respect to the axis of the detector. Each superlayer has 10 more cells than the superlayer inside of it, ranging from 26 to 136 cells. As shown in Figure 2–5, this results in the cells being staggered with respect to each other, ensuring that a track will never pass through the entire detector into regions where the resolution could be degraded (for instance near the wire planes). The minimum distance between superlayers is 2.5 cm, including the effect of the stereo layers being at a smaller radius in the center of the chamber. The active length of the chamber is 2.30 m and it extends radially from 0.192 m to 1.519 m.

The mechanical design of the CDC consists of two aluminum endplates held apart by a 2 mm thick beryllium inner core and a 12.5 mm thick outer shell. Each row of wires within a cell are positioned with Delrin feedthroughs which are located on the endplate by pinning to three precisely machined holes. The accuracy of the wire positioning is expected to be ±35 μm. The contributions to this value are the

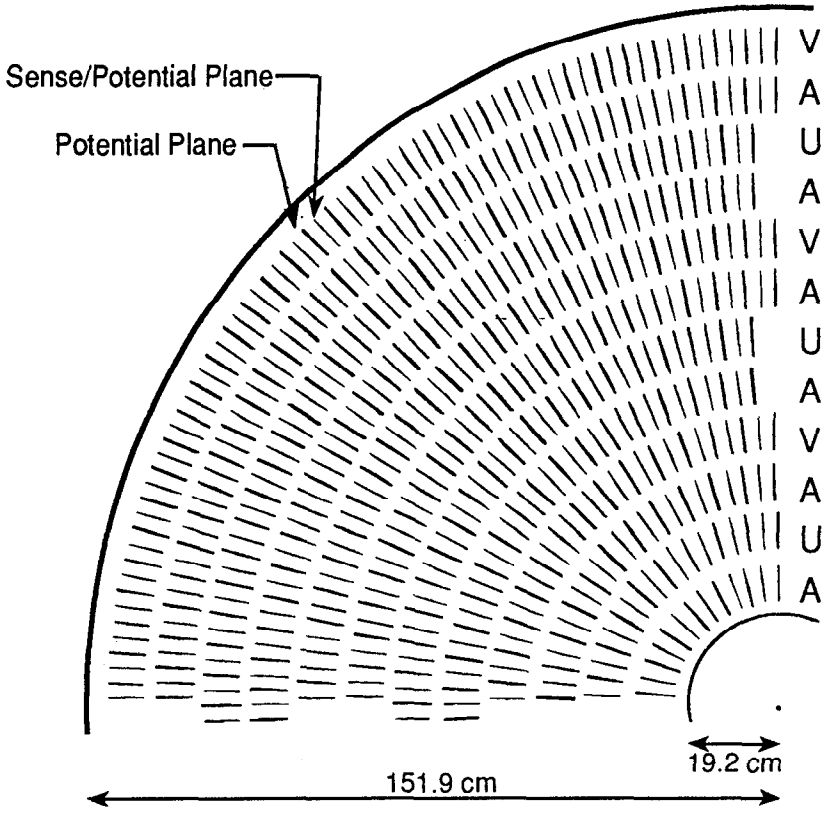

Figure 2–5 The layout of cells in the CDC. The letters indicate axial layers (A) and stereo layers at ±3.8° (U and V). Each layer has 10 more cells than the layer inside of it. Figure 2–4 shows the detailed wire pattern of each cell.

machining and placement of the endplates (25 μm), feedthrough machining and placement (15 μm), and wire sag and electrostatic deflection (10 μm).

2.2.2.2 Electronics

A schematic diagram of the CDC electronics is shown in Figure 2–6. The first stage is the preamplifiers, which are based on a Plessey SL560C chip, and is mounted on the endplates of the detector. The preamplifier gain is 25. The postamplifiers provide an additional gain of 100, pulse shaping, and two output signals: a discriminated timing signal and a pulse-shape signal.[55] The drift times are digitized by LeCroy 1879 Time-to-Distance Converters (TDC's), which are located in FASTBUS crates. They have achieved time resolutions of less than 1 ns. This timing signal is also used in the trigger, which is described later. The analog pulse height signals are digitalized using 100-MHz, 6-bit Flash Analog-to-Digital Converters (FADC's) based on the TRW 1029J7C chip and which are housed on SLAC-built FASTBUS boards.[57] The readout from the TDC's and the FADC's to

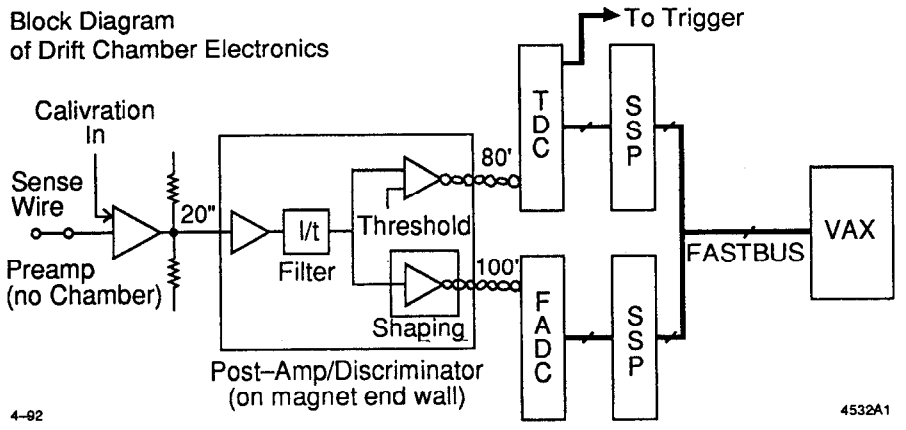

Figure 2–6 Schematic diagram of the CDC electronics.

the VAX 8600 host computer is controlled by programmable FASTBUS modules, the SLAC Scanner Processors (SSP's).[55]

2.2.2.3 Operation

The high voltage system provides graded voltages to the field wires through a resistor-divider chain, in which the center wire typically has about –4.5 kV, the potential wires are at -1.5 kV, the guard wires at -0.2 kV and the sense wires at ground. The copper skins which line inner and outer cylinders are typically at –2.5kV.

The chamber gas is composed of 89% Argon (Ar), 10% carbon-dioxide (CO_2) and 1% methane (CH_4), a mixture which is often referred to as "HRS gas". The pressure is just slightly higher than atmospheric pressure, which results in a gain of 2×10^4. The drift field with the above voltages is 900 V/cm. This corresponds to a drift velocity which is saturated at about 52 μm/ns.*

2.2.2.4 Track Finding

The first step of the track finding algorithm[59] is to group the individual position measurements, or hits, within each cell into track segments which are required to have at least three of the six possible hits. These segments are then combined into tracks first by using only the axial track segments and then adding the stereo information later. Pairs of the axial segments are then combined using a $\chi 2$ test requiring that they be consistent with belonging to a single track, with an arbitration algorithm to assign clusters to closely spaced tracks in a manner to

* This gas mixture has a saturated drift velocity at rather low fields beyond E/p of about 300 V/cm/atm (see Reference [56]).

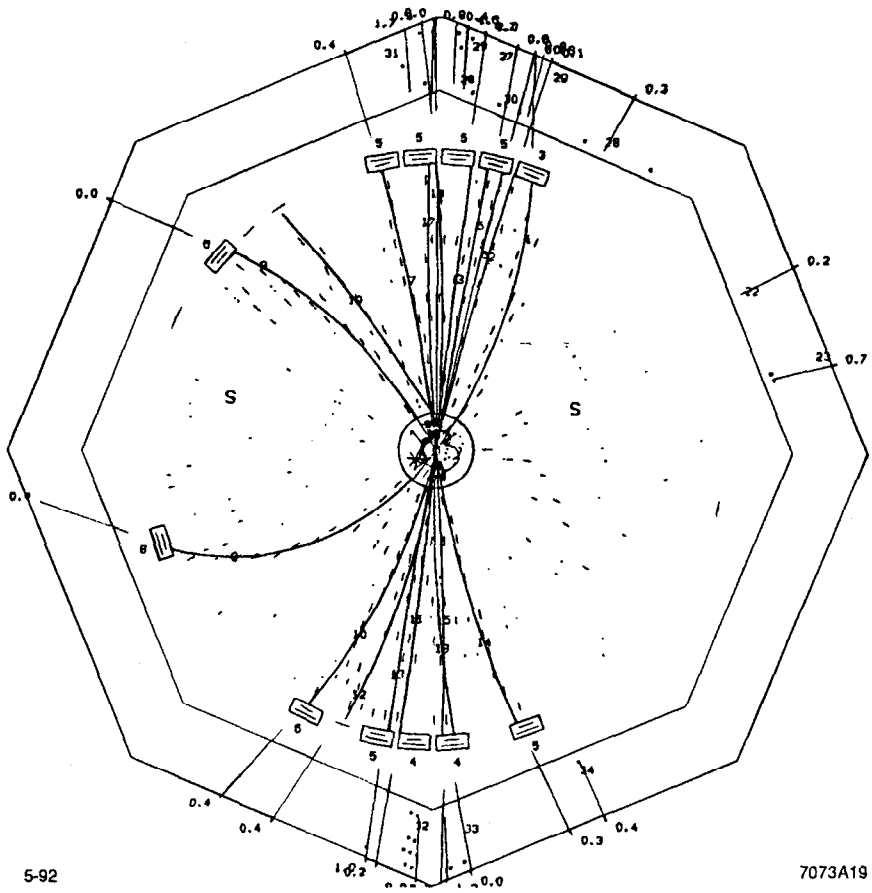

Figure 2–7 A typical event as recorded by the CDC. Also shown are the time-of-flight hits and the tracks detected in the liquid argon calorimeter.

minimize the overall χ^2. To add the stereo information, if a track has two or more stereo segments which can be unambiguously associated with that track, a χ^2 test is used to join the rest of the stereo segments. The remainder of the stereo segments are assigned to a track by using a smaller error for the stereo segments. Segments which are assigned to more than one track are arbitrated to only one of the tracks. Finally, the hits belonging to these tracks are then passed to a track fitting routine. Figure 2–7 shows a typical hadronic event with the fitted tracks.

The track fitting routine SARCS6[60] is based on a least-squares fit which determines the track trajectories in terms of five track parameters:

1. the tangent of the dip angle of the track from the beam axis, $s = \tan\lambda$, where $\lambda = \frac{\pi}{2} - \theta$,
2. the curvature of the track, $\kappa = 1/p\cos\lambda = 1/p_{xy}$ (where p is the track momentum),

3. the angle of the track projection in the xy plane at the track's point of closest approach to the origin, φ_0,
4. the radial distance to the point of closest approach of the track to the origin, δ_{xy}, and
5. the distance parallel to the z-axis to the point of closest approach of the track to the origin, δ_z.

The track fit also calculates the 5×5 error matrix relating these five track variables, accounting for a number of factors such as non-uniformity of the magnetic field, energy loss and multiple scattering. The multiple scattering inside the chamber is taken into account using the approximate formulas calculated by R. Gluckstern.[61] The use of these formulas to handle multiple scattering saves a vast amount of processing time by reducing the size of the matrix to be inverted in the track fit. Ordinarily, including multiple scattering in the track fit would mean having to invert a 72×72 matrix, but with these approximate formulas the problem is reduced to a 5×5 matrix inversion.

2.2.2.5 Position Resolution and Efficiencies

The drift times for hits in the CDC are determined by the information from the TDC. Using the FADC information, a time-slewing correction can be added which compensates for variation in the timing signal as a function of the signal pulse height. A particularly useful quantity to study which uses all of the information in a cell is the difference of triplet residuals for the inner and outer three sense wires:

$$[(t_1+t_3-2t_2)-(t_4+t_6-2t_5)]/8,$$

where t_i is the drift time for one of the six sense wires in a drift cell. Due to the staggering of the sense wires, the resulting distribution has a double peak structure which contains information about the position resolution, the wire stagger and can be used to monitor the changes in the drift velocity (see Figure 2–8).

The position resolution can also be measured by comparing the individual hits with respect to the fit of the track to which they are assigned. This method includes various systematic effects which are not studied by the local residuals such as the relative positions of superlayers. Figure 2–9 shows the track resolution as a function of drift distance. With the time-slewing correction, the average position resolution is about 170 μm.

The FADC's are of particular assistance to the tracking performance for their ability to resolve closely spaced hits. Various scanning algorithms that utilize the pulse shape information have an 80% efficiency for separating hits which are

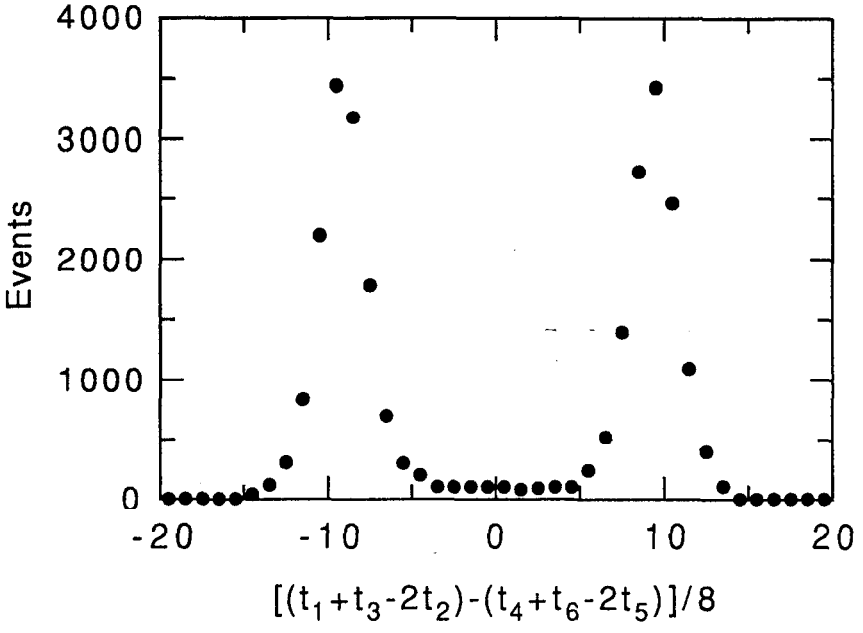

Figure 2-8 Double peaked distribution of drift times for the staggered wire in a CDC cell.[52]

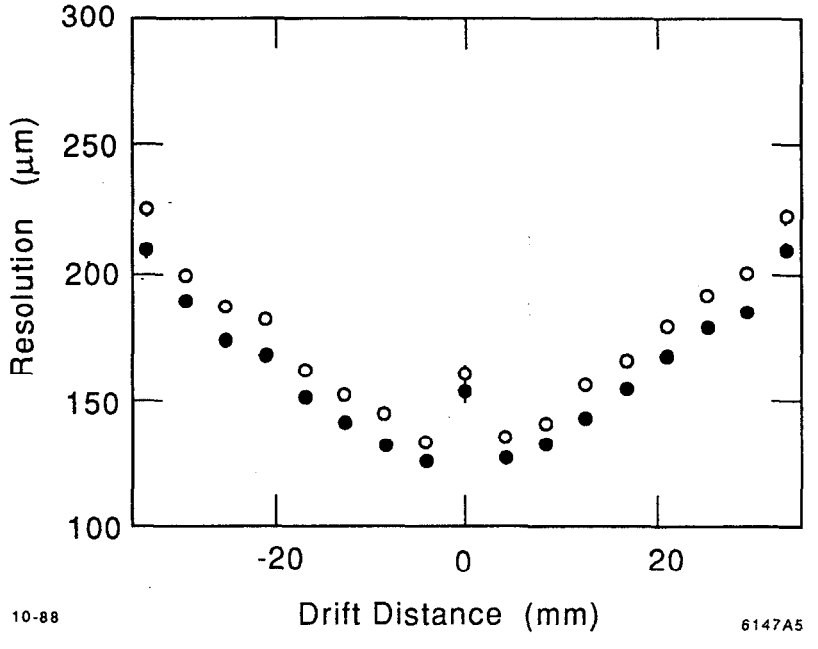

Figure 2-9 The CDC position resolution as a function of drift distance. The closed (open) circles are with (without) the FADC time-slewing correction.[51]

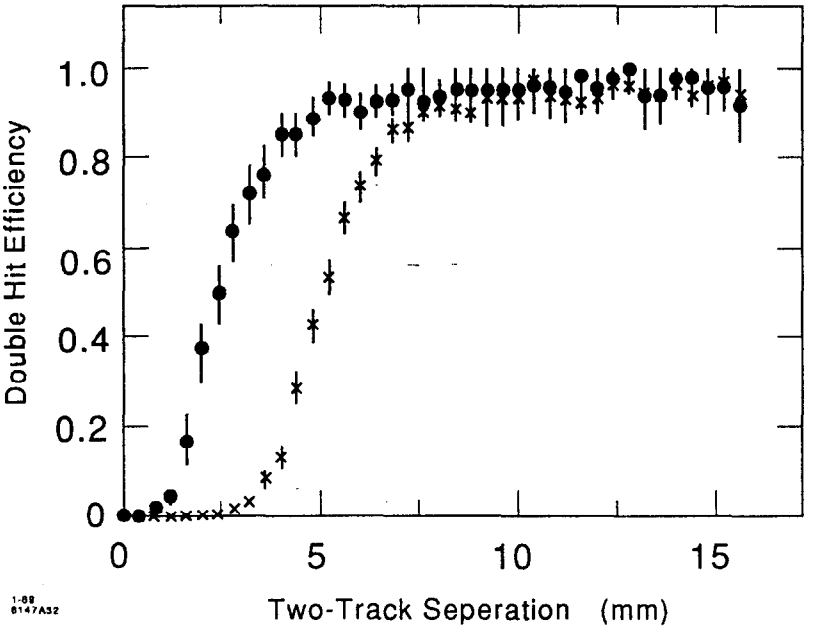

Figure 2–10 The double hit efficiency is plotted as a function of the separation of the two tracks using the TDC (×'s) and the FADC pulse height information (closed circles).[51]

3.8 mm apart, whereas with the TDC's alone, this is 6.4 mm. Figure 2–10 shows the double-hit efficiency as a function of the hit separation with and without the FADC information.

The CDC hit finding efficiencies have been studied and tuned in the Monte Carlo to reflect that which is observed in the data. In order to allow for efficiency correlations of the wires within a particular layer, the efficiencies are parameterized as single layer and superlayer efficiencies, which are shown in Figure 2–11 and Figure 2–12. The particularly lower efficiency in superlayer 12 is primarily due to high voltage problems in that layer which necessitated running at lower voltages at various times. The overall track finding efficiency has been measured in low multiplicity events at PEP to be approximately 99%. It is estimated that the track finding efficiency is greater than 95% for high multiplicity events at SLC energies. Figure 2–13 shows the distributions of the measured track finding efficiency for Bhabha events at PEP and Monte Carlo estimates of the efficiency in hadronic events at the SLC.[62] Below a $|\cos\theta|$ of 0.8 the efficiency is essentially flat with values which are essentially unity. The loss of efficiency at large values of $|\cos\theta|$ is well understood, as illustrated in Figure 2–14. The behavior and small p_{xy} is also well modelled by the Monte Carlo (see Figure 2–15). Nonetheless, to avoid these

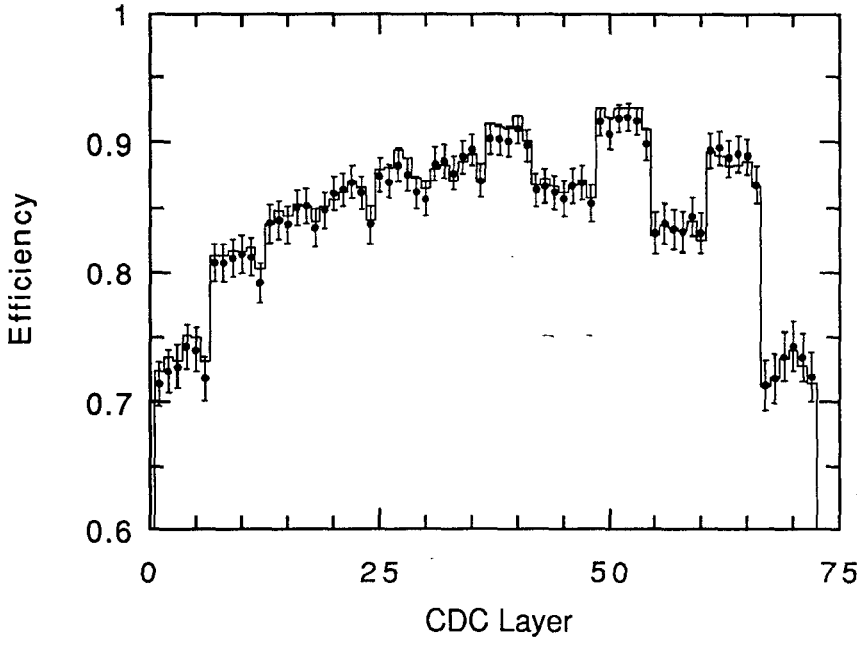

Figure 2–11 The single layer hit efficiencies in the CDC as measured in the 1990 hadronic data sample. The line is the Monte Carlo as tuned to the data.

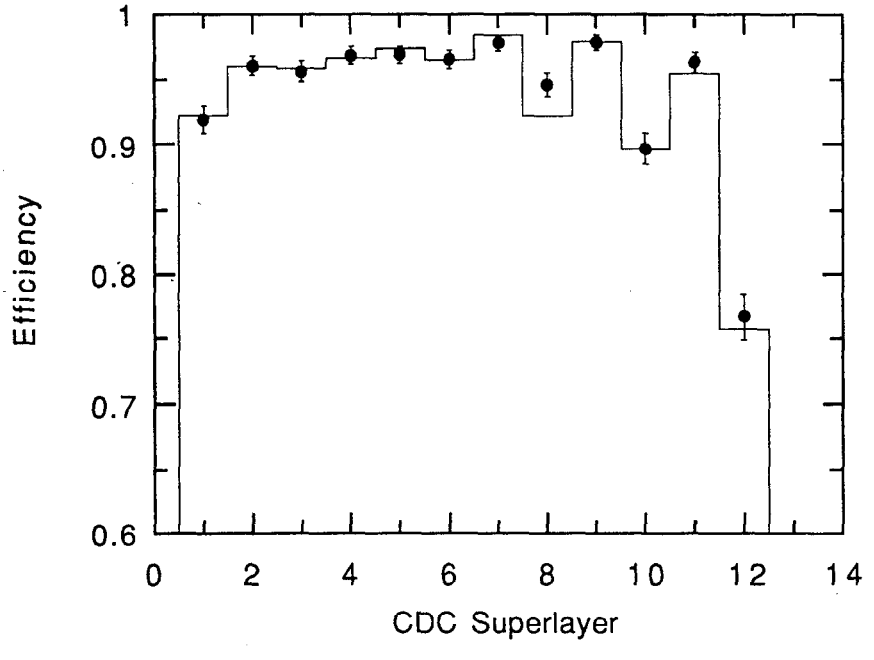

Figure 2–12 The superlayer efficiencies in the CDC as measured in the 1990 hadronic data sample. The line is the Monte Carlo which was tuned to the data.

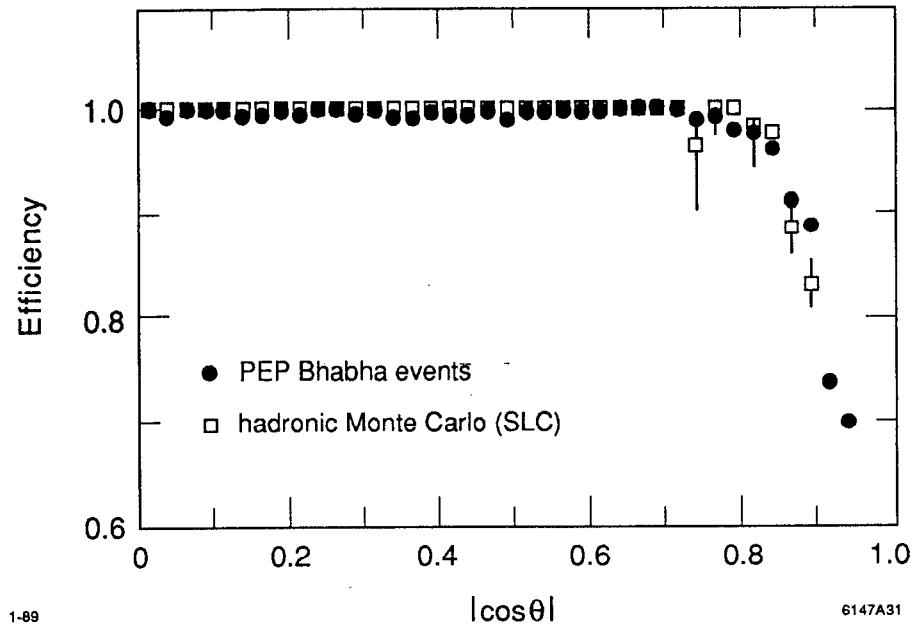

Figure 2–13 CDC track finding efficiency as a function of cos θ, as measured by Bhabha events detected with the Mark II Upgrade detector at PEP and as estimated using a hadronic Monte Carlo at SLC energies.

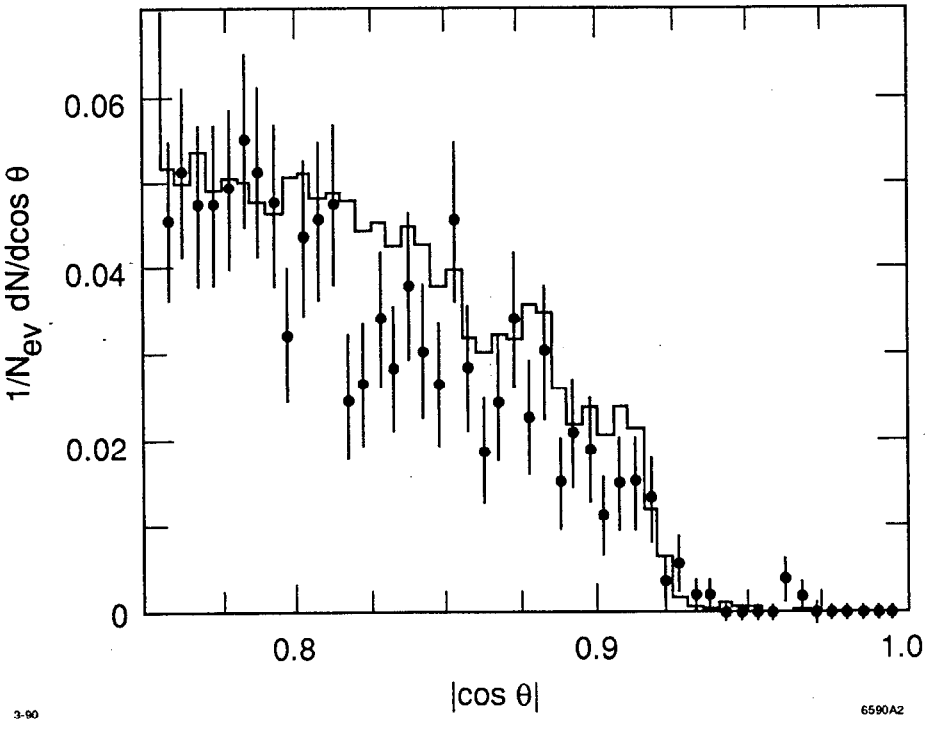

Figure 2–14 The distribution of tracks in the 1989 data set at large polar angles in the CDC.[62] The data is represented by points and the Monte Carlo by the line. The Monte Carlo is normalized to the number of events in the data.

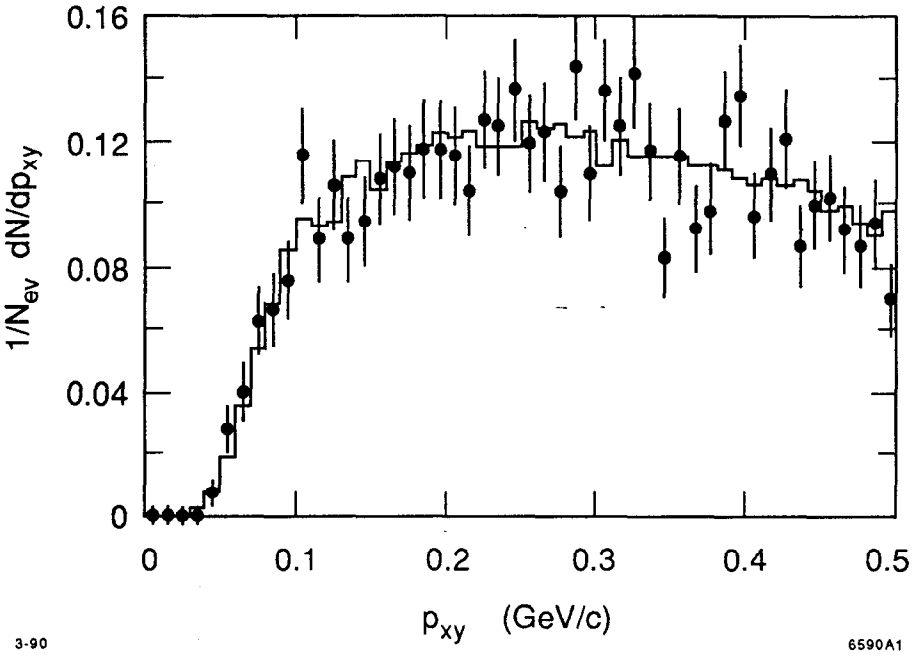

Figure 2–15 The distribution of tracks in the 1989 data set at small transverse momenta in the CDC.[62] The data is represented by points and the Monte Carlo by the line. The Monte Carlo is normalized to the number of events in the data.

regions of lower efficiency in the subsequent analyses, tracks are required to have $|\cos\theta| < 0.8$ and $p_{xy} < 0.15$ GeV/c. A data and Monte Carlo comparison of the distributions of the number hits per track is shown in Figure 2–16.

The large number of position measurements over a radial distance of about 1.3 m in the CDC provides an accurate measurement of the sagitta of a track in the axial magnetic field, and hence determination of the component of the momentum perpendicular to the beam axis. The momentum resolution was measured at PEP, and verified with muon events at the SLC, to be[63]

$$\frac{\sigma(p_{xy})}{p_{xy}} = \sqrt{(0.0046 p_{xy})^2 + (0.019)^2}\ , (p_{xy} \text{ in GeV/c})$$

where the first term is the intrinsic resolution and the second term is due to multiple scattering effects.

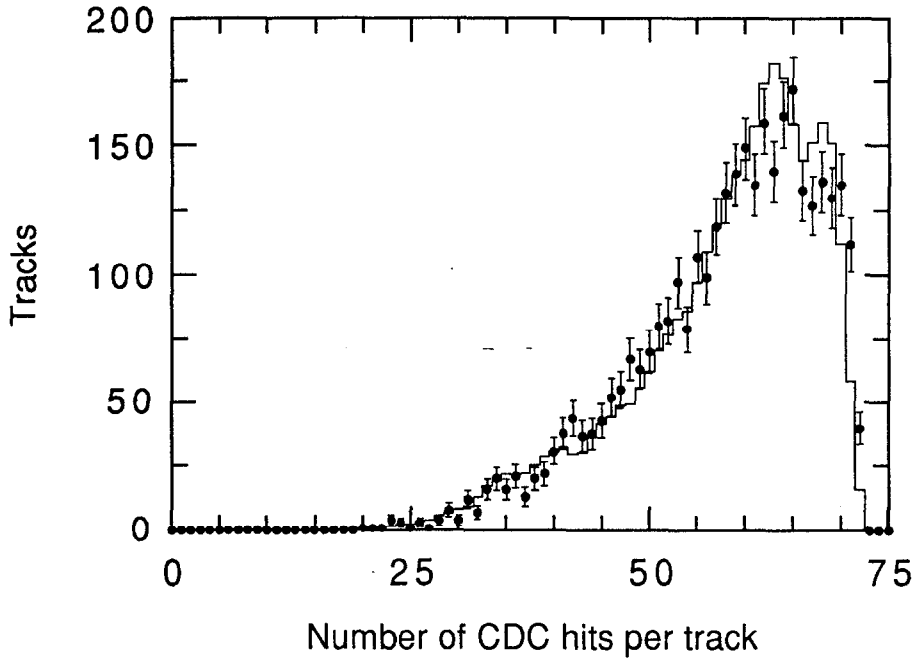

Figure 2–16 The distribution of the number of CDC hits per track for the data (points) and Monte Carlo (line). These tracks are required to have $|\cos\theta| < 0.8$ and $p_{xy} > 0.15$ GeV/c (refer to Figure 2–14 and Figure 2–15).

2.2.3 The Drift Chamber Vertex Detector

The Drift Chamber Vertex Detector (DCVD) is a high precision drift chamber designed to provide the high precision tracking necessary for the study of heavy quark decays at SLC energies. Of particular concern was that the detector be able to measure track trajectories with high resolution even in dense jets. In order to achieve the best possible resolution, it was necessary to control a wide spectrum of systematic effects, including the precision of the mechanical design and the physical environment inside the chamber such as the drift field, gas pressure and temperature. The development and initial studies of the DCVD are described in a number of references.[64][65][66]

2.2.3.1 Design

The layout of the DCVD is based on a jet cell geometry as illustrated in Figure 2–17. The active volume of the detector extends radially from 5.3 to 16.5 cm and has a total length of 48 cm. There are 10 jets cells in azimuth, each tilted at about 15° with respect to the radial direction from the chamber center, namely the beam axis. This feature resolves the ambiguity regarding which side of the cell a track passed, because the wrong tracks will be projected several centimeters away

from the beam axis. It is also useful to determine drift velocity by studying tracks which cross between cells and ensures that tracks from the interaction point are never entirely in a region near a wire plane where the chamber performance is degraded.

The cells contain 40 sense wires, spaced at 2.9 mm intervals, of which the central 38 are instrumented. The sense wires alternate with potential wires and there are grid planes at 1.8 mm from the sense plane on either side. Opposite the sense plane is the 59 wire cathode plane which is located between 1.44 and 5.08 cm from the sense plane at the innermost and outermost sense wires. A summary of the wire properties is given in Table 2–1.

To control the field quality near the inner and outer edges of the chamber, edge field wires with varying potential are used. All of the wires are parallel to the beam axis. Additionally, there are three types of field shaping electrodes used to grade the

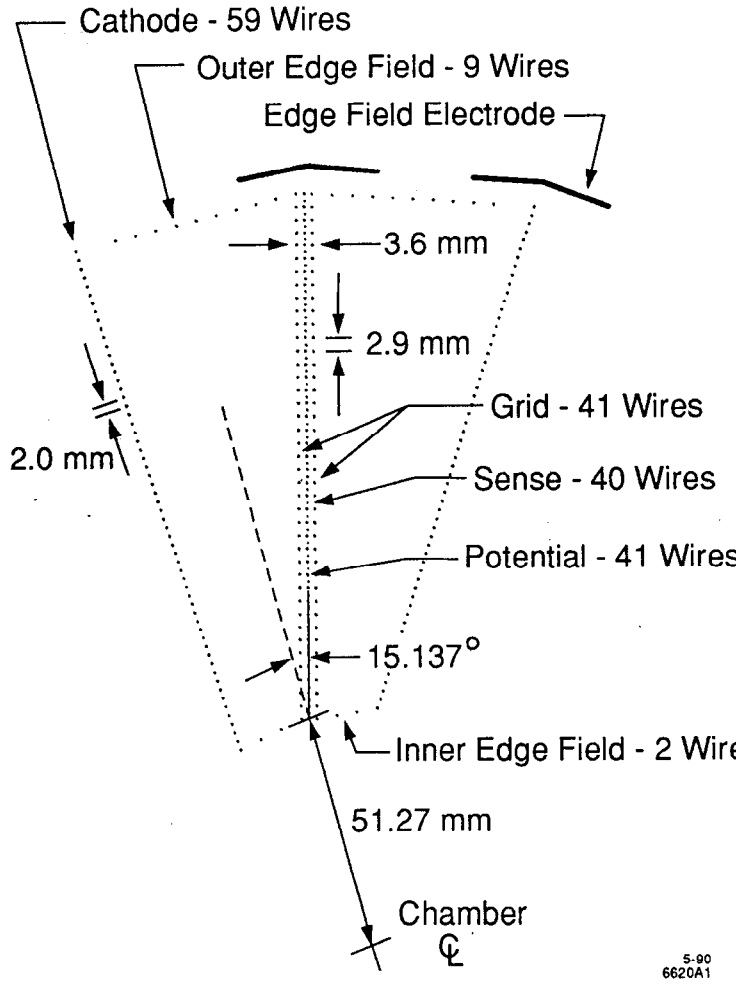

Figure 2–17 The DCVD jet cell design.

Wire Type	Number per plane	Diameter	Material
Sense	40	20 μm	tungsten
Potential	41	150 μm	Cu/Be
Grid	41	150 μm	Cu/Be
Cathode	59	225 μm	Cu/Be
Inner Edge Field	2	150 μm	Cu/Be
Outer Edge Field	9	150 μm	Cu/Be

Table 2–1 Wire characteristics for the various types of the wires in the DCVD. All of the wires are coated with a thin layer of gold.

field and improve its quality near the edges of the cell. There are conducting surfaces ("skins") bonded to kapton which is epoxied onto the inner and outer pressure cylinders. There are also twenty 'V' shaped edge field electrodes ("angel wings") between the wires and the outer skin. With the nominal operating voltages given in Table 2–2, this cell design produces drift fields which vary by <1% for all but a few of the wires near the cell edge.

System	Voltage (V)
Sense Wire	+2500
Potential Wire	0
Grid Wire	–480
Cathode Wire	–7900 to –2300
Outer Edge Field Wire	–6300 to –2300
Inner Edge Field Wire	-1500 & –440
Outer Skin	–6500
Inner Skin	–1600
Angel Wings (sense)	–1600
Angel Wings (cathode)	–6800

Table 2–2 Nominal operating voltages for 2 atm gas pressure. The angle wings by the sense and cathode planes are at different voltages.

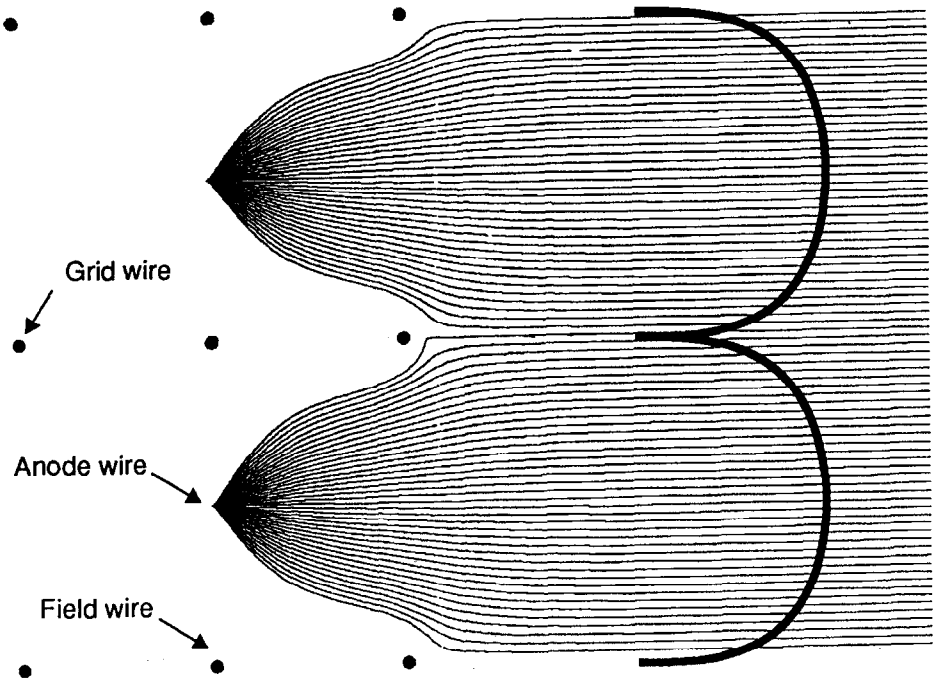

Figure 2–18 Electron drift trajectories in the region near the anode and grid planes. The heavy line is the line of constant drift time (isochrone).

Figure 2–18 shows the electron drift trajectories for a cell which employs a grid plane on either side of the sense plane. The primary advantage of the grid plane is the improved isochrony of the charge as a track traverses the region where charge will drift to the sense wire. It also aids in improving the electrostatic stability of the sense wire and in reducing cross-talk between adjacent channels.

To control the systematics which result from imperfections in the placement of the wires in the chamber, a novel approach was taken to positioning the wires. Instead of each wire position being individually determined by the location of a feedthrough on the end of the chamber, the planes of wires were attached as a unit to foundations made of Macor, a machinable ceramic with very good dielectric characteristics. In this fashion, the positions of the wires within a plane could be measured and their position within the chamber characterized by relatively few parameters. This modular design is illustrated in Figure 2–19. Each cell has two Macor foundations to hold the grid, cathode and edge field wires plus a much smaller stainless steel and Macor foundation to hold the anode wires. In the chamber, each of these are attached to an aluminum endplate held apart by 1.3 mm

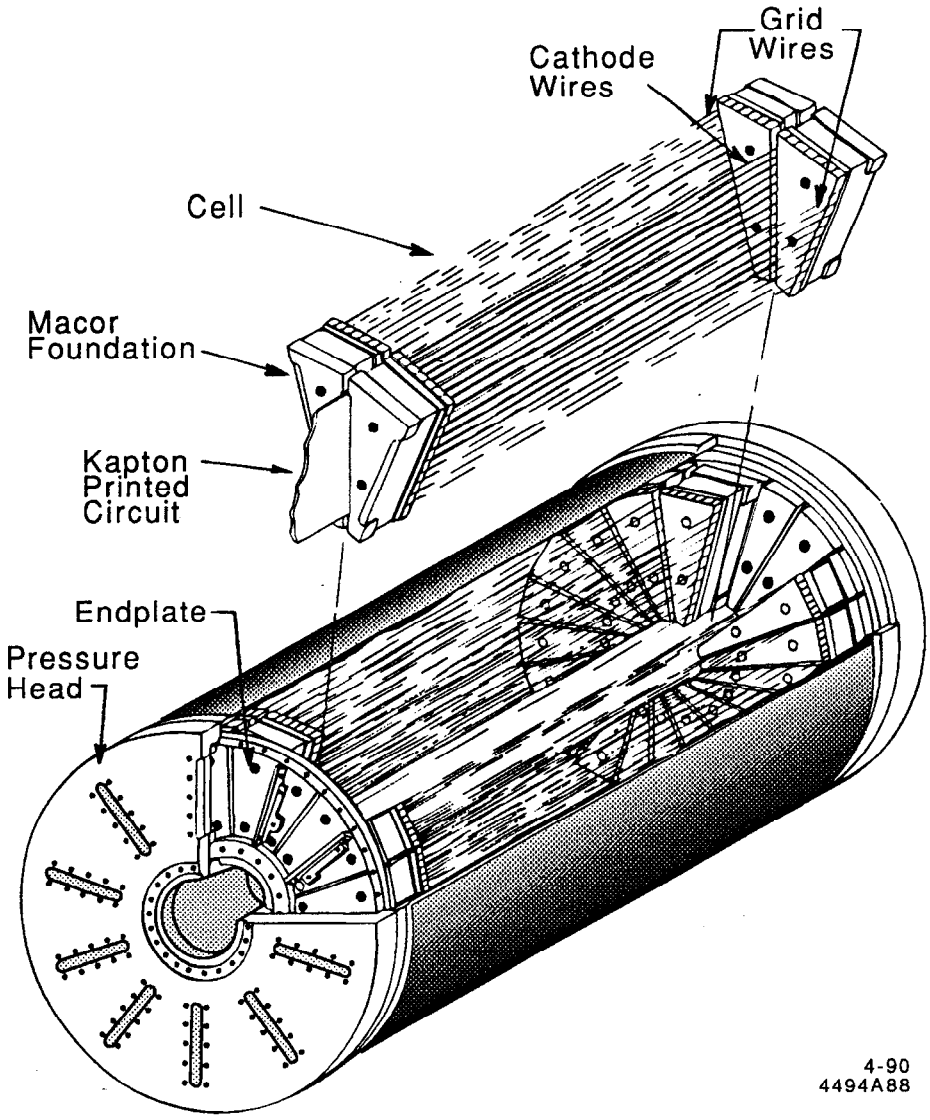

Figure 2–19 Mechanical assembly of the DCVD, illustrating the modular assembly of the cells on the Macor foundations.

thick beryllium inner and a 2.3 mm thick aluminum cylinders, which also serve as the pressure vessels.

The position of each of these foundations with respect to the endplate of the chamber is determined using a positioning system based upon a precision bearing which rests between a pair of two opposing conical sockets located in the foundation and the chamber endplate (see Figure 2–20). The first set of sockets were epoxied into a precision machined, steel template known as the master gage, which served as the definition of the relative positions of the sockets for foundations which would attach to one end of the chamber. To transfer the positioning from one system to the foundations or the chamber endplates, the master gage was bolted onto pieces

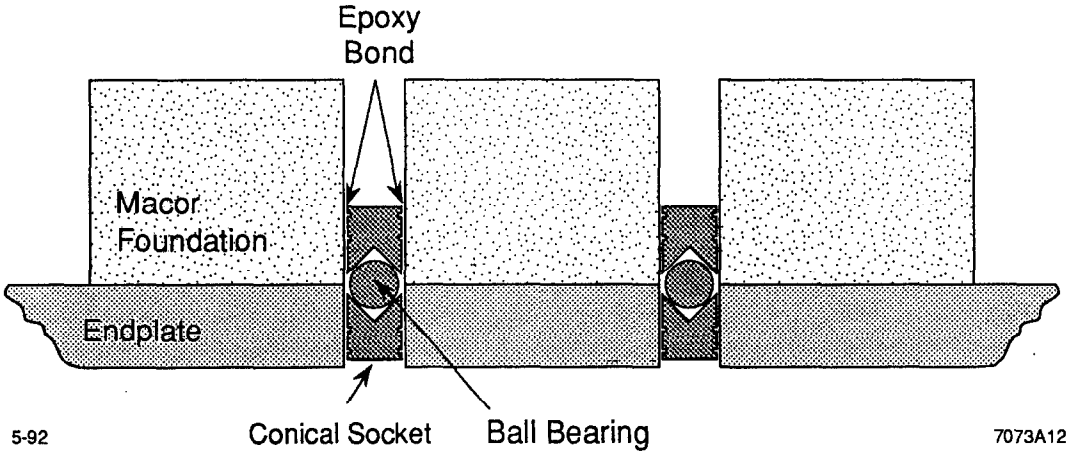

Figure 2–20 Cross sectional view of the ball-and-socket system used to locate the Macor foundations within the chamber.

requiring positioning sockets, and the sockets were glued into this piece — their position determined not by the hole in the piece, but rather by the socket position on the master gage. To affix sockets into the pieces whose sockets were set with the master gage, a second gage, the mirror gage, was used. This is a mirror-image duplicate of the master gage, and had its socket positions set from the master gage. It must be noted that this system of alignment does overconstrain the system and so care must be taken when epoxying the sockets. Nonetheless, it produces mating pairs whose positions are reproducible to ~1 μm.

The wires were positioned onto the Macor foundations using a system of granite blocks to which the socket positions of the master and mirror gages had been transferred. The wire planes were wound to the desired tension onto very precise copper-clad Invar* cylinders and lowered over the foundation and epoxied to that foundation. Note that the wires do not contact the Macor itself, but are bonded to it by a thin layer of epoxy. Thus, the wire position within a plane is largely determined by the accuracy of these Invar cylinders. As part of the wire bonding apparatus, a traveling microscope was built which allowed the wire positions within planes to be accurately surveyed for quality control. The wire position measurements for a plane of sense wires is shown in Figure 2–21 from which it is evident that the wires can be located within a plane to only a few microns.

The electrical connection to the wires are made via a solder connection to flexible kapton printed circuits. Pressure/high voltage feedthroughs have been

* Invar is an iron-nickel alloy with a low thermal expansion coefficient.

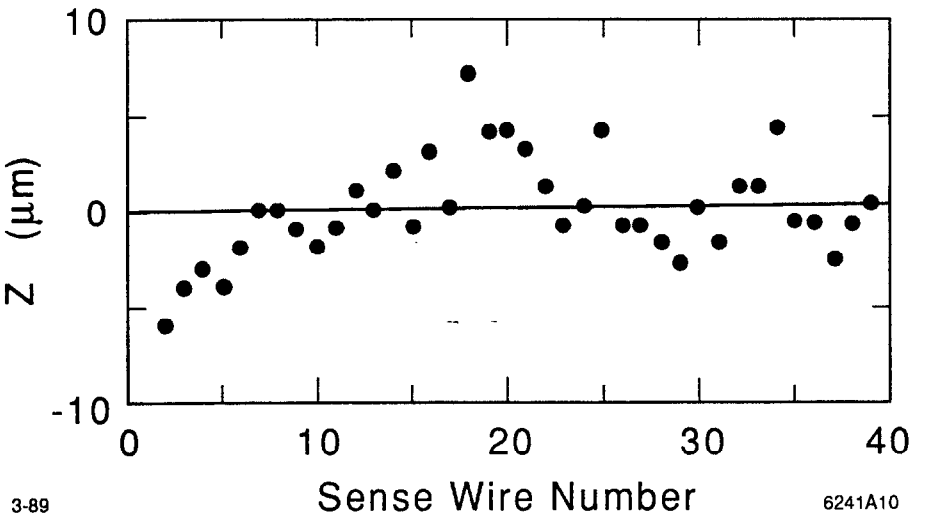

Figure 2–21 Measured deviations for wires within a completed sense wire plane.

expoxied onto these kapton circuits which form the gas seal at the pressure head (see Figure 2–22).

To position the sockets in the endplates of the detector, the master and mirror gages were used to transfer the socket positions to the opposing endplates. The angular position of the socket was determined by an Ultradex Model B precision dividing head, to which the endplate was attached. The master and mirror gages were mounted onto the endplates and a system of precisely cut granite blocks were used to align the endplates with respect to each other on the beryllium central core The endplates were then expoxied to the central core. This method achieved endplates which are parallel to within ±25 μm and have a relative rotation of less than ±40 μrad. The final positioning accuracy of the wires is illustrated in Figure 2–23. This demonstrates that the gaps between the sense and grid planes are the nominal 1.8 mm to within a tolerance of ±25 μm for all but one of the twenty gaps.

2.2.3.2 Gas and Temperature Control Systems

The chamber gas is a mixture of 92% carbon-dioxide (CO_2) and 8% ethane (C_2H_6). The ethane is added to provide quenching by absorbing photons from the electron avalanche at the sense wire before the photons could reach the cathode and extract photo-electrons. The gas is at an absolute pressure of 2 atm and the drift field is E/P = 0.77 kV/cm/atm. With this field, the drift velocity is well in the unsaturated regime in which the drift velocity is linearly proportional to the

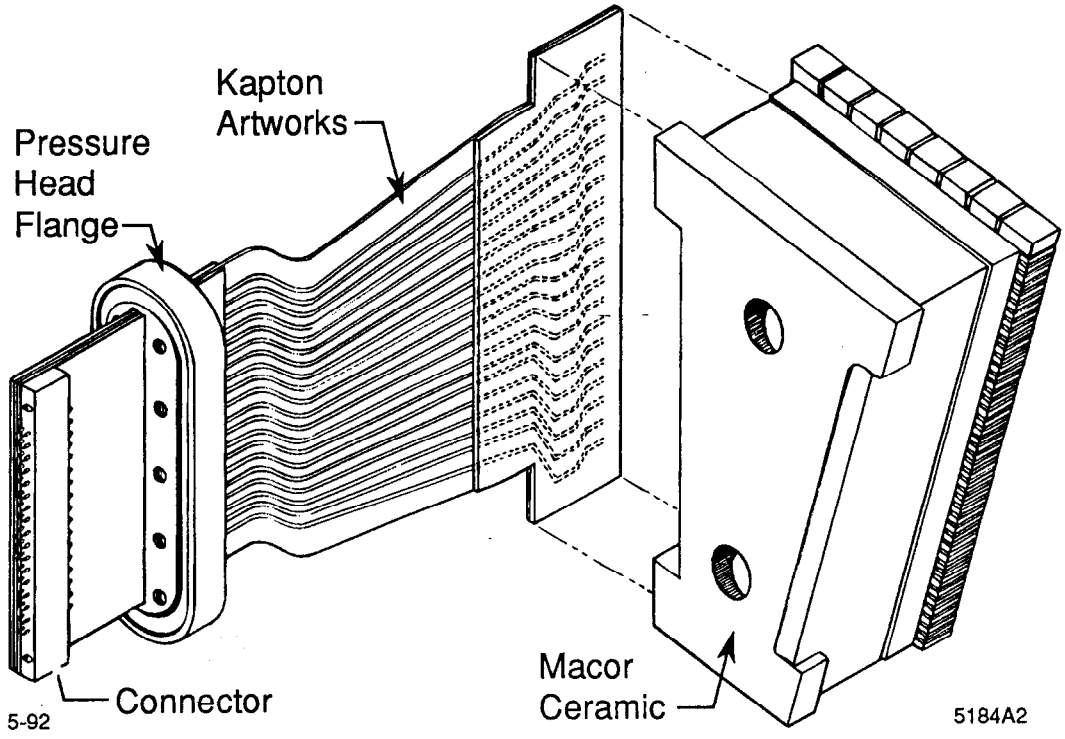

Figure 2-22 A schematic view of the Macor foundation, the kapton printed circuit and the pressure/high voltage feedthrough.

reduced drift field. This makes the drift-time relationship dependent on precise knowledge of any non-uniformities of the drift field. However, these operating conditions are potentially beneficial because this gas mixture is a *cool gas*, meaning that it exhibits electron diffusion which is near its thermal lower limit. Furthermore, cool gases typically have much slower drift velocities, in this case v_d = 5.7 μm/ns. A consequence of operating in this unsaturated regime is that the control of physical conditions inside the chamber such as the pressure, temperature, and composition of the chamber gas and the electric drift field is of particular importance. The drift field control is discussed in the next section. A more complete discussion of the gas studies and these control systems can be found in Appendix B.

The gas system is non-recirculating and uses commercially-made gas mixtures, which are purchased in large quantities in order to assure a constant gas composition. It is important that the amount of electronegative component to the gas in the chamber be as small as possible in order to minimize the charge lost at longer drift distances. This requires that the gas supplied by the vendor be of high

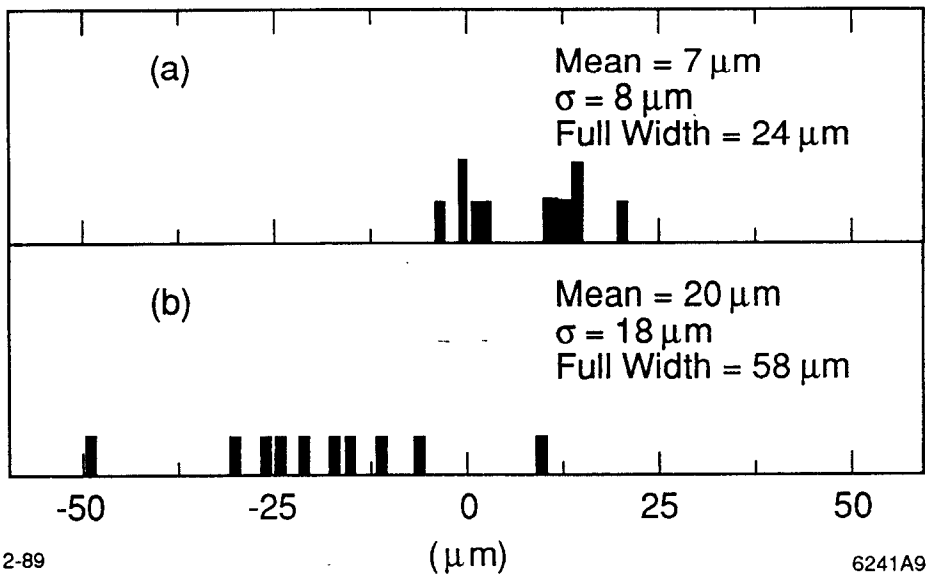

Figure 2–23 Deviation of the sense plane/grid plane gap from the nominal 1.8 mm for grid planes (a) whose Macor foundations do not support cathode planes and (b) for those foundations which also support cathode planes.

purity and that the DCVD gas system not admit atmospheric oxygen. Oxisorb was used to remove all but about 0.2 ppm of O_2 from the gas from the tube trailer, which typically had 1–2 ppm of O_2 when entering the gas system. The gas composition was monitored to a relative accuracy of 0.1 ppm O_2 by a Teledyne Model 316 Oxygen Analyzer and to the level of 0.01% ethane by a Teledyne Model 325 Thermal Conductivity Analyzer. The pressure was measured by a Barocell pressure sensor and controlled to the level of 7×10^{-4} atm by an electronic feedback system, the Datametrics Type 1501 Controller.

The gas temperature was also controlled by an electronic feedback system which maintained an average temperature of 28.15±0.05° C. This system recirculates water through a closed loop system from a 15 liter reservoir to the chamber, where the water is sent through 0.25″ aluminum tubing which has been attached to the pressure heads on either end of the chamber and the outer shell of the DCVD. The beryllium inner core is the only section of the chamber whose temperature is not actively controlled. The temperature of the water in the reservoir is controlled by a HAAKE N 2-R Digital Cryostat. The temperature monitoring system uses an array of 48 thermistors placed on and around the chamber. The temperature measured from these thermistors are sent to the VAX host computer where a feedback program adjusts the temperature setting of the cryostat. As it is not actively

temperature controlled, the inner core exhibited temperature fluctuations of ±0.15° C and the temperature variation between the inner core and outer shell was less than 0.35° C.

2.2.3.3 High Voltage System

Because the chamber is used in an unsaturated regime, the drift velocity depends linearly on the drift field, and thus it is crucial to precisely monitor and control the field voltages supplied to the chamber. To achieve this, great care was taken in both the assembly of the high voltage components such as the resistor-divider chains, and in the choice of voltage monitoring equipment.

A single high voltage supply powers the ten resistor-divider chains from which the cathode wire and edge field wires are supplied. The remainder of the voltages are controlled by separate supplies. These supplies are controlled from a feedback system on the VAX host computer, which sends information via CAMAC to the power supplies. The high voltage for the DCVD is measured to an accuracy of a few parts in 10^4 using a FLUKE Model 8506A digital multimeter which itself has a 5 ppm accuracy, and the resulting measurement sent in digital form to the VAX. This system is illustrated schematically in Figure 2–24.

Excess current in the cathode system is monitored by comparing the voltage differences from near the top and bottom of the resistor-divider chain with a reference chain. The other systems monitor current at the power supply. If excess current is detected, the chamber protection system is activated and within a few milliseconds the high voltage systems in the chamber are connected to 80 MΩ discharge resistors.

The voltages have been monitored during running and show that the extended stability of the cathode high voltage supply is 0.03%. The anode high voltage supplies were stable over the same period to 0.3%.

During the 1990 data run, there were often rather severe backgrounds in the DCVD (see Section 2.2.3.6). The high level of backgrounds led to some high voltage problems within the chamber. During periods of high backgrounds, it was not uncommon for the sense wires in one of the cells to begin drawing excessive current and eventually trip off the protection circuits. The damage was only temporary and could be fixed by leaving the sense wire high voltage at 1000 V for a period of several hours. Although the cause of this was never conclusively determined, one possibility is that charge was building up, perhaps in the gap between Macor foundations, which had an RC time constant of roughly an hour. Studies of the cells adjacent to that with the lowered sense show no detectable degradations in

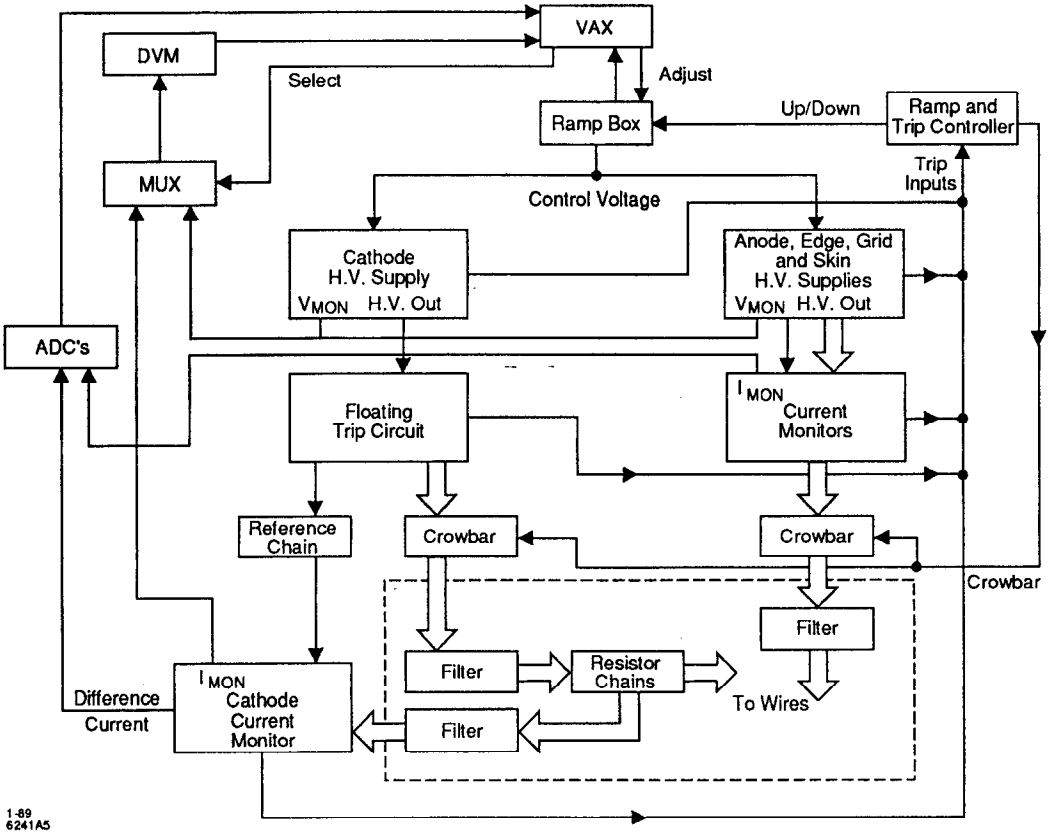

Figure 2–24 A schematic diagram of the DCVD high voltage system.

chamber performance as measured in terms of the single hit and cosmic miss distance resolutions.

2.2.3.4 Electronics

The signals from the sense wires are fed into 38-channel preamplifier cards which are mounted on the ends of the chamber. Each channel contains a fast, charge sensitive hybrid amplifier with a 40 nsec integration time. The preamplifiers are connected to postamplifiers by 30 feet of standard 50 Ω cable. The postamplifiers, located just outside the Mark II magnet iron, contain a pole-zero filter which compensates for the integration of the preamplifier and removes the $1/t$ ion tail. The postamplifiers are connected to 6-bit 100 MHz Flash ADC's with a memory depth of 1024 bins.[67] These 16-channel FADC's reside in two FASTBUS crates in the Mark II data acquisition building. The data is read from the FADC modules into SLAC Scanner Processors[55] (SSP's), one of which is located in each FASTBUS crate. The SSP's provide hit recognition, time and change measurement, zero-suppression and formatting for the raw and processed data. The overall gain

has been set such that the root-mean-square thermal noise is about half of one FADC count.

2.2.3.5 Hit and Track Finding Algorithms

A differential hit finding algorithm[68] is used to locate hits in the FADC data. This algorithm aids in separating closely spaced hits where the second hit is on the tail of the first. In such cases, a fixed threshold algorithm would have less tendency to find the second hit as the pulse height may not yet have dropped below the threshold. The differential algorithm steps through the 1024-bin digitalized pulse train bin by bin, forming the difference between the sum of three adjacent bins and the three following bins. The leading edge is flagged if this difference exceeds a threshold which decreases slightly with drift distance in order to account for the effects of diffusion and attenuation. A trailing edge is flagged when the difference of the sums is negative for two consecutive bins. A further cut is made which requires the integrated pulse height of the hit be larger than a second threshold in order to reduce the number of smaller fake hits from late arriving clusters. The time assigned to each hit is then calculated as,

$$t = \frac{\sum_i (\alpha)^i p_i \cdot t_i}{\sum_i (\alpha)^i p_i}, \qquad (2\text{-}1)$$

where i is the bin number counting from the bin at the leading edge of the hit, p and t are the pulse height and time of the i^{th} bin and $\alpha < 1$ is a constant which varies linearly with the drift distance and is adjusted to optimize the resolution. This form is useful because a typical pulse has a fast risetime which is determined by diffusion, ion statistics and electronics. In contrast, the much longer trailing edge is dominated by the non-isochrony of the cell and the late-arriving clusters and so contains less useful time information. The performance of this algorithm on closely spaced tracks is discussed in Section 2.2.3.8.

The pattern recognition algorithm which identifies charged tracks in the DCVD employs two stages to achieve maximum track finding efficiency.[69] In the first stage, track segments in the DCVD are sought using a *curvature module* approach.* This approach searches through regions of constant azimuthal angle, ϕ, and curvature, κ, looking for a collection of hits with the same ϕ and κ. The algorithm is

* This is named after the hardware curvature modules employed in the trigger system (see Section 2.2.8, "Trigger System," on page 84).

designed to be fully efficient for tracks with $p_{xy} > 250$ MeV/c and a distance of closest approach to the origin, δ_{xy}, of less than 4 mm. These segments are further refined by adding and subtracting hits based on the residuals to a fit of the hits to a circular arc in the xy plane. Occurrences of ten or more hits are then considered track segments.

The next step is to attempt to join these track segments to the tracks found in the CDC. To do this, a χ^2 is formed between the CDC track and DCVD segments with an arbitration procedure for closely spaced tracks. This χ^2 is involves the match of the three track fit parameters in the xy plane (δ_{xy}, ϕ and κ) with an additional term to allow for scattering in the material between the two detectors. Hits on segments for which a matching CDC track is not found are then used in the second stage of the algorithm.

This stage begins by using the tracks found in the CDC for which no DCVD hits were found and extrapolating the track into the DCVD, then looking for the nearest hit starting in the outermost layer. The process continues layer-by-layer, adding each hit to the track if it passes a χ^2 cut and recalculating the track parameters.

These methods are complementary, particularly in hadronic events. The first stage is particularly adept at finding hits in dense jets and regions of many spurious hits caused by the backgrounds in hadronic events (see Section 2.2.2.5). It is, however, not efficient for the lowest momentum tracks or tracks with large impact parameters. These are tracks which can be more readily found with the second stage algorithm. The major drawbacks of this part of the algorithm, and the impetus of using the other stage first, is that this algorithm can become confused when tracks are closely spaced or the track passes through a region of high backgrounds. This happens when a few wrong hits are associated with the track, forcing the track fit off of the correct trajectory and making it unlikely that subsequent correct hits will be added.

Once the DCVD hits have been associated with the tracks found in the CDC, the full set of CDC and DCVD hits are refit using the SARCS6 least-squares fitting routine (see Section 2.2.2.4). There are regions in the jet cell in which the electric field has non-uniformities which are not fully modelled in the time-distance relation, and consequently, it is chosen to discard the hits from these regions prior to the track fit. (Investigation of these effects is considered more thoroughly in Sections 2.2.3.7 and 2.2.3.8.) To this end, it is required that a hit not be on the innermost two or outermost four wires, whereas the hit finding algorithms use layers 3 through 36. Hits which are further than 20 cm from the center of the

chamber also are removed. Finally, hits which are within 2 mm of the sense plane or 3 mm of the cathode plane have their resolution inflated in order to minimize their effect on the track fit.

In addition to the five conventional track parameters, a sixth parameter is included in the fit which allows a kink in the track due to multiple scattering in the material between the detectors. The multiple scattering inside the chambers due to the gas and wires is taken into account by modifying the resulting error matrix according to the formalism of R. Gluckstern.[61] It should be pointed out that this formalism does not strictly apply in this case, as it assumes that the scattering region contains equally-spaced measurements of the same resolution. However, Monte Carlo studies have demonstrated this formalism is satisfactory in this case, particularly because of the large number of layers.

2.2.3.6 Backgrounds

Data recorded during the 1990 SLC run showed that there was a significant amount of beam-related background in the DCVD. Figure 2–25 shows the hits detected by the DCVD in a typical random-trigger event from this run. The

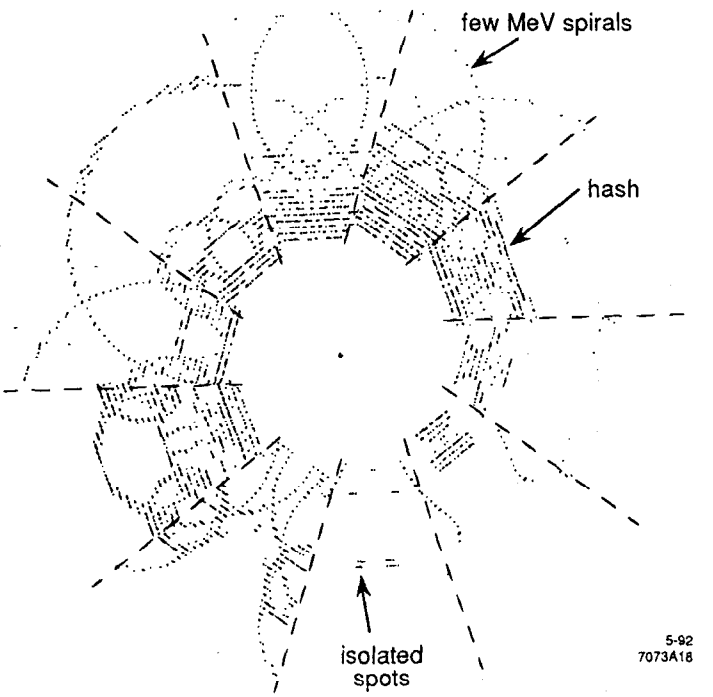

Figure 2–25 A typical random trigger event illustrating the level of backgrounds in the DCVD. The DCVD hit occupancy in this event is 20%. Note that each hit is shown on either side of the sense plane because locally it can not be determined from which side of the sense plane the hit originated.

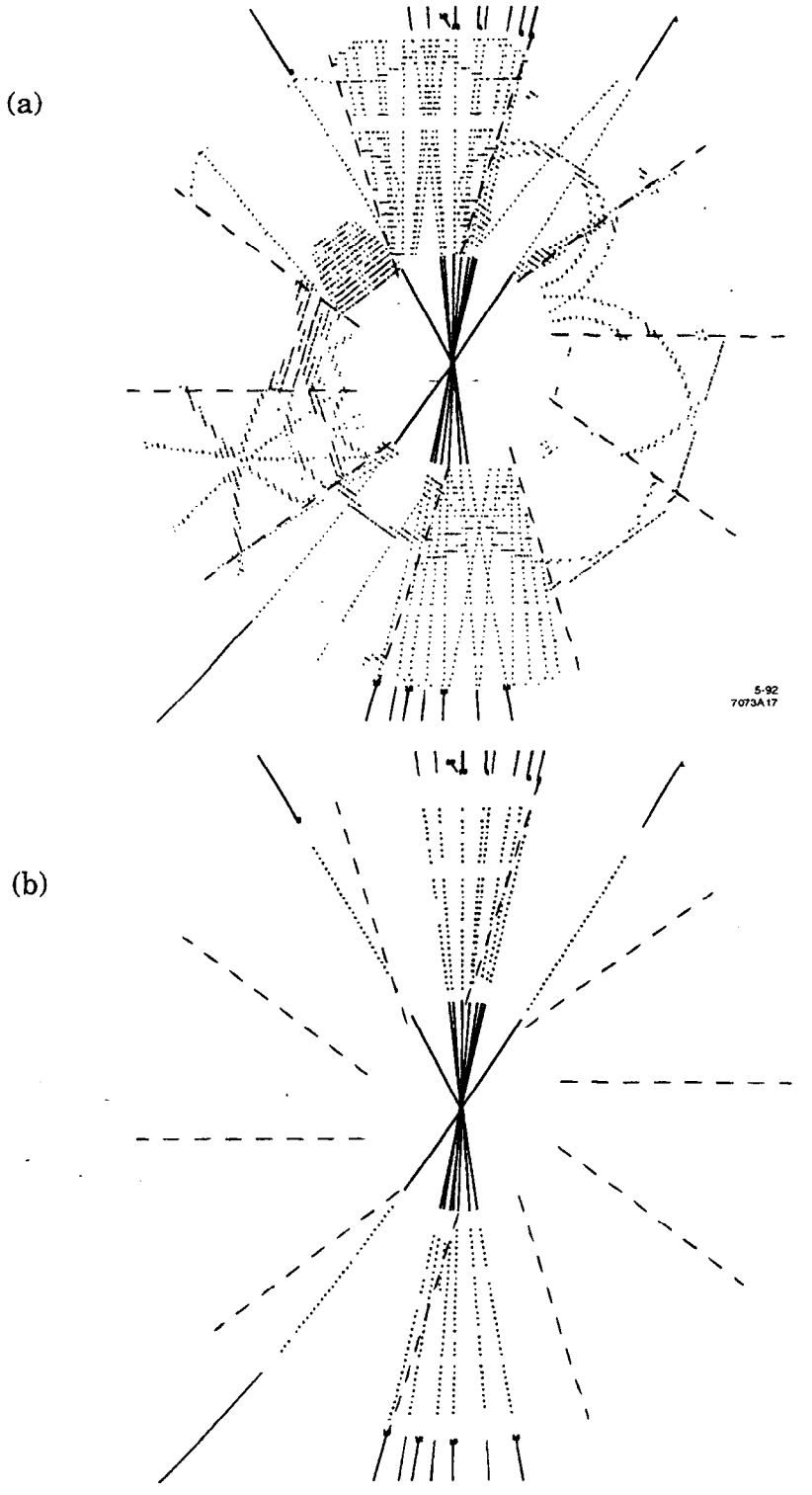

Figure 2–26 A typical hadronic event in the DCVD showing: (a) all detected hits, and (b) those hits assigned to tracks. This event has an occupancy of about 23%. In the upper plot each hit is shown on either side of the sense plane because of the local left-right ambiguity.

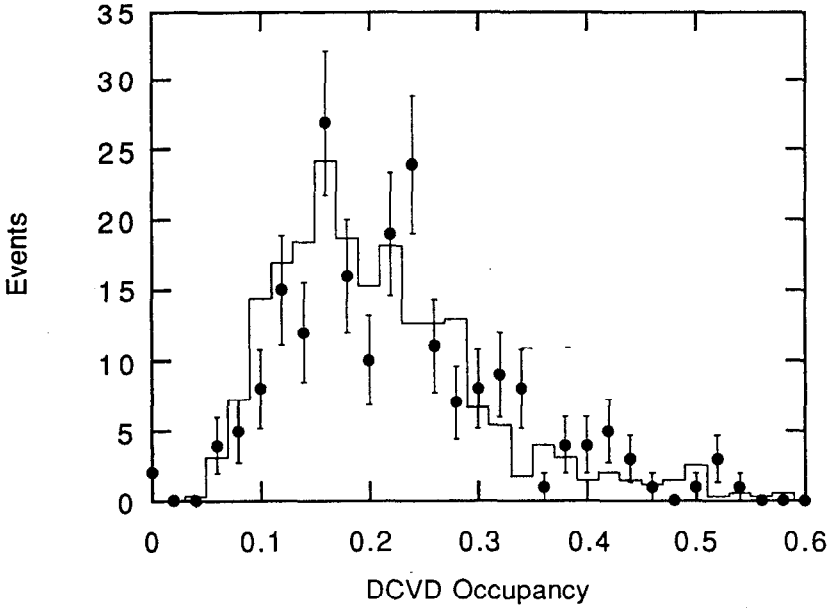

Figure 2–27 The DCVD occupancy observed in hadronic events. This does not account for events during which one or more DCVD cells was off. The points are the data and the line is the Monte Carlo with mixed background as described in Section 3.4.

background consists primarily of several distinct types. The spirals are electrons from photon conversions produced with a few MeV/c of momentum in the xy plane. The hash which is typically found in the inner layers is thought to be caused by a large number of very low energy particles, potentially produced from electromagnetic showers. Finally, the smaller spots due to photon conversions in the gas volume. Figure 2–26 illustrates the backgrounds in a hadronic event. As illustrated by this event, the DCVD hit finding algorithms nonetheless prove sufficiently robust to adequately reconstruct the tracks despite this level of background.

The level of backgrounds in the DCVD was characterized in terms of the occupancy, which is defined as the fraction of physical FADC bins in the chamber included in the found hits. The levels varied greatly, with most hadronic events having occupancies of about 20%, though events were observed with occupancies >50% (see Figure 2–27). The event illustrated in Figure 2–26 is typical in another fashion, which is that the backgrounds tend to be most severe at smaller radii, as illustrated in Figure 2–28. The backgrounds in the CDC are minimal in the 1990 data. (During the 1989 running, the CDC had significantly worse backgrounds which were reduced because of new masking and the material in the DCVD.) The

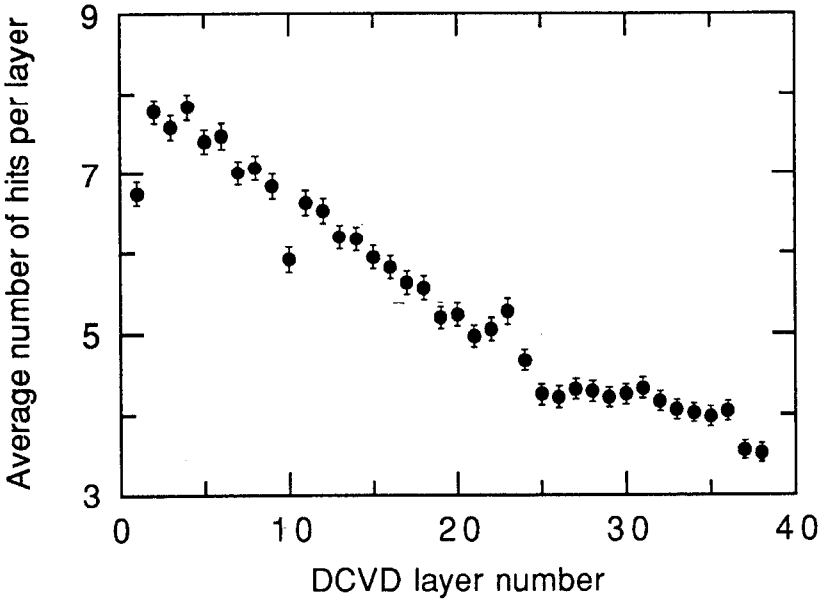

Figure 2–28 Number of hits observed per DCVD layer as a function of the layers number, illustrating the increased backgrounds at the inner layers.

SSVD also saw much less background than the DCVD, despite its much smaller radius. This is quite simply a result of the much smaller active volume of the SSVD.

2.2.3.7 Time-Distance Relation

In order to achieve the optimum resolution it is necessary to carefully study the relation between the drift time of a hit and the distance which it had drifted, called the *time-distance relation.*[70] As mentioned previously, the DCVD is operated in the unsaturated regime, such that the drift velocity varies linearly with E/P. Thus, understanding drift fields in the cell is crucial.

The first step in understanding the electric field is an analytic solution for the strength of the field along a line from a sense wire perpendicular to the sense plane. This solution, though calculated for an infinite wire plane array, describes the field to an accuracy of about 0.1% in the center of the jet cell, based upon comparison with a detailed electrostatics simulation. Using published data of the drift velocity in CO_2 as a function of E/P,[71] and scaling these results up by 10% based on our measurements in order to account for the addition of 8% ethane, a first-order time distance relation was derived (see Figure 2–29). For tracks which are not parallel to the sense plane, the electrons are assumed to drift in a direction perpendicular to the sense plane until they are at a radius of 1.78 mm from the sense wire. From

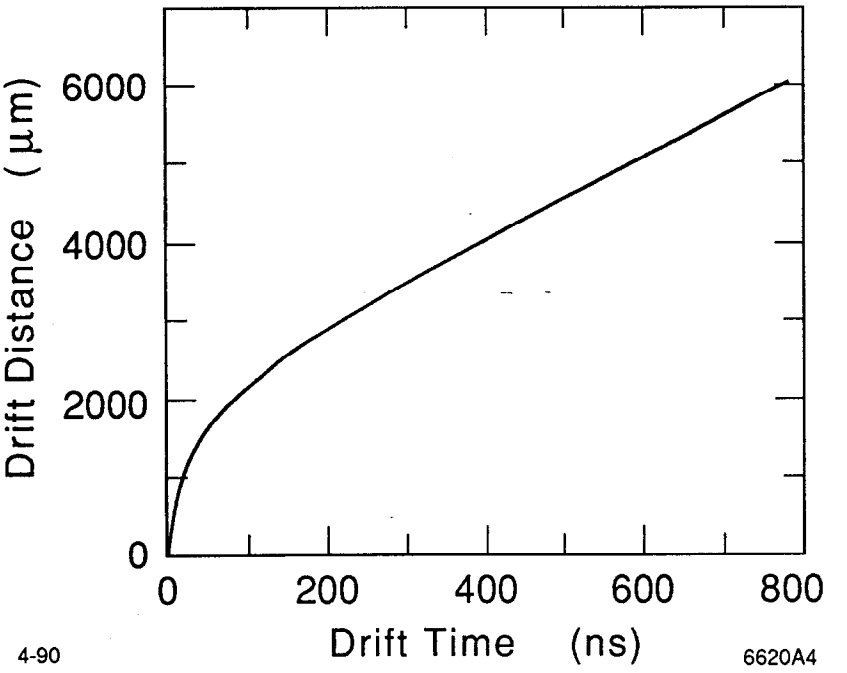

Figure 2–29 Time-distance relation as calculated from the analytic electric field calculation. Beyond 6 mm the drift velocity is assumed to be constant.

that point, the electrons are assumed to drift toward the sense wire radially. This radius is chosen to match the line of constant drift time based on the electrostatic simulation. The same time-distance relationship shown in Figure 2–29 is used for tracks not parallel to the sense plane, except that the drift distance is taken to be the length of this modified trajectory. The 4.75 kG magnetic field tilts the drift trajectories slightly by the Lorentz angle of 18.2 mrad.

To account for the perturbation of the electric field near the edges of the jet cell, a full electrostatic simulation was used to generate corrections to the first-order analytic model. This correction is based on a comparison of the electric field calculated by the simulation for all drift distances and wires in the DCVD jet cell. The resulting correction to the drift distance is shown in Figure 2–30 as a function of drift distance and wire number. The level of this correction can be as large as 10% for the wires on the extreme inner and outer edges of the cell. A smaller correction is also applied which accounts for tracks which are not parallel to the sense plane.

Finally, cosmic ray events have been used to refine the time-distance relation further. This is done by assuming a functional form which includes terms up to third order in the signed drift distance and wire number, then with a global 22-parameter fit, minimizing the residuals of the cosmic tracks. For this study, the

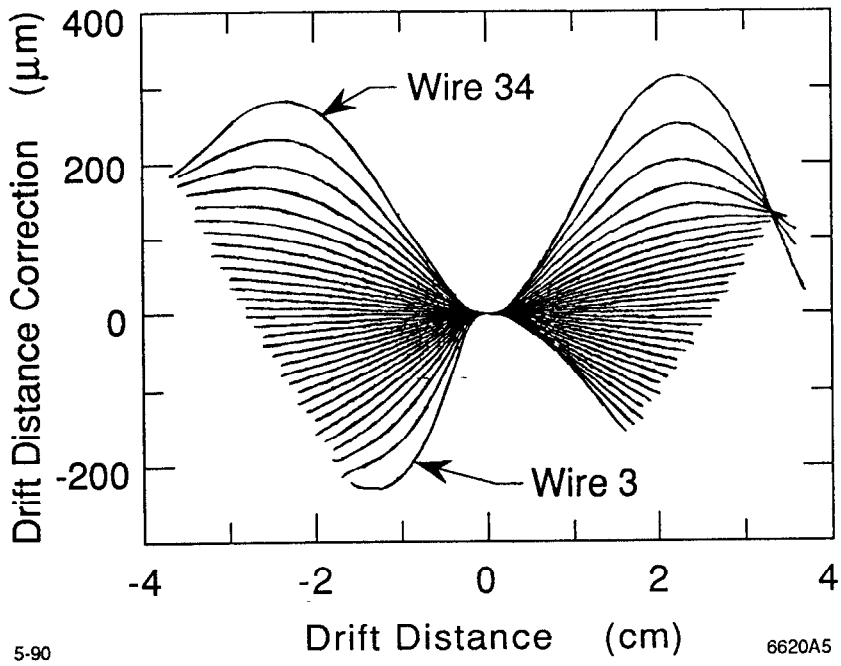

Figure 2–30 The drift distance correction to the first-order analytic model, as calculated by the full electrostatic simulation, is shown as a function of drift distance for the various DCVD layers.

cosmic rays are required to have $p_{xy} > 5$ GeV/c and a distance of closest approach to the chamber center in the xy plane which is less than 2.5 cm. Furthermore, the two halves of the cosmic ray are fit to a single trajectory. The results demonstrate that there are variations, which are less than 50 μm for all but the outermost layers, that were not included by the electrostatic correction. The results of this empirical correction are shown in Figure 2–31. A similar, but lower dimensional fit to the DCVD residuals in the cosmic events was used to determine the physical alignment of the DCVD with respect to the CDC.

2.2.3.8 Position Resolution and Efficiencies

The DCVD position resolution was studied primarily with the aid of track residual distributions. The track residual, δ, is defined as the difference between the hit location for a given layer and the position predicted for that layer by the track fit. It is expected that the resolution should be the sum of two terms in quadrature. The first is an intrinsic term which is related to the intrinsic gas properties (ionization statistics and amplification) and the hit timing strategy. The second term is due to the diffusion of the electron pulse. For a particular choice of chamber gas, the amount of diffusion depends on the square-root of the drift time,

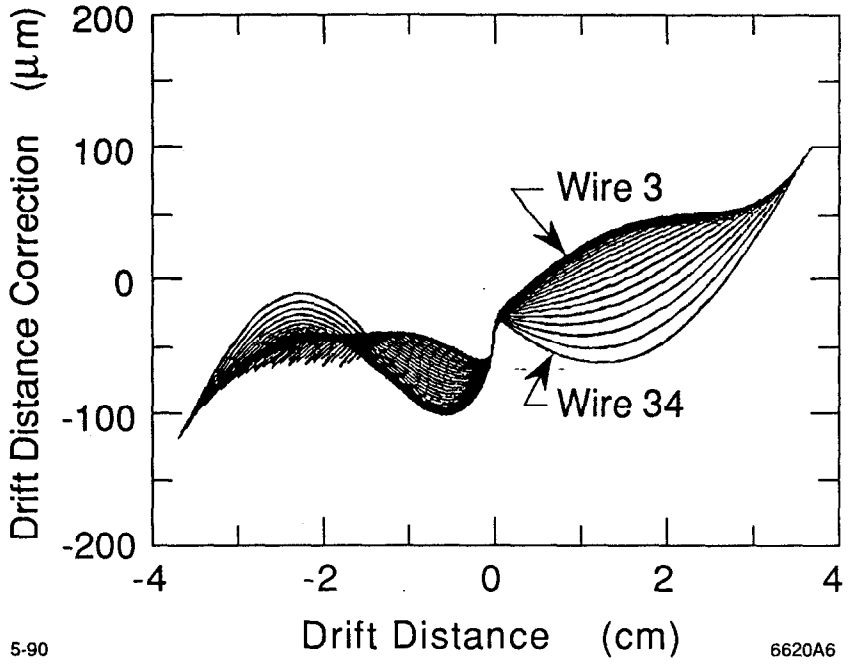

Figure 2–31 The empirical correction to the time-distance relation based on cosmic ray studies.

or for a constant drift velocity, the drift distance. The position resolution is thus expressed as

$$\sigma_x^2 = \sigma_{int}^2 + \sigma_{diff}^2 \cdot D \tag{2-2}$$

where σ_{int} and σ_{diff} are the intrinsic and diffusion coefficients, and D is the drift distance. The residual distributions were studied using tracks with $p_{xy} > 1$ GeV/c. The rms widths were calculated with a cut requiring that the normalized residuals, δ/σ_δ, be less than 4 to prevent the widths from being dominated by the tails.

Figure 2–32 shows the variance of the residual distributions binned as a function of drift distance for cosmic ray data taken during 1990. A fit to this data yields,

$$\sigma_x^2 = (12.4 \pm 0.8\ \mu\text{m})^2 + (40.2 \pm 0.3\ \mu\text{m})^2 \cdot D, \tag{2-3}$$

where D is in units of cm. There is potentially a small systematic shift toward poorer resolution than is found by the fit at large drift distances. However, this region is sparsely populated with hits compared to lower drift distances and thus has less statistical strength in the fit.

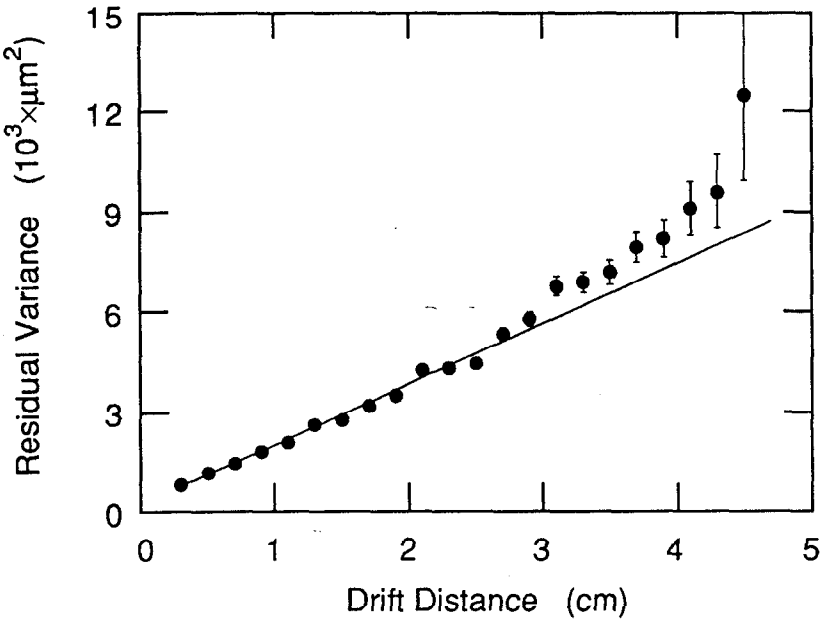

Figure 2–32 The DCVD resolution as a function of drift distance for cosmic events, and a linear fit to these points.

Of more concern is the resolution in hadronic events. This was studied in a similar fashion using track residuals. It was found that the resolution of hits in hadronic events depends not only on the drift distance but also on the layer in the DCVD (see Figure 2–33). It was found empirically that this dependence could be parameterized adequately with a simple dependence on the layer number, L:

$$\sigma_x^2 = \sigma_{int}^2 + \sigma_{diff}^2 \cdot D + \sigma_{layer}^2 \cdot (19 - L). \tag{2-4}$$

Binning the residuals in terms of drift distance and layer number, the above functional form was used to fit the residual variances. The result is:

$$\sigma_x^2 = (28.4 \pm 0.8\ \mu m)^2 + (43.0 \pm 0.5\ \mu m)^2 \cdot D + (7.58 \pm 0.2\ \mu m)^2 \cdot (19 - L), \tag{2-5}$$

where the drift distance, D, is in units of cm. This function can be more readily understood by viewing it graphically, as done in Figure 2–34. From this, it is evident that compared to the resolution of cosmic events, the hadronic event position resolution is significantly degraded at the inner layers, but is very nearly the same as cosmics at the outer layers.

There are primarily two explanations for the poorer resolution at the inner layers. One is that at the inner layers the hits from closely spaced tracks will be more likely to overlap and thus potentially affect the measured time of the latter

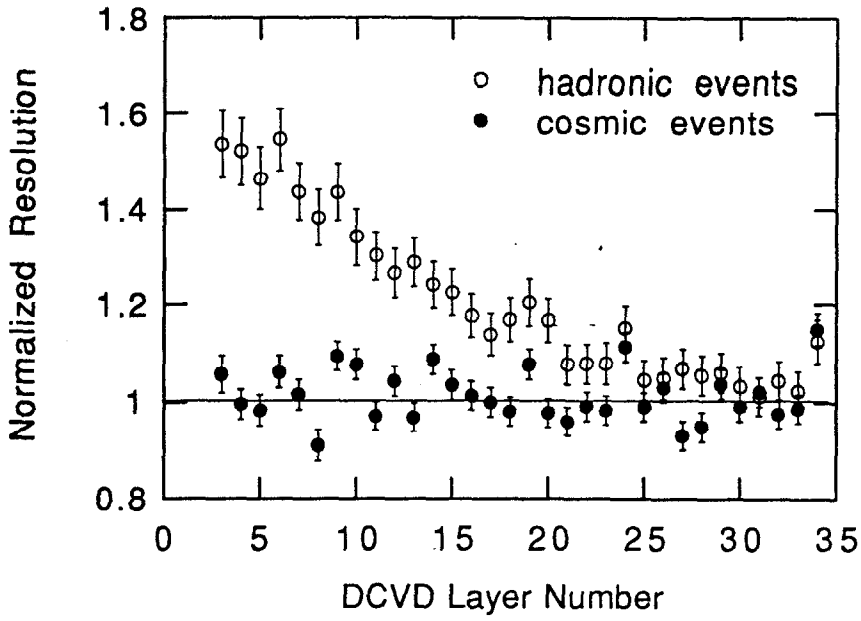

Figure 2-33 Normalized residuals as a function of wire number for cosmic events and hadronic events of all drift distances. In this plot, the hadronic residuals were normalized with the values calculated for cosmic events, Equation (2-3).

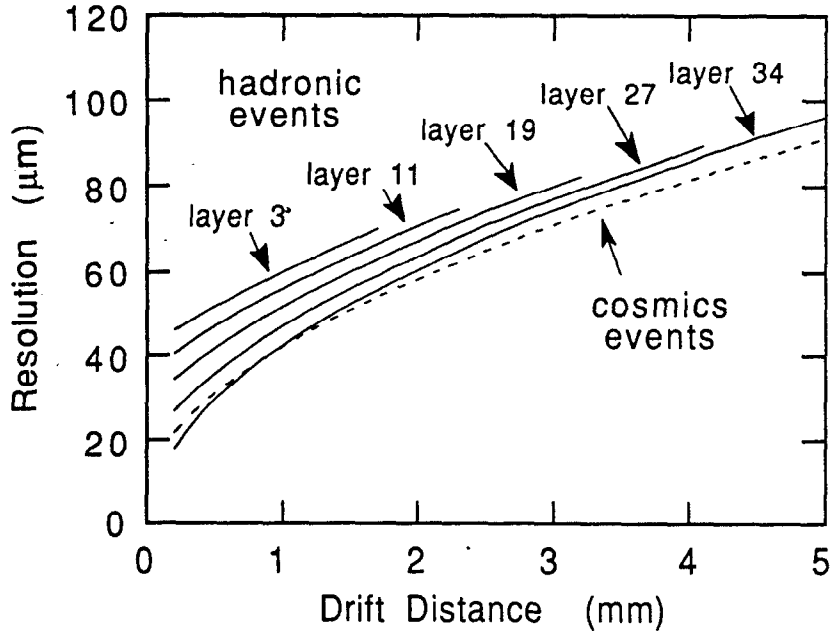

Figure 2-34 The fit resolution as a function of drift distance for hadronic events and cosmic events.

hit. The other possibility is that it is simply related to backgrounds, which as shown in Section 2.2.3.6 are more severe at the inner layers.

To determine the source of the degraded resolution, the Monte Carlo was employed. Specifically, the resolution measured in the Monte Carlo with full detector simulation can be compared for three different sets of Monte Carlo events: muon-pair events, hadronic events with no beam-related background added and hadronic events with the beam-related backgrounds similar to those observed in the data.* The muon pairs in the Monte Carlo show no dependence on the DCVD layer number, as similarly cosmic events did not. The hadronic events with no background have only a slight dependence on the layer number. For these events, there is a fractional resolution difference between the inner and outer layers of 10% at a small drift distance of 2 mm (where the fractional effect of wire dependence is most acute). The hadronic events with the backgrounds applied show much more layer dependence, with the same fractional difference of 55%. Thus it is clear that the majority of the resolution degradation is in fact due to the presence of backgrounds, with only a fairly small contribution from the closely spaced tracks.

The resolution also exhibits a dependence on the polar angle of the track, θ. The length of the track segment from which charge will drift to a particular sense wire will increase as $(\sin\theta)^{-1}$. The average amount of deposited charge will increase accordingly. Thus, the statistics will improve and the resolution with which the pulse time is determined should vary as $(\sin\theta)^{-1/2}$. As illustrated in Figure 2–35, this was indeed found to be the case, and a correction was applied to the resolution to account for this. The correction is $1.057/\sqrt{\sin\theta}$, where the constant is chosen to leave the overall resolution unchanged.

The resolution and time-distance relation were also investigated in some of the potentially problematic regions of the jet cell. Hits which were within 2 mm of the sense plane or 3 mm of the cathode plane were effectively removed from the track fit by inflating the errors assigned to these hits. This was done because the resolution was measured to be significantly worse in these regions than the rest of the cell, since the time-distance relation does not fully account for all of the variation in the field. The position of the hit along the axis of the chamber is also of interest because of the possibility of electric field variations near the ends of the chamber. It was found that hits with $|z| > 20$ cm show some adverse affects in their time-distance relation and the resolution, and thus are not used. The slope of the

* See Section 3.4, "Detector Simulation," on page 102 for information describing the treatment of Monte Carlo hits and backgrounds.

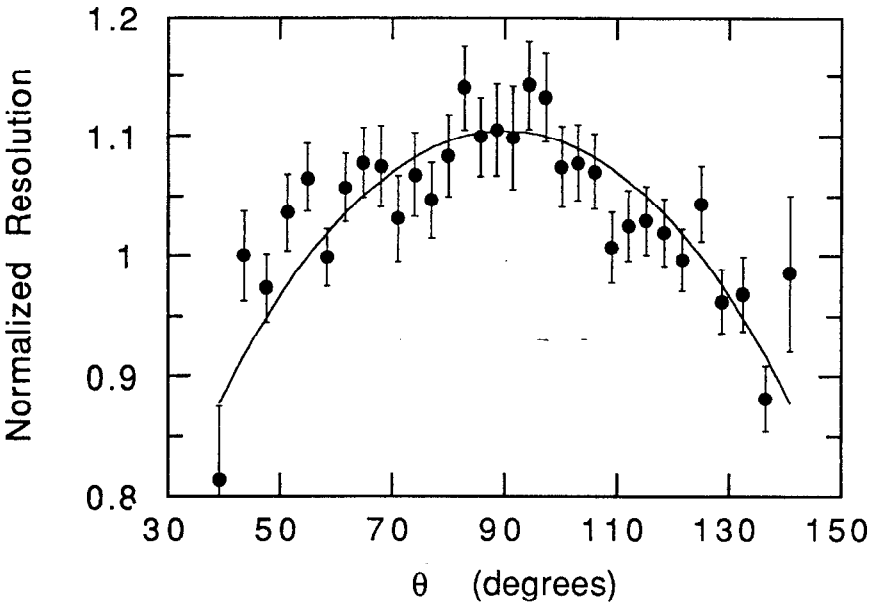

Figure 2–35 The normalized resolution as a function of the polar angle of the track. The line is a fit with a $(\sin\theta)^{-1/2}$ dependence.

track with respect to the sense plane was also investigated. It was found that the corrections in the time-distance relation are adequate and that no resolution degradation is observed.

The double hit resolution was investigated[68] first with the use of a pulse library containing a large sample of pulses from cosmic events. By superposing the pulse trains from different cosmic ray tracks with various separations, the efficiency with which the second hit is found can be studied. It is found that even with hits separated by as little as 400 μm, the efficiency of detecting the second hit is nearly unity (see Figure 2–36). There is however some loss of efficiency until the separation is about 1500 μm because of the effects of the first pulse on the measured time of the second pulse. The fake hit rate has been investigated using cosmic ray data and shows that, as illustrated in Figure 2–36, beyond 700 μm from the first hit the fake hit fraction drops below 10%. Finally, closely spaced tracks in hadronic events have also been used to study the double track resolution and the results are consistent with those determined above.

The hit finding efficiency has been studied and tuned for the best agreement with the data. In the Monte Carlo generation, a single value of the hit efficiency was used to characterize all the sense wires in the detector. Assigning the input efficiency to 0.95 yielded the best data/Monte Carlo agreement. The measured layer-by-layer efficiency varies with the layer number particularly due to the effects of

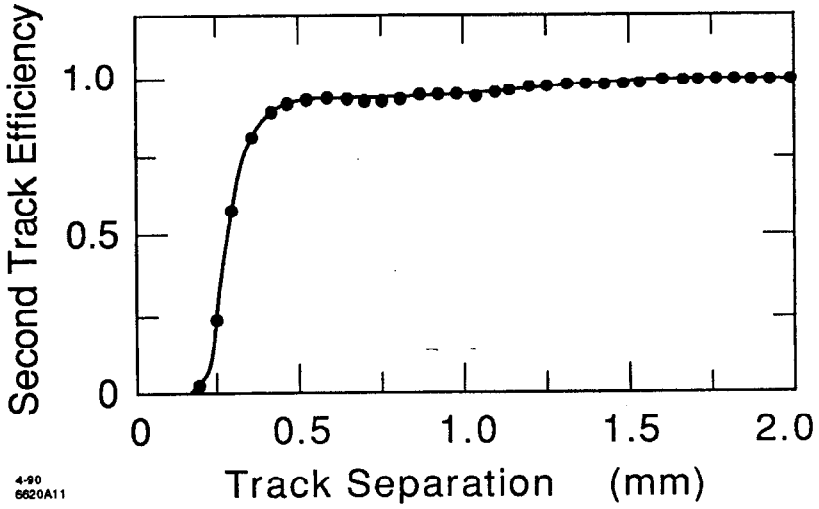

Figure 2–36 The efficiency to detect a second hit as a function of the separation of the tracks at this layer.

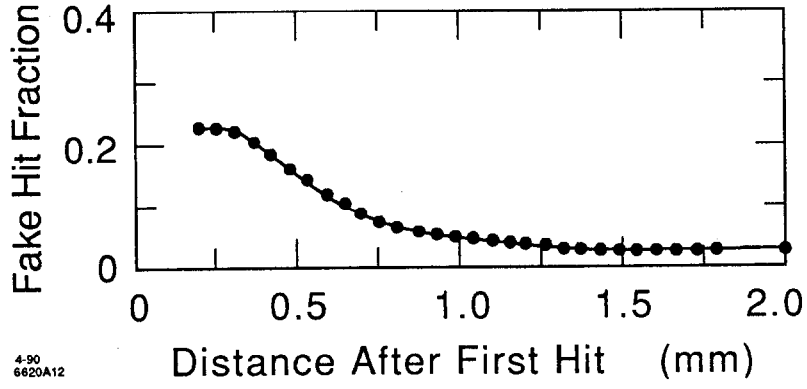

Figure 2–37 The fake hit fraction measured in cosmic events as a function of the distance from the first hit.

higher backgrounds in the inner layers (see Figure 2–38). The distribution of the number of DCVD hits assigned to tracks found in the CDC is shown in Figure 2–39. The general agreement between the data and Monte Carlo is good, although the data has a less-peaked structure. This produces a slightly lower average in the data (21.7±0.2 hits per track) than is predicted by the Monte Carlo (22.2 hits per track).

2.2.4 The Silicon Strip Vertex Detector

The innermost tracking detector, the Silicon Strip Vertex Detector (SSVD), was designed to provide several very high precision measurements of the produced tracks at a location as close as possible to the e^+e^- interaction point. This allows very precise determination of the track impact parameter especially for those tracks

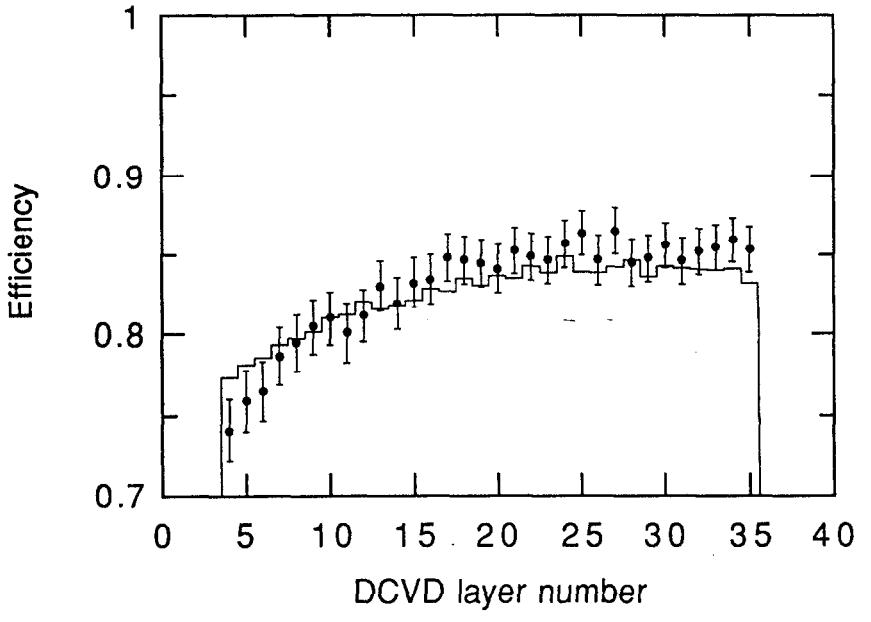

Figure 2–38 The DCVD measured hit efficiency as a function of the layer number for the data (points) and the Monte Carlo (line).

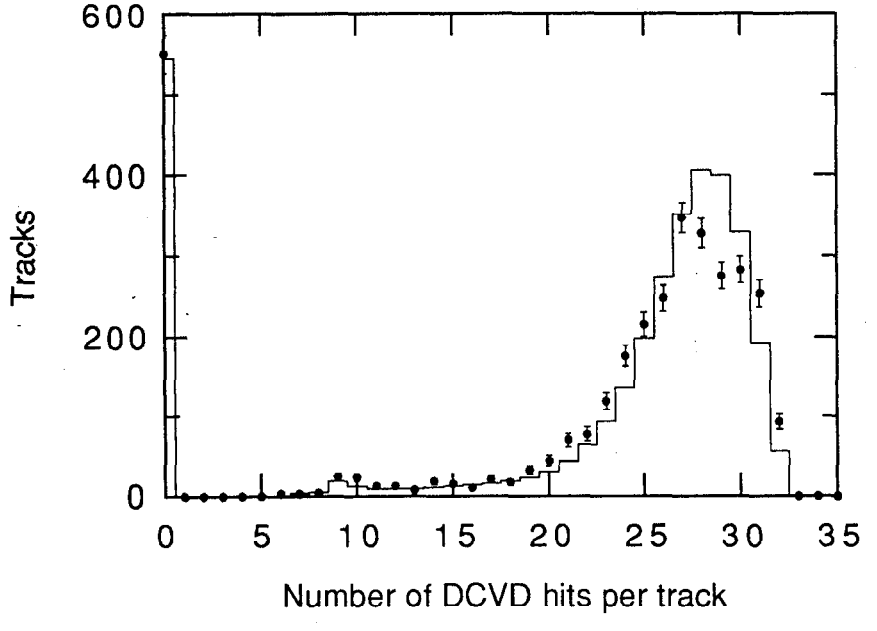

Figure 2–39 The distribution of the number of DCVD hits per track for the data (points) and Monte Carlo (line). These tracks are required to have $|\cos\theta| < 0.8$, $p_{xy} > 0.15$ GeV/c, $|z| < 1.5$ cm, $|b| < 1.5$ cm and $N_{CDC} \geq 25$. Many of tracks with no found DCVD hits were in cells which had their sense voltage lowered due to high voltage problems.

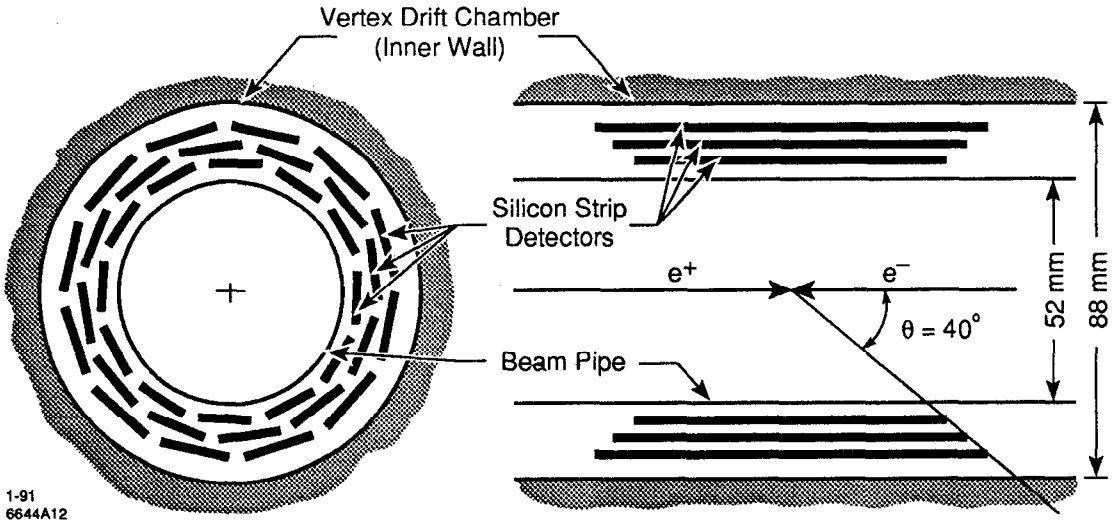

Figure 2–40 Schematic layout of the Silicon Detector Modules in the SSVD.

Layer	Radius	Active Length	Pitch
1	29.4 mm	72 mm	25 μm
2	33.7 mm	82 mm	29 μm
3	38.0 mm	90 mm	33 μm

Table 2–3 Geometric properties of the Silicon Detector Modules used in the three layers of the SSVD.

with high momentum. The design and performance of the SSVD is extensively described elsewhere. In particular, the reader may wish to refer to References [72] and [73] for greater detail than is presented here.

2.2.4.1 Design

The SSVD is designed of 3 layers from 29 to 37 mm from the beam axis. Each layer is comprised of 12 of the Silicon Detector Modules (SDM's), as illustrated in Figure 2–40. Each SDM has 512 axial strips with differing pitches depending on the layer. The average SDM thickness is 314 μm of silicon, which when combined with a small cable beneath the detector is about 0.55% of a radiation length. Table 2–3 summarizes the details for each of the three detecting layers in the SSVD.

The detector is made from two identical halves to facilitate assembly onto the beam pipe (see Figure 2–41). Each half of the detector is held against the beam pipe with a set of three copper springs with a 3 mm sapphire ball to assure that no

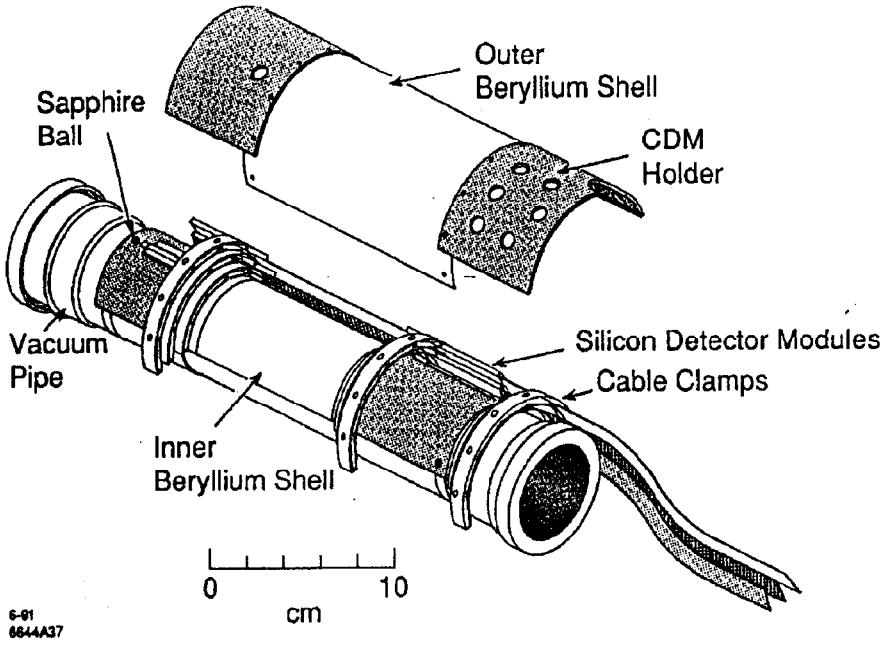

Figure 2–41 Mechanical assembly of the one half of the SSVD.

electrical connection is made to the beam pipe. The SDM's are inserted in aluminum end pieces, held apart by half-cylindrical beryllium shells of a 250 μm thickness. The modules were held in place by spring mounts in the end pieces to assure that the modules remain in the same position even through temperature fluctuations as large as 15° C in 30 minutes. Finally, the cables leading from the SDM's were clamped firmly to prevent them from affecting the detector placement.

2.2.4.2 Electronics

The first stage of the readout electronics utilizes 128-channel custom-designed VLSI Microplex chips[74] mounted outside the active region on both ends of the detectors. The SDM's are connected to driver/receiver modules which pulse the power to the detectors in order to minimize the power dissipation, and provide the timing signals to the Microplex chip readout. The readout is controlled by nine microprocessor-controlled ADC's, the so-called "Brilliant Analog-to-Digital Converters" or BADC's.[75] These devices controlled the analog multiplexing of the Microplex signals, digitized the signals and analyzed the results. The BADC's performed a pedestal subtraction and a common-mode correction, and then stored the resulting pulse heights. A second pass through the data then allowed a cluster finding algorithm to select channels with significant pulse height information by requiring that a sum of pulse heights over three strips be larger than the sum of the

thresholds for those three strips. Three strips are used for finding clusters because given that a track from the IP will cross a strip at an angle of less than 200 mrad in the xy plane, this is the maximum number of strips which can have a signal generated by a single track. The pulse height information for the five strips around the center of the cluster are then sent to the VAX host computer to be saved in the event record.

The SSVD functioned quite well in general with relatively few failed channels. There were two cases in which an entire cell was rendered inoperable due to failed cables. One of these modules was lost for the entire run and the other for slightly more than half. Aside from this, only 1.6% of the remaining channels failed during the run due to defects in the detector or problems with the electronics.

2.2.4.3 Hit Finding and Track Fitting

Hits were defined at a contiguous series of detector strips with a corrected pulse height of at least $1.5\sigma_i$, where σ_i is the rms noise of each individual strip. Additionally, it was required that at least one strip have a pulse height of at least $5\sigma_i$ and that the cluster contain no bad strips. The point at which the particle traversed the module is then given by a weighted mean of the strips in the cluster. For closely spaced tracks, the algorithm splits the clusters into two separate clusters if there is a pulse height dip of more than $1.5\sigma_i$ within the original cluster, provided that each half have at least one strip have a pulse height of at least $5\sigma_i$. The pulse height of the strip dividing the two half clusters is split evenly between them. It is expected that this algorithm should work well for tracks separated by 2 or more strips. On average only 1% of tracks are affected by merged clusters due to the high granularity of the detector.

The process of matching the clusters found on the SSVD layers to the tracks measured in the CDC and DCVD begins by extrapolating the track through the SSVD and looking at all combinations of hits within ±1 mm of the track projection. This rather simple algorithm works because there are only three layers and the backgrounds are low, thus keeping the combinatorics reasonable. The final set of hits for each track is decided upon by a χ^2 test. Table 2–4 illustrates the agreement of the fraction of tracks with different numbers of hits between that found in the data and the Monte Carlo with the full detector simulation.*

The information from the SSVD hits assigned to a track is then combined with the track fit information from the CDC and DCVD to form an 8×8 covariance

* The Monte Carlo detector simulation is described in Chapter 3.

number of SSVD hits per track	fraction of tracks	
	data	Monte Carlo
0	8.0±0.6%	7.0%
1	14.4±0.8%	13.4%
2	54.0±1.5%	55.2%
3	23.5±1.0%	24.5%

Table 2–4 The fraction of tracks with various numbers of SSVD hits per track. The cuts on the tracks are all of the 'vertex quality cuts' described in Section 4.4 on page 128 (exclusive of the cut on the number of SSVD hits) which are designed to be selected high quality tracks.

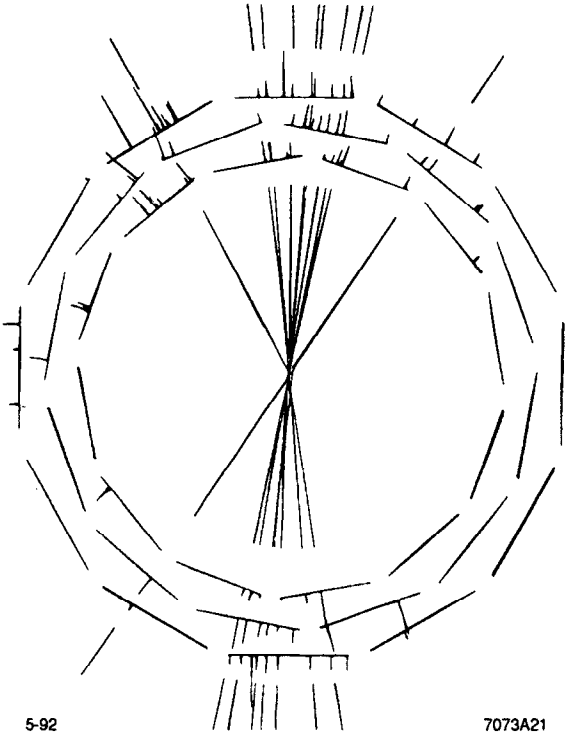

Figure 2–42 A hadronic event recorded in the SSVD. The height each hit is proportional to its pulse height. This is the same event as displayed in the DCVD in Figure 2–26.

matrix. This matrix is comprised of two parts. There is the 5×5 covariance matrix from the SARCS6 fit to the CDC and DCVD measurements and a 3×3 matrix for the SSVD hits which includes the correlations between layers due to multiple scattering.[73] Figure 2–42 shows a typical hadronic event recorded in the SSVD.

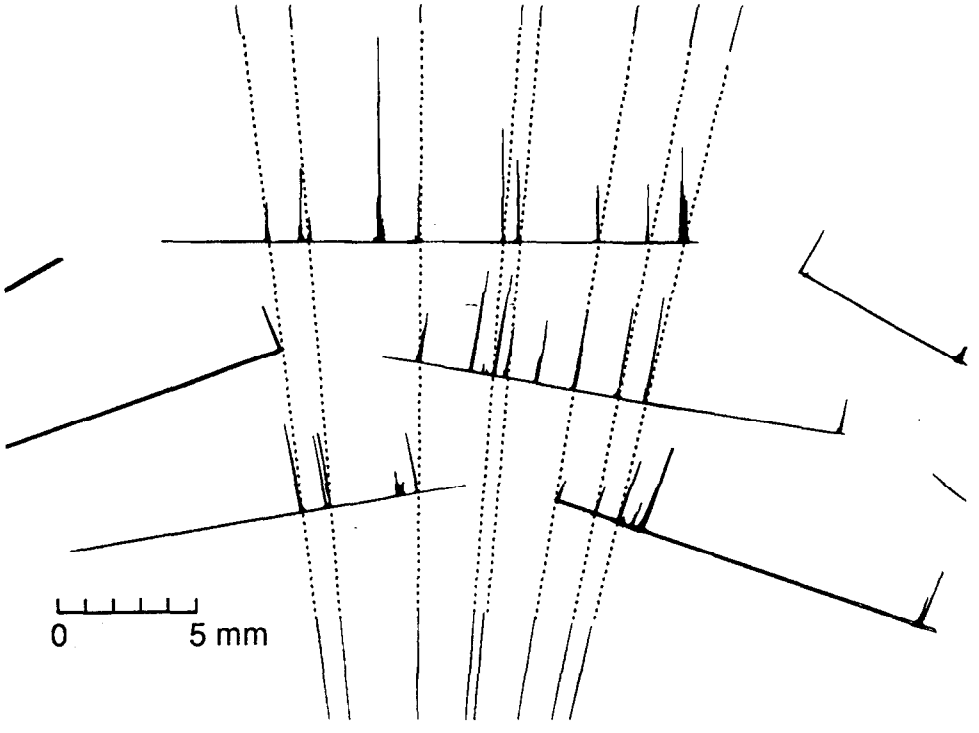

Figure 2–43 An illustration of the SSVD hit matching onto tracks from CDC and DCVD. The hits in the SSVD are shown with their pulse heights. The fitted tracks are denoted by the lines.

The ability of SSVD hits to matched with the track projections from the CDC and DCVD is illustrated in Figure 2–43.

2.2.4.4 Alignment

The local alignment of each SDM relative to the end pieces of the detector is described by seven parameters. There are three angles and two displacements along the x and y directions as illustrated in Figure 2–44. The offset in the z direction is not considered as all of the strips are axial. Additionally there are parameters to account for the possibility of a bow and twist in the module. The global alignment of each of the halves of the SSVD can be characterized by the same set of three angles and a displacement along the x and y directions.

The local alignment of the SSVD, namely the alignment of each of the detector modules relative to each other was attempted using several different approaches. Before the SSVD was installed into the DCVD, an optical alignment and an alignment using x-rays[77] to survey the detector were done. It was hoped that it would only be necessary to do a global alignment of each half of the detector with respect to the DCVD and CDC using detected tracks. Upon taking data in the

SSVD, it became clear that this was not the case. These alignments did not position the modules with respect to each other within the required accuracy. As both of the alignments are potentially quite accurate, it remains unknown why the alignments did not describe the installed detector. Possible explanations include systematic problems in these measurements or motion of the modules during installation. The precise cause notwithstanding, the situation required that tracks be used for both the global and local alignments. During the run, the motion of the SSVD with respect to the DCVD was monitored by the Capacitive Displacement Monitor (CDM).[76] This system was comprised of a series of capacitive sensors mounted on the inside of the DCVD inner core and on the outside of the SSVD. The observed motion was incorporated, but the magnitude of the effects were small compared to the sensitivity of the global alignment.

The global and local alignment procedures start with the projections of the tracks as fit by the CDC and DCVD, from which are calculated the residuals, ξ_i, in each of the SSVD layers in which a hit was assigned to this track. Note that since the SSVD hits are assigned to tracks from the CDC and DCVD based on the best hit/track matches, this procedure will be iterative. A series of variables are formed using these residuals:

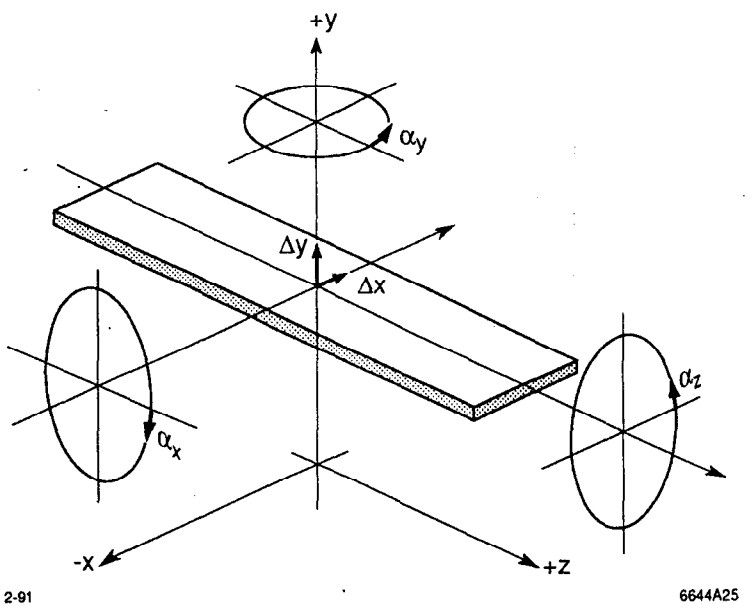

Figure 2–44 Definition of the local alignment variables Δx, Δy, α_x, α_y and α_z.

- for tracks with hits in layers j and k:

$$\Delta b_{jk} = (\xi_j + \xi_k)/2 \tag{2-6}$$

$$\Delta \phi_{jk} = (\xi_j - \xi_k)/\Delta r_{jk} \tag{2-7}$$

- for tracks with SSVD hits in three layers:

$$\Delta b_{123} = (\xi_1 + \xi_2 + \xi_3)/3 \tag{2-8}$$

$$\Delta \phi_{123} = (\xi_1 - \xi_3)/\Delta r_{13} = \Delta \phi_{13} \tag{2-9}$$

$$\Delta \delta = (\xi_1 - 2\xi_2 + \xi_3)/2 \tag{2-10}$$

The five global alignment constants per detector half are then determined by minimizing the sum of the squares of each of the variables divided by its variance using a sample of about 2100 tracks with $p_{xy} > 0.5$ GeV/c. The local alignment was similar except that it determined a subset of the seven local alignment parameters for each of the modules. This subset included the radial offsets Δx and Δy and the yaw angle α_y The sensitivity to the remaining local parameters was small and the x-ray alignment results were used for these values. The level of improvement provided by the local alignment is illustrated using the triplet residual, Δ, defined as the difference between the track fit with only the SSVD hits in the first and third layers (using curvature and z information as determined by the outer chambers) and the position of the SSVD hit in layer two. The mean triplet residual as a function of the azimuthal angle around the chamber is shown in Figure 2–45.

2.2.4.5 Position Resolution and Efficiency

The position resolution of the SSVD can be studied using the triplet residual, Δ, as defined above. A distribution of Δ for tracks with $p > 1$ GeV/c is shown in Figure 2–46. A fit to the width of this Gaussian yields a width of 8.7 μm, which corresponds to an average resolution per layer of $\sigma = 8.7/\sqrt{3/2} = 7.1$ μm. This, however, is an average over three layers with different strip pitches (25, 29 and 33 μm). The Monte Carlo with the full detector simulation reproduced the observed average resolution remarkably well. This Monte Carlo assumes intrinsic resolution of 5, 6 and 7 μm for the three layers. It also includes effects from beam-related backgrounds and the uncertainty in SSVD alignment, which effectively add 3 μm and 2.5 μm in quadrature to the resolution, respectively.

The hit finding efficiency was investigated by looking at tracks with two or more hits. A straight line between the hits was defined and if the line crossed a third

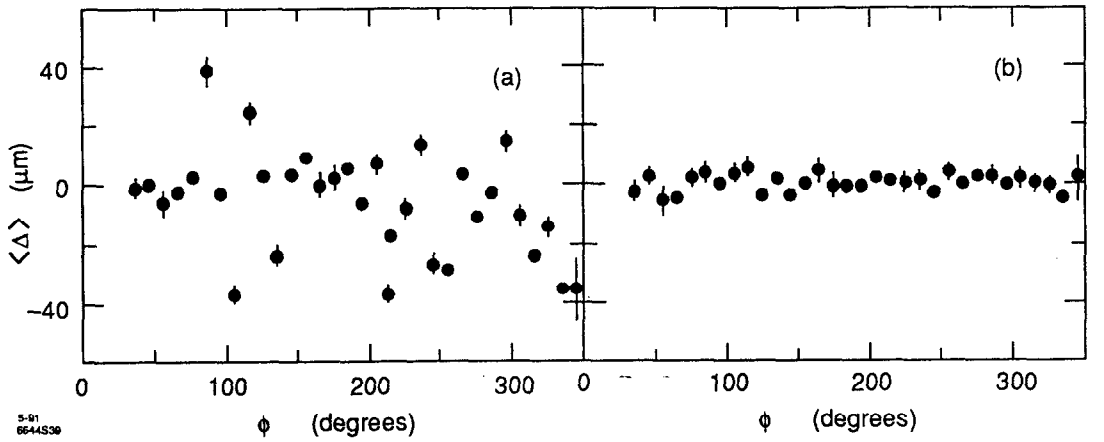

Figure 2–45 Mean triplet residual, Δ, as a function of the azimuthal angle, ϕ, (a) before and (b) after the local alignment. Each point corresponds to a different set of three overlapping modules. The lack of points between 0 and 36° is the result of the dead module in that region.

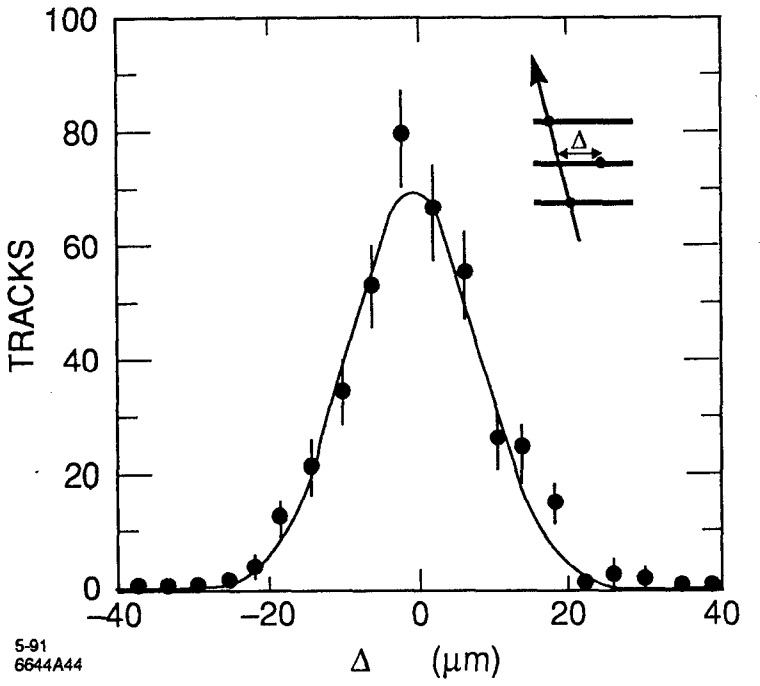

Figure 2–46 Distribution of triplet residuals observed in the data (points) and the Monte Carlo with the full detector simulation (line), for tracks with at least 1 GeV/c of momentum.

module farther than 10 strips from any know bad strips a hit was sought in that layer. To avoid problems from close tracks it was required that the track in question be at least 15 mrad from any other track. Furthermore, each hit was required to be at least 30 strips from any other hit to reduce effects from background hits. Of 731

pairs of hits satisfying the above requirements, 730 had a hit located within three strips of the predicted location, corresponding to a hit finding efficiency of 99.9±0.1%.

2.2.5 The Beam Pipe

The beam pipe used for the 1990 Mark II run has a diameter of 25 mm in order to get the inner detecting layers as close as possible to the interaction point. The central section of the beam pipe, which spans the entire angular acceptance of the tracking detectors, is made from a 0.483 mm thick aluminum tube with a 0.025 mm coating of copper to aid in the absorption of low energy photons. The beam pipe also contains two "wire flippers" for measuring beam profiles in the vertical and horizontal directions.[78] These wire flippers hold carbon fiber wires which can be inserted into and retracted from the beam axis. These wire flippers are 0.80 mm of aluminum and cover about 11% of the solid angle in the region given by $|\cos\theta| < 0.8$. The beam pipe assembly is shown in Figure 2–47.

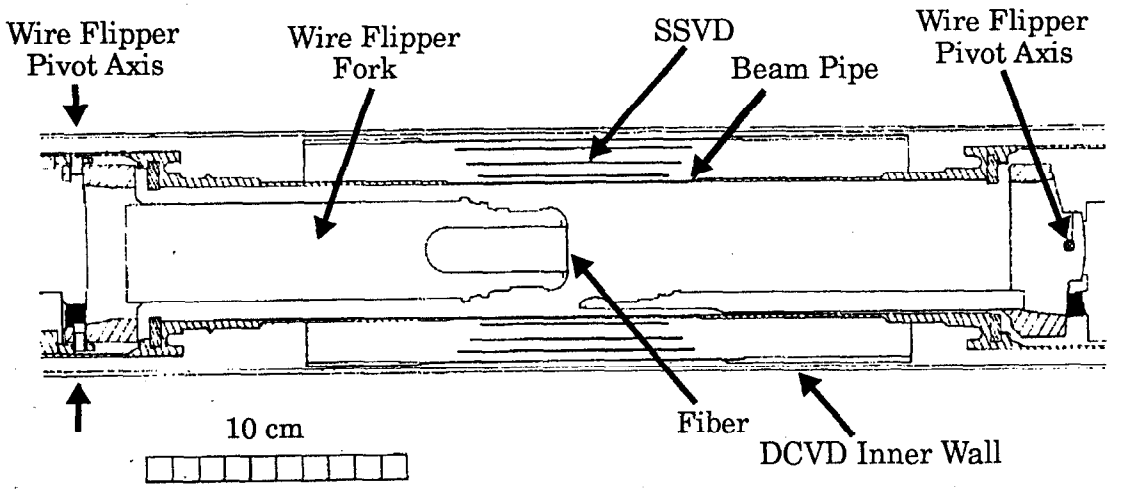

Figure 2–47 Beam pipe and wire flipper assembly.

2.2.6 Tracking Detector Summary

Table 2–5, below, has a summary of the primary dimensions and performance parameters of the tracking detectors. Table 2–6 lists the material present in the different detectors, which will be important in the performance of the tracking detectors which is the subject of later chapters.

2.2.7 Extraction Line Spectrometers

The energy of the beams at the interaction point is determined using a pair of precision spectrometers housed in the extraction lines of the SLC (refer to

Parameter	CDC	DCVD	SSVD
Number of layers	72	38	3
Active inner radius (cm)	19.2	5.3	2.94
Active outer radius (cm)	151.9	16.5	3.80
Active length (cm)	230	48	7.2–9.0
$\lvert\cos\theta\rvert$ acceptance (all layers)	0.60	0.82	0.77
Average resolution (μm)	185	61	7.1
Double track resolution (μm)	~4000	~400	~60
Double track resolution (mrad)	~5	~4	~2
Number of readout channels	5832	380	18432

Table 2–5 A summary of some of the parameters for the three tracking detectors.

Item	Radius (mm)	Thickness (% R.L.)
wire flipper	23.7	0.90
beam pipe	25.0	0.75
SSVD inner shell	27.6	0.11
SSVD layers (3)	29.4–38.0	0.55/each
SSVD outer shell	41.0	0.11
DCVD inner shell	45.0	0.86
DCVD gas & wires	50–170	0.72
DCVD outer shell	177	5.93
CDC inner shell	190	0.95
CDC gas & wires	190–1520	2.12

Table 2–6 A list of the location and number of radiation lengths of the material present in the tracking detectors. Note that the wire flipper only covers 11% of the azimuthal acceptance. The amount of material was studied using tracks, and these values reflect small corrections to the nominally measured values (within the measured errors). See Section 4.5.2, "Multiple Scattering-Limited Resolution," on page 138.

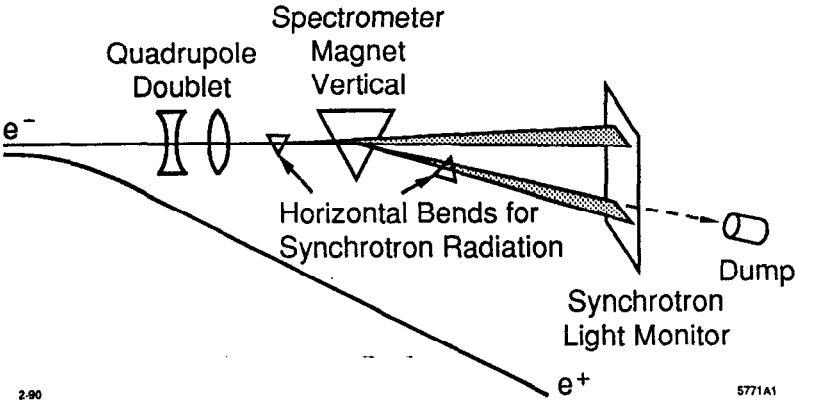

Figure 2–48 A schematic diagram of the Extraction Line Spectrometer.

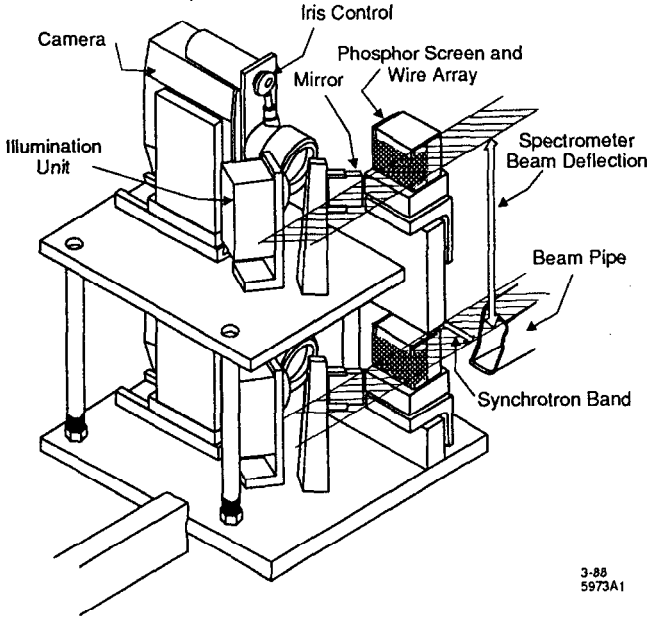

Figure 2–49 The Phosphorescent Screen Monitor for detecting the synchrotron beams from the Extraction Line Spectrometer.

Figure 2–1 on page 31). The schematic layout of the Extraction Line Spectrometers[79] is shown in Figure 2–48. The e^- or e^+ beams are directed through a vertical bend magnet whose field has been carefully mapped and are monitored throughout the run. Before and after this vertical bend are horizontal bend magnets which produce swaths of synchrotron radiation. The principle device used for detecting the synchrotron radiation was the Phosphorescent Screen Monitor (PSM) This is illustrated in Figure 2–49. The PSM has a target for each of the synchrotron beams which is an array 100 μm wires at a 500 μm spacing and a phosphorescent

screen to emit light when struck by the synchrotron beams. The wire positions and the spot on the phosphorescent screen due to the striking synchrotron beam are recorded by a camera, whose output is digitized for processing. This system has achieved an absolute $e^{\pm}$ beam energy measurement accuracy of ±35 MeV.

2.2.8 Trigger System

The trigger system selects events which are to be stored on magnetic tape for future analysis. There are three different triggers for selecting hadronic and leptonic events. These triggers use information from different detector systems and provide a level of redundancy sufficient to be fully efficient for triggering on hadronic events. There are also two special purpose triggers for selecting cosmic ray events and events at random beam crossing intervals. Information from these trigger systems is passed to the VAX host computer via the Master Interrupt Controller (MIC).

Charged Particle Trigger

This trigger uses CDC and DCVD to locate track patterns entirely in hardware using coarsely segmented hit information. The trigger for the 1990 runs used nine layers of the CDC and three layers of the DCVD. In the CDC, the basic unit used in this pattern finder was a jet cell. A cell was considered to be hit if at least four of the six wires had TDC information. In the DCVD, the information from the postamplifiers was divided into eight time bins for the trigger. These hit patterns were loaded into shift registers and transferred to hardware curvature finding modules to identify the hit patterns (see Figure 2–50). Each module searches for tracks in a given range of curvature and typically require 10 layers to define a track. Tracks within 10° of each other are considered one track. The total number of detected tracks is passed to the MIC for a trigger decision.

Calorimetry Energy Trigger

The calorimetry energy trigger searches for events of interest by matching certain pre-selected event topologies to the detected events. The information from the Liquid Argon Calorimeter and Endcap Calorimeters are used for a Total Energy Deposition (TED) trigger, which sums energy seen by both calorimeters. Signals in the SAM and mini-SAM are used to form a low-angle Bhabha trigger for luminosity monitoring. This is accomplished with the aid of the programmable Memory Logic Modules which interfaces with MIC.

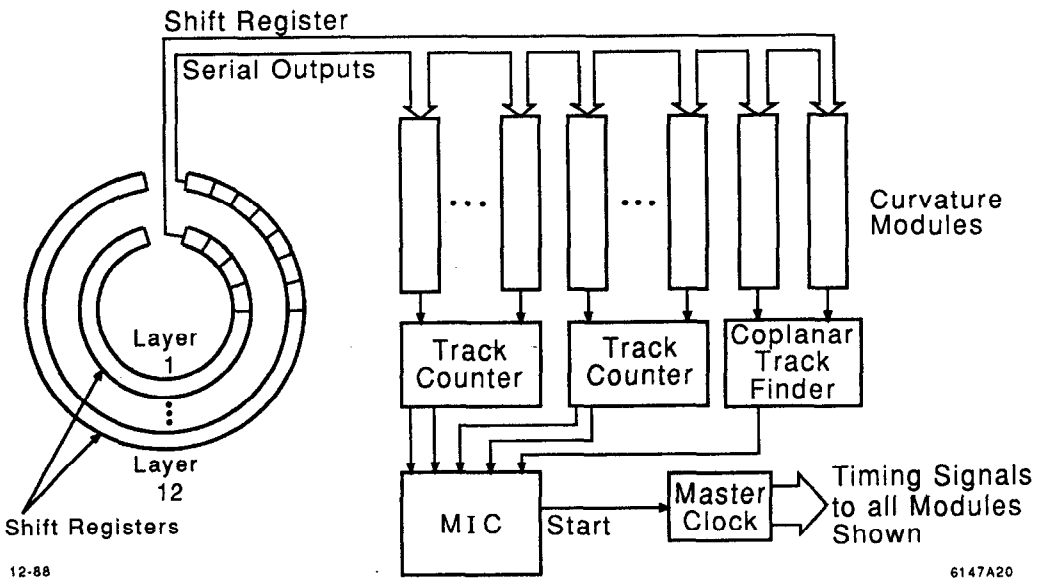

Figure 2–50 Block diagram of the charged particle trigger.

SSP-Based Software Trigger (SST)

The SST[80] was designed to improve upon the TED trigger by processing the energy information with programmable FASTBUS modules, the SLAC Scanner Processors (SSP's).[55] This provided a great deal of flexibility in optimizing the trigger algorithms compared to a hardware trigger. The calorimeter information is read into LeCroy 1885N FASTBUS ADC's and then summed into clusters by the SSP's. The trigger algorithms can then sum this information into towers which point back toward the IP and compare the results to expected patterns to make the trigger decision.

Cosmic Trigger

The cosmic trigger is used to identify cosmic ray events either between beam crossing or during dedicated cosmic ray runs. These events are useful for detector studies such as those previously discussed in the chapter. The events can be selected with either the normal charged trigger or by the Coplanar Track Finder (CTF) which is designed specifically to look for back-to-back tracks. The CTF uses two curvature modules to estimate the azimuthal angle of the track and returns a positive result to MIC if the tracks are within about ~11° of each other.

Random Trigger

Finally, there is a random trigger to select and record events on random beam crossings. This aids in monitoring the beam-related backgrounds and including their effects in the Monte Carlo detector simulation.

2.2.9 Data Acquisition System

The data acquisition system of the Mark II[51] reads the data from each of the detectors systems through CAMAC and FASTBUS systems and sends it to the VAX 8600 host computer. The on-line programs running on the VAX then merges the data records and stores them in the appropriate order onto magnetic tape. The VAX is also responsible for environmental and performance monitoring of parts of many detectors. The CAMAC system reads out a variety of instrumentation modules and the BADC's.[75] The FASTBUS system reads out through a master SSP[55] which controls the SSP's placed in each FASTBUS crate for reading out the TDC's or FADC's in that crate.

The data acquisition system is operated for each bunch crossing of the SLC. This introduces no dead-time because of the low 120 Hz repetition rate of the SLC. If a trigger detects a valid event, the data acquisition system reads out the CAMAC system and starts the read-out process of the FASTBUS system.

Chapter 3

Monte Carlo Simulation

In order to extract results about the physical processes underlying observed data, a Monte Carlo simulation is employed. Specifically, in the following analyses the Monte Carlo will be used to calculate the efficiencies for the tagging algorithm and the relations between the observed and the produced (or corrected) multiplicity. The Monte Carlo can be divided into two equally important parts: the models which generate the four-vectors of the particles from the electron-positron annihilation, and the algorithms for simulating the effects of the detectors in which we observe the tracks.

3.1 Electron-Positron Interaction Overview

The process through which hadrons are produced in electron-positron annihilation can be divided into a number of distinct processes, illustrated in Figure 3–1. The first process is initial state photon radiation, which affects the amount of energy available in the following annihilation. The probability of a hadronic event with a radiated photon of a given energy is the product of the probability to radiate a photon of that energy and the probability to produce a hadronic event at the reduced center of mass energy. At the Z^0 pole, initial state radiation is suppressed because the cross section is lower on either side of the pole. Above the Z^0 pole, however, this effect enhances the radiation such that many

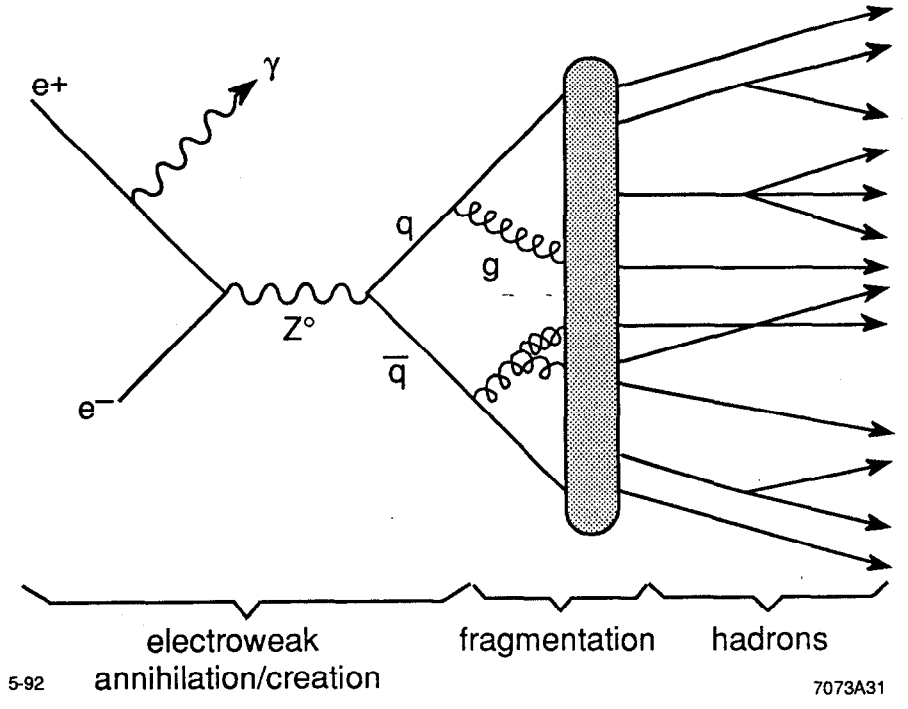

Figure 3–1 Schematic illustration of an e^+e^- annihilation event.

events will radiate the amount of energy required to reduce the center of mass energy to the Z^0 mass.

The annihilation of the electron-positron pair into the Z^0, and its decay into a quark pair is of course governed by the electroweak force. As discussed in Chapter 1, this process is calculable and has been studied in detail.

The radiation of gluons from the initial quarks and the conversion of these quarks and gluons into hadrons is dealt with in the fragmentation process. For reasons discussed in Section 3.2, this process is not calculable. Consequently one must employ physically-motivated models to handle the hadronization process.

Some of these produced hadrons decay via electromagnetic, weak or strong processes. Of particular importance in this analysis is the weak decay of the bottom and charm flavor hadrons, such as $B \rightarrow D + X$ which is discussed further in Section 3.3. Finally, the particles are observed in the detectors.

3.2 Fragmentation Models

The methods which are employed to calculate the effects of the strong force vary depending on the energy of the quarks. At high quark energies, the strong coupling constant, α_s, is much less than unity. For instance at the Z^0, the Mark II has

measured α_s to be $0.123 \pm 0.009 \pm 0.005$.[81] The consequence of this for perturbative calculations is that the effects of the increasingly complicated and numerous diagrams with more gluon vertices will tend to yield smaller corrections as the order of the diagrams in α_s increase. Thus, in principle, the calculations may be terminated at the order for which yields the accuracy desired. In practice, however, this calculation becomes extremely complex with the increasing order of α_s, and presently only those diagrams up to $O(\alpha_s^2)$ have been calculated.[82]

At lower energies, around 1 GeV, the strong coupling constant becomes larger than unity. Consequently, the perturbative approach becomes useless, as each succeeding level of diagrams can produce corrections of the same order as the $O(\alpha_s)$ diagrams. These low energies are of critical importance, however, because it is here that the quarks and gluons hadronize. It is precisely to cope with this low energy regime that the models of fragmentation were developed. A number of different fragmentation models have been developed. Reference [83] reviews the present status of these models.

3.2.1 Lund Monte Carlo

For this analysis, we use the Lund Monte Carlo (JETSET version 6.3).[84] We have elected to use the parton shower model to generate the final state quarks and gluons, and string fragmentation to combine these into hadrons.

The parton shower model[85] is a QCD cascade model in which partons are produced in a quark-gluon shower analogous to an electromagnetic shower. A leading log approximation is employed to determine the 'branching' during the shower process. The final state at the end of the shower is mostly comprised of gluons. This model was introduced into the Lund Monte Carlo to better reproduce the behavior expected at energies higher than those of PEP and PETRA. At those energies, the 2-, 3- and 4-parton states produced by matrix element methods were generally regarded as sufficient, though some evidence pointed to the limitations of that approach.[86] The parton shower method generates showers by the three possible branchings: $q \to qg$, $g \to gg$ and $g \to q\bar{q}$ (see Figure 3–2). The probability for each of these branchings is given by

$$dP_{a \to bc} = \frac{\alpha_s(Q^2)}{2\pi} \frac{dm_a^2}{m_a^2} P_{a \to bc}(z)\, dz \qquad (3\text{-}1)$$

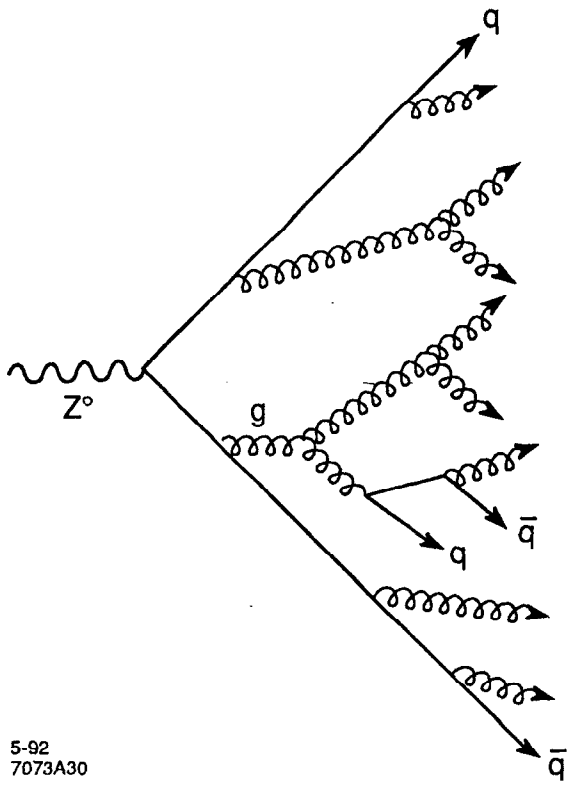

Figure 3–2 Parton shower evolution process.

where m_a is the mass of the parton a, z is the energy fraction E_b/E_a in the center of mass frame of the event, $Q^2 = z(1-z)m_a^2$ and α_s is calculated from the first-order expression:

$$\alpha_s(Q^2) = \frac{12\pi}{(33-2n_f)\ln(Q^2/\Lambda^2)}, \tag{3-2}$$

where n_f is the number of quark flavors and Λ is the QCD scale parameter.

The functions $P_{a\to bc}(z)$ are given by the Altarelli-Parisi splitting functions:[87]

$$\begin{aligned} P_{q\to qg}(z) &= \frac{4(1+z^2)}{3(1-z)} \\ P_{g\to gg}(z) &= \frac{6(1-z(1-z))}{z(1-z)} \\ P_{g\to q\bar{q}}(z) &= \frac{(z^2+(1-z)^2)}{2} \end{aligned} \tag{3-3}$$

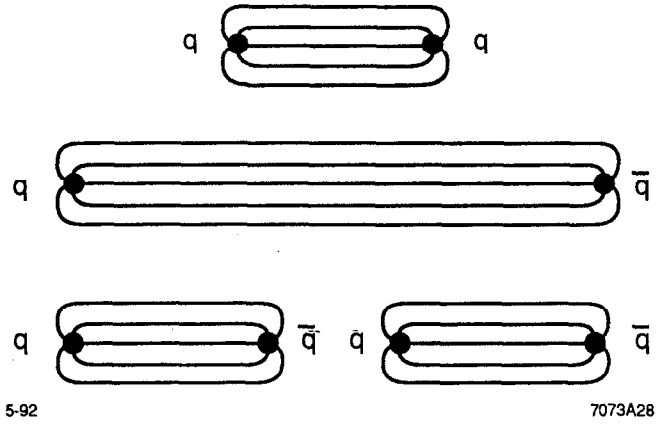

Figure 3–3 The color flux lines stretched between a pair of quarks until there is enough energy to produce a new quark pair from the energy of the color field.

In the leading log approximation, there is a coherence effect between Feynman diagrams which is equivalent to an angular ordering, meaning that the opening angle for a parton branching cannot occur an angle larger than that of the previous branching. The angular ordering is imposed as an additional constraint on the value of z and the masses.

The initial partons are produced substantially off-shell and the parton shower is continued until the virtuality of all of the partons reach a cut-off value which is fixed at m_{min} for gluons and $m_q + \frac{1}{2}m_{min}$ for quarks (where m_q is the constituent quark mass). Typical values of m_{min} are ~1 GeV.

Once the parton shower is finished, the partons are formed into hadrons using the Lund string fragmentation model.[88] String models are based on the idea that because of the coupling between gluons, the strong force flux lines between partons will tend to be close together, forming a narrow flux tube, or string. If this string is assumed to be uniform along its length, this leads to a potential which depends linearly on the length of the string. The energy density of the string, κ, is about 1 GeV/fm (0.2 GeV ^{2}). As the partons stretch the string, the energy stored in the string increases until it is sufficient to create a new quark-antiquark pair (see Figure 3–3). It is possible with the Lund model to have strings with additional gluons from the parton shower on the string connecting the quark and antiquark. Due to the momentum of these gluons, they will appear as kinks in the string connecting the quarks.

Baryons are formed either by production of diquarks[89] or by the popcorn mechanism.[90] In the former method, diquarks are allowed to be produced from a single breaking of the string. These diquarks can then combine with the quarks on the ends of the string to form baryons. The latter method involves the production of two or more $q\bar{q}$ pairs, of a different color than the $q\bar{q}$ on the end of the string, from which different combinations of baryons (B) and mesons (M), such as $B\bar{B}$, $BM\bar{B}$, $BMM\bar{B}$, *etc.*, can be formed. In practice, the probability for all but the first two combinations is very small in the Lund model. These baryon production models require numerous parameters, which characterize diquark production, strange diquarks, spin-1 diquarks, the relative probability of $B\bar{B}$ to $BM\bar{B}$, and strange quark suppression factors for the quarks which make of the meson, M, and the quark shared between the B and $\bar{B}$.

A string usually breaks when the quark and antiquark at each end of the string are about 1–5 fm apart. The quarks must be produced at a separation large enough such that the energy required to generate the quark's mass and transverse momentum is removed from the field. The quantum mechanical tunneling probability for the quarks to be produced with a particular transverse mass m_T is proportional to

$$\exp\left(-\pi m_T^2/\kappa\right) = \exp\left(-\pi m^2/\kappa\right)\ \exp\left(-\pi p_T^2/\kappa\right). \tag{3-4}$$

Locally the transverse momentum, p_T, is balanced between the $q\bar{q}$ pair. This equation also implies the suppression of heavy flavor production: strange quark production is reduced by a factor of about 0.3 while charm reduced by about 10^{-11} relative to the up and down quarks. Consequently, charm and bottom quarks do not participate in the soft fragmentation. In the Lund Monte Carlo, the generated parton p_T distribution is described by a Gaussian whose width, σ_0 is a tunable parameter. Similarly, the suppression of $s\bar{s}$ production relative to $u\bar{u}$ and $d\bar{d}$, and the production of pseudo-scalar to vector particles are also input parameters.

The longitudinal fragmentation is expressed in terms of the fraction of energy which the quark passes on to a meson. The Lorentz invariant variable used is chosen to be

$$z = \frac{(E+p_L)_{hadron}}{(E+p)_{quark}}, \tag{3-5}$$

where p_L is the momentum along the original quark direction. The probability of a quark pair to form a meson of transverse mass m_T with a particular value of z, is given by the Lund symmetric function,[91]

$$f(z) \propto \frac{1}{z} z^{a_1} \left[\frac{1-z}{z}\right]^{a_2} \exp\left[\frac{-bm_T^2}{z}\right], \tag{3-6}$$

where the a_i are quantities which may depend on the flavor of the quarks which together define the hadron and b as flavor independent. This form was developed in order to ensure a left-right symmetry so that the fragmentation process will yield the same results regardless of the end of the string chosen as the starting point. In practice, it is normally assumed that the a_i are the same

$$f(z) \propto \frac{(1-z)^a}{z} \exp\left[\frac{-bm_T^2}{z}\right]. \tag{3-7}$$

Thus, $f(z)$ depends only on two parameters (a and b). Note that this function $f(z)$ is not the probability of a primary hadron being produced in a particular event with a given z, but rather it is the probability used each time a string is broken producing a new quark pair. The former quantity, $D(z)$, is a combination of the $f(z)$ functions folded together according to the ordering along the string.

3.2.2 Heavy Quark Fragmentation

The large mass of the charm and bottom quarks compared with the light quarks requires that effects of flavor-dependent fragmentation be included in these events. Compared to light quarks, the fragmentation of heavy quarks is expected to be much harder, meaning that the distribution of energy carried away by the hadron containing the heavy quark favors larger values of z.[92] This hard fragmentation has been observed for both charm and bottom events at PEP and PETRA[42][93] and at LEP.[22][23][24][94][95] The most common parameterization for the probability of heavy hadrons being produced with a particular value of z is given by the Peterson function.[94] A phenomenological picture of the heavy quark fragmentation process of $Q \rightarrow H + q$, where $H = Q\bar{q}$ is illustrated in Figure 3–4. The Peterson function was derived on the assumption that the amplitude for this process is proportional the reciprocal of the energy transfer $\Delta E = E_H + E_q - E_Q$. If this is expanded in

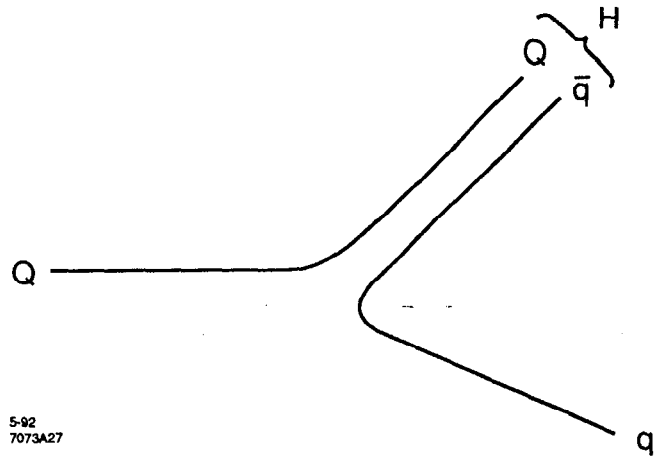

Figure 3–4 A phenomenological diagram of the fragmentation of a heavy quark, Q, into a hadron, H, and an antiquark.

terms of the particle masses, and a $1/z$ term is included to account for the effect of longitudinal phase space, then the result is:

$$D_Q(z) \propto \frac{1}{z\,[1-1/z-\varepsilon_Q/(1-z)]^2}, \tag{3-8}$$

where the parameter ε_Q is given by the ratio of the light to heavy quark transverse masses:

$$\varepsilon_Q = \frac{m_T^2(\text{light quark})}{m_T^2(\text{heavy quark})} \tag{3-9}$$

A plot of this function is shown in Figure 3–5. Because heavy quark production in soft fragmentation is almost entirely absent, the fragmentation probability function $f(z)$ is just the same as $D_Q(z)$, unlike for *uds* events.

A caveat which should be noted in the use of the fragmentation functions for heavy quarks is that there are two slightly different definitions of z (and ε) which can be used.[42] The definition by the Monte Carlo during the fragmentation is the primordial value of z:

$$z_{pri} = \frac{(E+p_L)_{hadron}}{(E+p)_{unfragmented\ system}}, \tag{3-10}$$

where the unfragmented system includes the heavy quark as well as other nearby quarks. The other definition is known as the reconstructed value, z_{rec}, and is

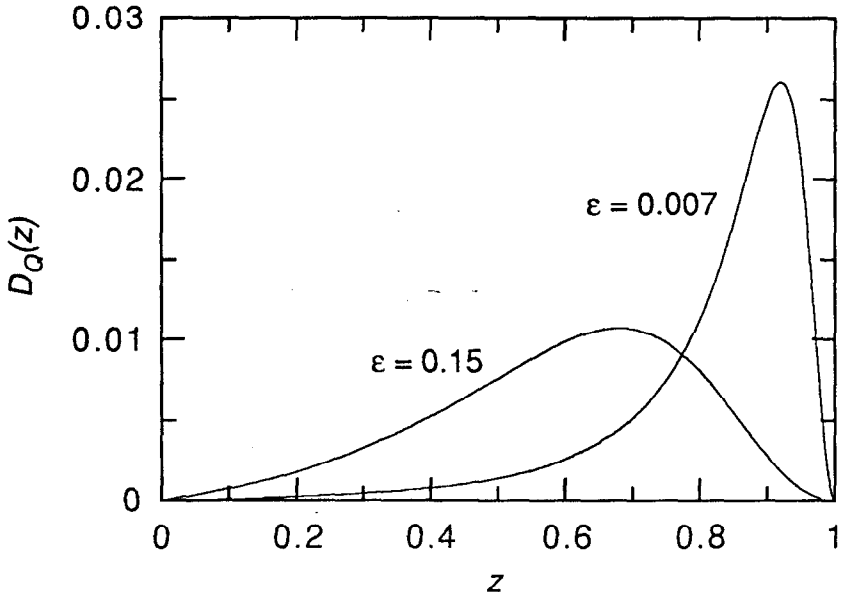

Figure 3–5 The Peterson fragmentation function for ε of 0.15 and 0.007, which yield an average z of 0.59 and 0.82 respectively.

defined by Equation (3-5). This value is favored for comparison among different experiments as it is model independent. Finally, it should be noted that the while the Peterson function is adequate for use as the input to the Monte Carlo, one should use caution when fitting (corrected) z_{rec} distributions for a number of reasons, including the possibility of events with a hard gluon having $z_{rec} > 1$, a feature which is not accommodated by the Peterson function.[6][42]

Guided with the results found by Chrin,[42] the values of ε_c and ε_b used by the Peterson function for describing the longitudinal fragmentation of charm and bottom quarks to hadrons are 0.15 and 0.007, when the parton shower model is employed. These correspond to averages of the Peterson function of 0.67 and 0.83, respectively. With these values as input to the Monte Carlo, the average values for the quantity $x_E = 2E_{had}/E_{cm}$ are $\langle x_E \rangle_c = 0.41$ and $\langle x_E \rangle_b = 0.68$.

3.2.3 Monte Carlo Tuning

The Lund Monte Carlo fragmentation parameters which are used in this analysis are the result of tuning the Monte Carlo with Mark II data at PEP (E_{cm} = 29 GeV), which if the Monte Carlo properly treat the energy dependency, are expected to be valid at the Z^0.[97] As illustrated in the following section, the Monte Carlo with this tuning is in fact a reasonable description of the data. More

recent high-statistics studies at LEP have shown no major sources of disagreement between various versions of the Lund Monte Carlo and their larger data sample.[102]

Table 3–1 gives a partial list of the parameters used in the Monte Carlo. Parameters not included in this table, such as the various baryon production parameters,* should be assumed to be the default parameters in JETSET version 6.3.[84]

3.2.4 Hadronic Event Properties

Using the 528 event sample recorded by the Mark II in 1989, the global properties were studied and it was found that a Monte Carlo with this tuning is a good model for describing the data.[62][98] The events in these plots were selected with a standard set of cuts for selecting hadronic events which is described in Section 4.3. A small number of cuts were made on the tracks used, chief among them that the track have $|\cos\theta|$ of less than 0.82 and that the projection of momentum in the plane perpendicular to the beam axis be at least 300 MeV/c. Two useful event shape parameters are the thrust and sphericity. The thrust, T, is defined as

$$T = \max\left(\frac{\sum_i \vec{p}_i \cdot \hat{T}}{\sum_j |\vec{p}_j|}\right), \tag{3-11}$$

where $\hat{T}$ is the unit vector which maximizes the sum of its dot product with each of the track momenta. The sphericity, S, is a similar quantity, except that it is quadratic in momentum. It is defined as

$$S = \frac{3}{2}\min\left(\frac{\sum_i |\vec{p}_i \times \hat{S}|^2}{\sum_j |\vec{p}_j|^2}\right), \tag{3-12}$$

where the unit vector $\hat{S}$ minimizes the momentum sum. Figure 3–6 shows the agreement of the thrust and sphericity distributions between the data and Monte Carlo for the 1989 Mark II data sample. In addition to the Monte Carlo model used in this analysis (Lund 6.3) these show, for comparison, the results of other Monte Carlo models: the Weber 4.1,[99] the Caltech-II 86[100] and Lund's JETSET 6.3 using a matrix element parton generation.[84]

* The baryon production parameters are in PAR(1) through PAR(7) in COMMON LUDATE.

	Name	Description	Variable name	Value
Lund Parton Shower	Λ_{LLA}	QCD scale	PARE(21)	0.4 GeV
	m_{min}	virtuality cut-off for further parton evolution	PARE(22)	1.0 GeV
Lund String Fragmentation	$\sigma_o(p_T)$	width of parton p_T distribution	PAR(12)	0.23 GeV/c
	P(*s*)/P(*u*)	$s\bar{s}$ suppression relative to $u\bar{u}$ and $d\bar{d}$	PAR(2)	0.30
	$\left.\frac{V}{PS+V}\right\|_{u,d}$	fraction of vector *u* and *d*-flavor meson production	PAR(8)	0.50
	$\left.\frac{V}{PS+V}\right\|_{s}$	fraction of vector *u* and *d*-flavor meson production	PAR(9)	0.60
	$\left.\frac{V}{PS+V}\right\|_{c,b}$	fraction of vector *u* and *d*-flavor meson production	PAR(10)	0.75
Lund Symmetric Fragmentation Function (*uds*)	*a*	*uds* fragmentation parameter	PAR(31)	0.45
	b	*uds* fragmentation parameter	PAR(32)	0.90
Peterson Fragmentation Function (*c* and *b*)	ε_c	*c* fragmentation parameter	PAR(44)	0.15
	ε_b	*b* fragmentation parameter	PAR(45)	0.007

Table 3–1 Some of Lund Monte Carlo (JETSET version 6.3) parameters used in this analysis. The variable name refers to the location of this variable in the Lund programs LUDATE and LUDAT1 common blocks[84].

The more detailed jet structure of the events can be investigated with jet finding algorithms such as the JADE clustering algorithm (YCLUS).[101] This algorithm starts with each of the tracks being considered to be a jet and then combines them, beginning with the pairs that will yield the smallest value of the parameter $y \equiv m_{ij}/E_{vis}$, the ratio of the invariant mass to the total visible energy. This process continues until all pairs have y larger than some value y_{cut}. For a range of y_{cut}

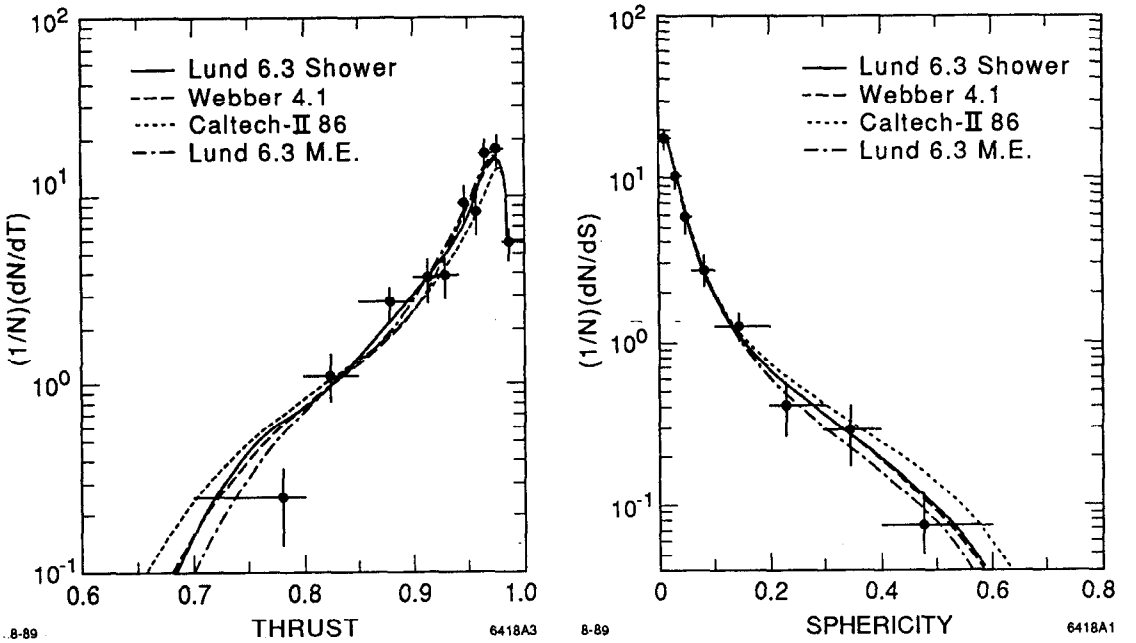

Figure 3–6 Corrected distributions of the thrust and sphericity for the events in the 1989 data sample.

values, the fraction of events with a given number of jets can be calculated and compared between data and Monte Carlo, as is shown in Figure 3–7(a). Another method of using this algorithm is too look at the value of y at which the event forms only two jets. The resulting differential distribution, $D_2(y)$, is illustrated in Figure 3–7(b).

Inclusive track distributions can also be investigated. The detected charged multiplicity distribution is shown in Figure 3–8. The distribution of the fraction of tracks with $x = 2p/E_{cm}$ is shown in Figure 3–9. The momentum projected into the plane perpendicular to the sphericity axis is another way to view the jet nature of the events. This momentum is shown in Figure 3–10 as the component in the plane of the event ($p_{\perp in}$) and that out of the plane of the event ($p_{\perp out}$).

These various plots, illustrating the global event properties, the jet production properties and the inclusive track properties, all confirm that within the statistics of this measurement, the Lund Monte Carlo tuned at PEP energies shows excellent agreement with that observed data at 91 GeV.

3.3 Heavy Hadrons in the Monte Carlo

As noted in Table 3–1, charm and bottom mesons are produced from Z^0 in the ratio of 3:1 vector (D^* and B^*) to pseudoscalar (D and B). With a B^*–B mass

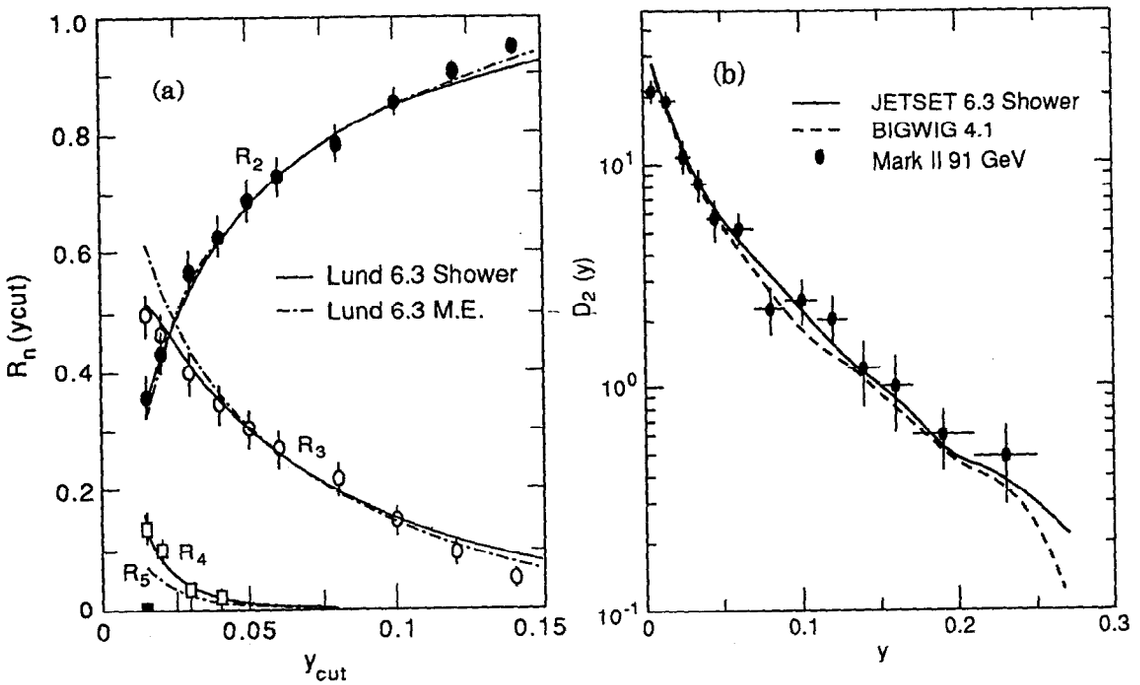

Figure 3–7 Jet distributions: (a) integral distribution of the number of events as a function of y_{cut}, and (b) the differential distribution of the y value for which an event goes from 3 to 2 jets.

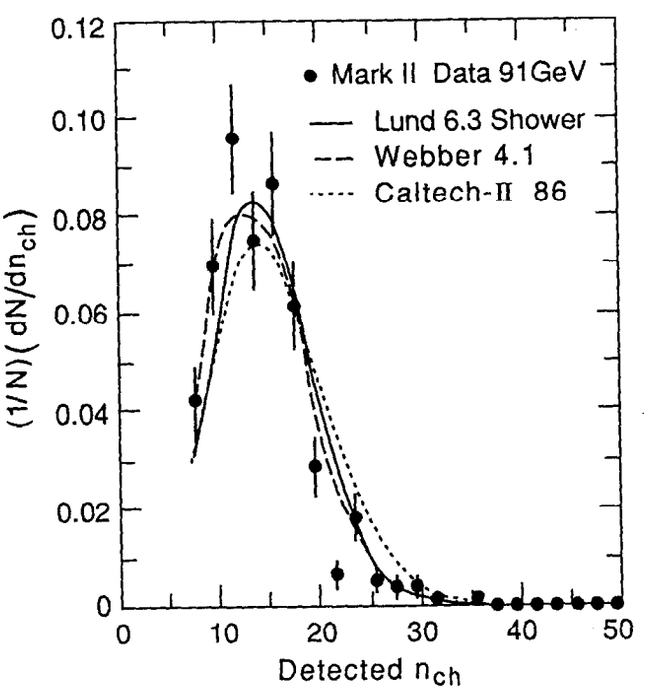

Figure 3–8 Distribution of the number of detected tracks per event passing the fiducial cuts observed in the data and as predicted by several Monte Carlo models.

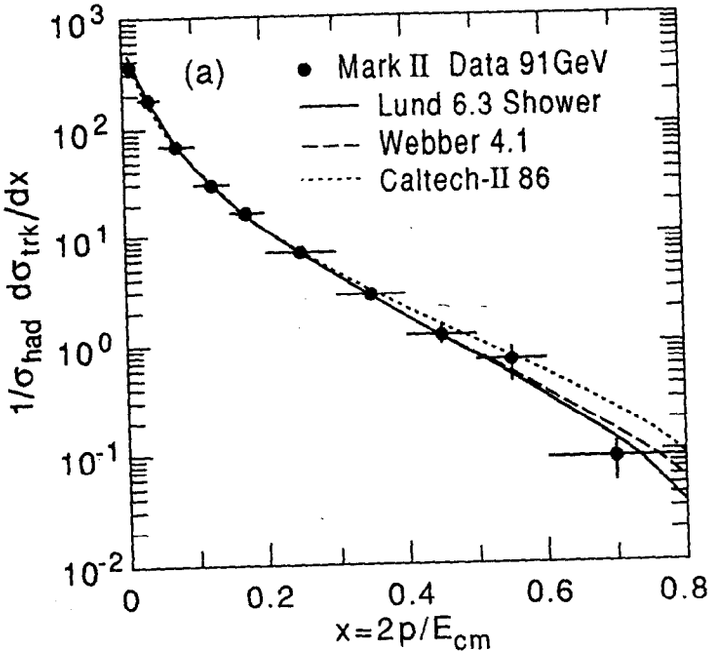

Figure 3–9 Distribution of the scaled momentum.

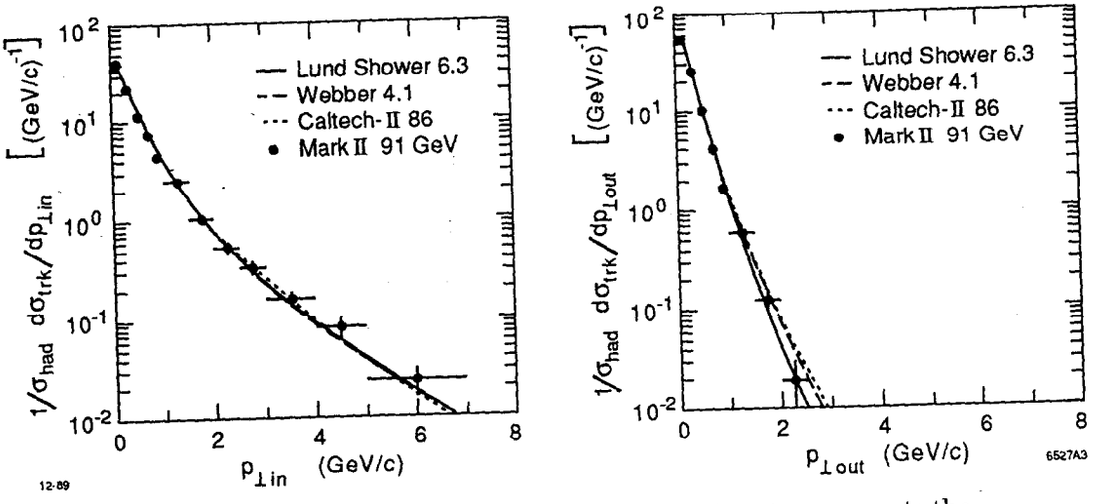

Figure 3–10 The two projections of the momentum transverse to the sphericity axis: the projection in and out of the event plane.

difference of ~50 MeV, the B^* mesons all decay electromagnetically to a B meson.[8] The D^* mesons decays both hadronically and electromagnetically, however the possible hadronic decay modes are different for neutral and charged D's:[8]

$D^{*0} \to D^0 \gamma$	45±6%	$D^{*+} \to D^+ \gamma$	18±4%
$D^{*0} \to D^0 \pi^0$	55±6%	$D^{*+} \to D^+ \pi^0$	27.2±2.5%
$D^{*0} \to D^+ \pi^-$	not allowed	$D^{*+} \to D^0 \pi^+$	55±4%

Note that the D^{*0} is not allowed, by conservation of energy, to decay into the charged pion. This results in an asymmetry of the produced charged and neutral D mesons, despite the fact that the mesons are produced in equal numbers of charged and neutral varieties. All other excited hadrons such as the heavy strange mesons, D_s^* and B_s^*, and spin $\frac{3}{2}$ baryons are decayed to the ground state mesons electromagnetically by the Monte Carlo. The ground state heavy strange mesons comprise 13% (12%) of all heavy flavor baryons for charm and bottom mesons, respectively. The heavy flavor baryons comprise 9% of the heavy hadrons for both charm and bottom.

The Monte Carlo then decays the ground state heavy flavor hadrons weakly by the emission of a virtual $W^{\pm}$ boson. The simplest diagram for the decay of heavy hadrons is the spectator diagram shown in Figure 3–11. The lifetimes for the various charm hadrons has been well measured for each type:[8]

$\tau(D^0) = 0.421 \pm 0.010$ psec	$\tau(D^+) = 1.062 \pm 0.028$ psec
$\tau(D_s) = 0.445^{+0.035}_{-0.029}$ psec	$\tau(\Lambda_c) = 0.191^{+0.017}_{-0.013}$ psec

These lifetimes vary quite significantly, a fact which is not predicted by the spectator model. These lifetime differences are believed to arise from interferences between diagrams and diagrams with interactions involving the spectator quark such as annihilation and W-exchange. The Monte Carlo generation used values equivalent to these, with the exception of the Λ_c whose lifetime was 0.10 psec.

The situation is different in the case of average bottom hadrons. The lifetime of the admixture of bottom hadrons produced at PEP, PETRA and LEP has been reasonably well measured,[8][25] but considerably less constraint exists for the separate species of bottom hadrons.* Hence, the Monte Carlo decays all of the bottom hadrons with the same lifetime given by the average bottom hadron

* The present status of the separate B lifetime measurements is discussed in more detail in Section 6.3.1 on page 180.

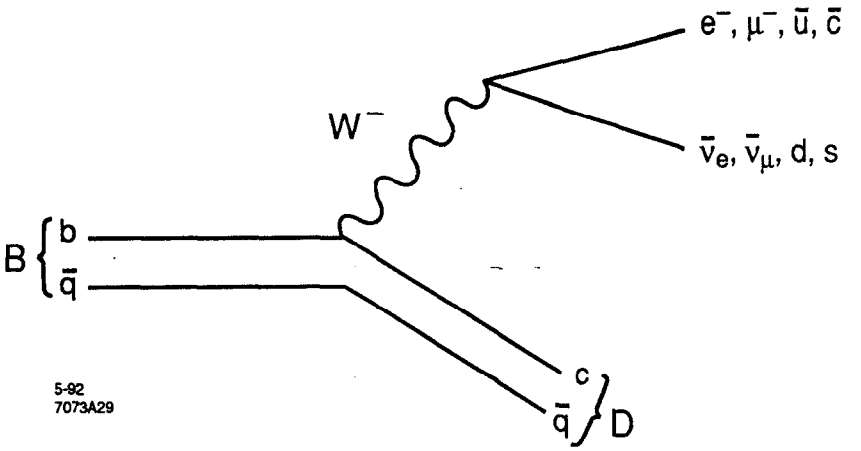

Figure 3–11 The spectator diagram for the decay of a hadron containing a heavy quark (in this example *b*) into a W^- which in turn decays into a charged-lepton and neutrino or a quark-antiquark pair.

lifetime. This is not expected to be a cause for concern as the lifetime difference among the bottom hadrons is expected to be significantly less than that observed for charm hadrons. We use a value of 1.24 psec in the Monte Carlo generation.

The weak decays of the charm and bottom hadrons in the Monte Carlo are handled somewhat differently. The decays of the D^0 and $D^{\pm}$ are handled primarily through explicit decays which have been measured or are good educated guesses of the correct branching fractions. The other charm and bottom baryons are decayed to quarks via a V – A matrix element, and then the resulting quarks are allowed to fragment like a jet system. For semileptonic decays it is assumed that the spectator system always collapses into a single hadron.

3.4 Detector Simulation

In order to relate the physical parameters of interest to the observed data, a detector simulation is employed. This allows one to study the effects of these parameters on events which are similar in nature to those we observe with the actual detectors. This detector simulation follows the generated tracks through the detectors and leaves hits at the appropriate locations. The tracking detectors are divided into layers for the detector simulation, corresponding to the material and measurement locations in each apparatus. As a particle enters each layer, probabilities are calculated for it to interact with the material in that layer and to generate a detected hit there. The effects included in this manner are multiple Coulomb scattering, nuclear scattering, energy loss, photon conversions and the

efficiency for a hit to be generated. In each of the detectors, the simulation allows all of the same reconstruction code to be used on the Monte Carlo events as is used the real data events. In the DCVD, for instance, the FADC data is simulated by placing hits from a large library of detected hits at a position determined using an inverse of the measured time-distance relationship. Nearby hits will have their pulse height information summed together. The SSVD uses a Landau distribution to determine pulse heights in each strip, accounting for the track angle. Effects such as diffusion between strips, Gaussian noise and strip-to-strip coupling are also included.

Additionally, the beam-related backgrounds observed in the data were added to the detector simulation. To do this, a set of events which were recorded by a random trigger were selected by requiring that they be near in time to a recorded Z^0 event. The raw hits in these random events were then 'mixed' onto the hits generated for tracks by the Monte Carlo. In the CDC, all of the recorded hits in Monte Carlo and background data events were combined. Closely spaced hits in a CDC jet cell were treated using the measured double-hit efficiencies to decide whether the latter hit is found. The latter hit time resolution is also degraded depending on its proximity to the prior hit. For the DCVD and SSVD, the inclusion of backgrounds was performed by adding the pulse heights of the generated Monte Carlo event and random event. In the DCVD this pulse height addition was done on a bin-by-bin basis through all of the FADC record. Similarly, for the SSVD, the pulse heights from each strip in the background event were added to the appropriate strip in the Monte Carlo event.

In the SSVD, the effects of uncertainty in the local and global alignment are also included in the detector simulation. This uncertainty is a result of alignment process which used the limited sample of hadronic tracks.* Incorporating these uncertainties into the Monte Carlo was accomplished by running the same alignment routines on Monte Carlo event samples of the same number of events as our data sample. The resulting imperfect alignment constants were then used in the track reconstruction code for the Monte Carlo events.

A significant improvement to the detector simulation was made by the implementation of a better model for multiple Coulomb scattering in the detector simulation. The original method would change the particle's direction as it passed through each scattering layer according to a Gaussian distribution whose width was

* See Section 2.2.4.4 on page 77 for information on the SSVD alignment.

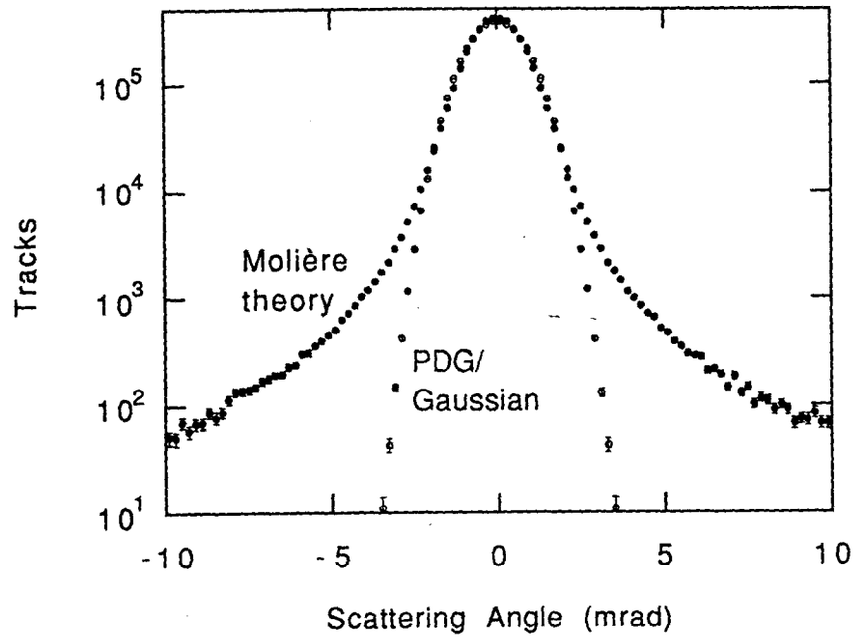

Figure 3–12 The multiple scattering angle distribution for the Molière theory as calculated by the subroutine MLR, and a Gaussian assumption using the Particle Data Group's Equation (3-13) as the width of the distribution. This particular example is calculated for a pion of momentum 1 GeV/c which is normally incident on 500 μm of silicon (which corresponds to 0.53% of a radiation length).

specified, in limit of small angle scattering, by the standard multiple scattering formula as given by the Particle Data Group:[103]

$$\Phi_{ms} = \frac{13.6\text{MeV}}{\beta cp}\sqrt{\frac{x}{X_0}}\left[1 + 0.038\log\frac{x}{X_0}\right], \qquad (3\text{-}13)$$

where x is the material thickness and X_0 is the radiation length of the material.*

There are two problems with this approach. First, the scattering layers in the Monte Carlo detector simulation can be comprised of very little material, such that it can be below the range of the validity of the standard formula ($10^{-3} < x/X_0 < 100$ for all Z). Second, this method does not properly introduce the tails from occasional large-angle scatters (plural and single scattering) which are actually present in the multiple scattering process. To do this, the Molière scattering theory[104] was employed using the MLR subroutine in the CERN Program Library (CERNLIB).[105] Figure 3–12 compares the predicted multiple scattering angle

* See Section 4.1.3 on page 116 for more information on multiple Coulomb scattering and the use of this equation.

distribution for a track passing through a particular scattering layer using a Gaussian formula and using the Molière scattering theory. The effects of this change on the track measurement will be discussed further in Section 4.5.2, "Multiple Scattering-Limited Resolution," on page 138.